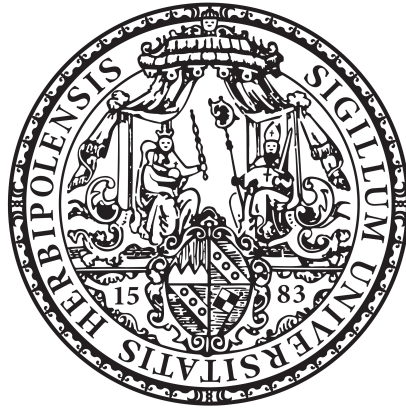


Multiwavelength Studies Of γ -Ray Emitting Radio Galaxies



Dissertation zur Erlangung des naturwissenschaftlichen
Doktorgrades der Julius-Maximilians-Universität Würzburg

vorgelegt von

Sheetal Saxena

aus Brampton

Würzburg, 2017



Eingereicht am: 02.06.2017
bei der Fakultät für Physik und Astronomie

1. Gutachter: Prof. Dr. Karl Mannheim
2. Gutachter: Prof. Dr. Peter Jakob
3. Gutachter:
der Dissertation

Vorsitzende(r):

1. Prüfer: Prof. Dr. Karl Mannheim
2. Prüfer: Prof. Dr. Peter Jakob
3. Prüfer: Prof. Dr. Raimund Ströhmer
im Promotionskolloquium

Tag des Promotionskolloquiums: 28.11.2019

Doktorurkunde ausgehändigt am:

Zusammenfassung

Der Ursprung, sowie die exakte Zusammensetzung des isotropischen Gammastrahlen-Hintergrunds (IGRB), sind trotz jahrelanger Studien über den Einfluss unaufgelöster extragalaktischer Objekte, nicht abschließend geklärt. Es wird für möglich gehalten, dass diffuse Prozesse, wie z.B. die Annihilation dunkler Materie, sowie bisher nicht detektierte Gammastrahlen-Emission aus aktiven Galaxiekernen (AGN), wie zum Beispiel Radiogalaxien, dazu beitragen. Radiogalaxien gehören zu der Gattung der Quellen, die stark im Radiowellenbereich emittieren. Einige dieser Galaxien wurden auch im Wellenlängenbereich von Gammastrahlung mittels des Fermi Large Area Telescope (Fermi-LAT) und für sehr energiereiche Gammastrahlung mittels Cherenkov-Detektoren nachgewiesen. Es wird davon ausgegangen, dass die kleinere Anzahl an nachgewiesenen Radiogalaxien im Gammastrahlenbereich, verglichen mit der Anzahl an nachgewiesenen Blazaren, auf die Orientierung ihrer Jets zurückzuführen ist. Des Weiteren wurde bisher nur eine kleine Anzahl an Radiogalaxien im Energiebereich der Gammastrahlung nachgewiesen, obwohl davon auszugehen ist, dass der Nachweis auch für weitere Galaxien möglich ist. Aus diesen Gründen werden Gammastrahlung emittierende Radiogalaxien, eine interessante und schwer auffindbare Klasse an Objekten, zur Untersuchung im Rahmen dieser Arbeit ausgewählt.

Zur Verbesserung des Verständnisses diffuser Prozesse ist eine Modellierung der spektralen Energiedichteverteilung (SED) notwendig. Da die Emission von AGN zeitlich variiert, ist es wichtig simultan aufgezeichnete Daten für die Analyse zu verwenden. Die Berechnung der spektralen Energiedichteverteilung, basierend auf zeitgleich aufgezeichneten Daten für eine Vielzahl an Wellenlängen des elektromagnetischen Spektrums, liefert eine hinreichend genaue Beschreibung des Zustandes eines Objektes innerhalb eines gegebenen Zeitraumes. Diese Arbeit konzentriert sich auf die Gammastrahlung emittierenden Radiogalaxien M 87, NGC 1275, Pictor A und Centaurus A, da diese mittels Cherenkov-Teleskopen im Bereich hochenergetischer Gammastrahlung, sowie auch in anderen Wellenlängenbereichen, nachgewiesen wurden. Es wird eine, in dieser Form erstmals angewandte, konsistente Untersuchung durchgeführt, bei der jede Radiogalaxie auf identische Weise, mittels zeitgleich aufgezeichneter Daten, analysiert wird. Dieser Ansatz unterscheidet diese Arbeit von vergleichbaren Studien.

Die Fermi-LAT Rohdaten für jede Quelle werden für die Zeiträume analysiert,

in denen diese direkt mit der Beobachtung hochenergetischer Gammastrahlung durch Cherenkov-Teleskope, sowie darüber hinaus mit weiteren Wellenlängenbereichen, überlappen. Das Synchrotron Self-Compton (SSC) Modell wird der Analyse zu Grunde gelegt und ermöglicht eine akkurate Beschreibung, der im AGN Jet auftretenden, Synchrotron Prozesse und inversen Compton-Streuung, sowie die Abschätzung physikalischer Charakteristiken der Quelle. Es stellt sich heraus, dass die Spektren von M87, NGC 1275, Pictor A und Centaurus A mit demselben SSC Modell gut beschrieben werden können und relativ konsistente Werte für physikalische Größen, wie zum Beispiel den Doppler-Faktor oder die Magnetfeldstärke liefern.

Zur genaueren Charakterisierung der aus der Annihilation dunkler Materie resultierenden diffusen Emission, werden die SED der Radiogalaxien zusätzlich mit einem Modell für dunkle Materie gefittet. Die daraus resultierende, geschätzte Teilchenmasse für dunkle Materie liegt mit $m_\chi = 4.7$ TeV innerhalb des vorhergesagten Bereiches. Die hochdichten Regionen in der Nähe der schwarzen Löcher des AGN liefern ideale Voraussetzungen zur Detektion dieser Signaturen. Des Weiteren wurde herausgefunden, dass etwaige Unterschiede zwischen der erwarteten und der beobachteten Emission in den Spektren einiger Radiogalaxien mittels einer Kombination aus SSC Modell und dunkler Materie Modell erklärt werden können. Unter der Annahme, dass die der Annihilation dunkler Materie zu Grunde liegende Emission zeitlich konstant bleibt, stellen zum einen die Kombination des SSC- und dunkler Materie Modells, sowie die Erkenntnis, dass Charakteristiken dunkler Materie durch ähnliche Multi-Wellenlängen-Experimente während zukünftiger, emissionsarmer Zustände gefunden werden können, die wesentlichen Ergebnisse dieser Arbeit dar.

Das Sample der Radiogalaxien wird anschließend erweitert, so dass es alle vom Fermi-LAT detektierte und Gammastrahlung emittierende Radiogalaxien umfasst. Im Anschluss daran wird eine Berechnung der aus dem Kernbereich stammenden, und der totalen Radioluminosität, sowie der Gammastrahlungs-Luminosität durchgeführt. Ein künftiger Schritt zur Erweiterung dieser Arbeit wäre die Abschätzung der Gammastrahlungs-Luminositätsfunktion von Radiogalaxien und deren prozentualer Beitrag zum totalen IGRB, basierend auf der weitläufig akzeptierten Annahme, dass eine vernünftige Abschätzung der Gammastrahlungs-Luminositätsfunktion einer Population

mittels einer angemessenen Skalierung ihrer Radio-Luminositätsfunktion erreicht werden kann, da die Gammastrahlungs-Luminosität und die Radioluminosität stark miteinander korrelieren. Diese Arbeit hat die hierfür benötigten Grundlagen für diese Art von Berechnung gelegt, indem sie die Theorie und die ersten Schritte darlegt.

Es ist die Hoffnung, dass der große Umfang der zusammengetragenen Daten, deren Simultanität, und die Anwendung einer konsistenten Analyseverfahren für das gesamte Sample eine verbesserte Grundlage für zukünftige Berechnungen des Beitrages dieser Population zum IGRB leistet, sowie strengere Anforderungen für Multi-Wellenlängen-Experimente.

Abstract

Although the contribution to the Isotropic Gamma-Ray Background (IGRB) from unresolved extragalactic objects has been studied for many years, its exact composition and origin are as of yet unknown. It is suspected that diffuse processes such as dark matter annihilation contribute to the total IGRB, as well as unresolved γ -ray emission from Active Galactic Nuclei (AGN), including radio galaxies. Radio galaxies are a source class that emit strongly at radio wavelengths, some of which have also been detected at γ -ray wavelengths by the Fermi Large Area Telescope (Fermi-LAT), and by very high energy γ -ray Cherenkov telescopes. It is thought that due to the orientation of their jets, radio galaxies are detected less numerously at γ -ray energies than blazars. Furthermore, only a small number of radio galaxies have been detected at γ -ray energies though it is considered that others do as well. It is for these reasons that γ -ray emitting radio galaxies, an interesting and elusive class of objects, are selected for investigation in this work.

In order to reach the goal of better understanding diffuse processes, it is necessary to model the radio galaxy spectral energy distributions (SEDs). As AGN emission is variable with respect to time, it is critical to use simultaneously collected observations. Calculation of the SED based on simultaneous, multiwavelength data across the electromagnetic spectrum produces a reasonably accurate representation of the state of an object in a given time range. The γ -ray emitting radio galaxies M 87, NGC 1275, Pictor A, and Centaurus A are selected here based on having been detected in very high energy γ -rays by Cherenkov telescopes, as well as in other wavelengths. A uniquely consistent analysis approach is applied, in which each radio galaxy is analyzed the same way using simultaneously collected data. This approach sets it apart from other studies.

Fermi-LAT raw data for each source in the sample is analyzed in time ranges which directly overlap the very high energy γ -ray Cherenkov observations, as well as several other wavelength ranges. A synchrotron self-Compton (SSC) model is applied, which provides accurate treatment of synchrotron and inverse-Compton processes occurring in the jets of AGN, while estimating physical characteristics of the source. It is found that the spectra of M 87, NGC 1275, Pictor A, and Centaurus A can be well described by the same SSC model, producing values for the physical characteristics such as the doppler factor and magnetic field, which are relatively consistent with each other.

In order to characterize the diffuse emission from dark matter self-annihilation, the radio galaxy SEDs are also fit with a dark matter model, resulting in an estimated dark matter particle mass of around $m_\chi = 4.7$ TeV which lies within predicted ranges. The highly dense regions near the black holes of AGN provide the optimal conditions for detecting these signatures. It is also found here that discrepancies between the expected emission and the observed emission in the spectra of some radio galaxies can be explained using the combined SSC and dark matter model. As emission from dark matter annihilation is expected to remain steady with respect to time, a key feature of this work is the novelty of the combined SSC and dark matter model, and the finding that dark matter characteristics may be revealed through similar multiwavelength analyses during future low emission states of the AGN.

The radio galaxy sample is then extended to include all γ -ray emitting radio galaxies detected by the Fermi-LAT, and a calculation of the core radio, total radio, and γ -ray luminosities is followed through. A future step in extending this work would be to estimate the γ -ray luminosity function of radio galaxies and their percent contribution to the total IGRB, based on the widely agreed upon assumption that a reasonable estimate of the γ -ray luminosity function of a population can be attained by appropriately scaling its radio luminosity function, as γ -ray luminosities and radio luminosities are strongly linearly correlated. This work has also provided the basis for such a calculation by outlining the theory and initial steps.

It is the hope that the vast scope of the gathered data, its simultaneity, and the use of consistent analysis methods across the sample, will provide an improved foundation for a future calculation of the contribution of this population to the IGRB, as well as encourage stricter requirements for multi-wavelength studies.

Dedicated to Dad

For DFD

Contents

Zusammenfassung	iii
Abstract	vii
Contents	xiii
1 Introduction and motivation	1
1.1 Introduction	1
1.2 Active galactic nuclei and their unification	4
1.2.1 Blazars	6
1.2.2 Radio galaxies	6
1.3 Physics	7
1.3.1 Jet relativistics and beaming	7
1.3.2 Radiation mechanisms	10
1.4 Spectral modeling	14
1.5 Dark matter	15
1.5.1 AGN as dark matter laboratories	16
1.5.2 A brief mentioning of supersymmetry	16
1.5.3 Summary	18
2 Methods	21
2.1 Introduction	21
2.2 Multiwavelength instrumentation	22
2.2.1 The Very Long Baseline Array	22
2.2.2 The Long Baseline Array	23
2.2.3 Chandra	24
2.2.4 Swift-UVOT, Swift-XRT, and Swift-BAT	25
2.2.5 Suzaku	26
2.2.6 The Fermi Large Area Telescope	28
2.2.6.1 Mission and data	28
2.2.6.2 Detector design	30
2.2.7 MAGIC	32
2.2.8 VERITAS	33
2.2.9 H.E.S.S.	34
2.2.10 The joint campaign of Cherenkov detectors	35
2.2.11 Archival data	35

2.3	Collection of simultaneous multiwavelength data	36
2.3.1	Simultaneous data	36
2.3.2	Sample selection	36
2.4	Analysis of raw Fermi-LAT data	37
2.5	Synchrotron self-Compton multiwavelength modeling	40
2.5.1	The one-zone SSC model	41
2.5.2	The two-zone SSC model by Weidinger et al.	41
2.5.3	Other models to one and two-zone SSC	43
2.6	Dark matter annihilation modeling	44
2.6.1	Prompt pion emission	44
2.6.2	Inverse-Compton emission	45
2.7	Summary	46
3	M 87	47
3.1	Introduction	47
3.2	Collection of simultaneous multiwavelength data	48
3.3	Results of Fermi Large Area Telescope analysis	50
3.3.1	Comparison of results	53
3.4	Results of multiwavelength analysis	54
3.5	Results of dark matter analysis	55
3.6	Summary	57
4	NGC 1275	59
4.1	Introduction	59
4.2	Collection of simultaneous multiwavelength data	60
4.3	Results of Fermi Large Area Telescope analysis	62
4.3.1	Comparison of results	65
4.4	Results of multiwavelength analysis	66
4.4.1	Comparison of results	67
4.5	Results of dark matter analysis	68
4.6	IC 310	71
4.6.1	Collection of simultaneous multiwavelength data	71
4.6.2	Results of Fermi Large Area Telescope analysis	71
4.7	Summary	72
5	Pictor A	73
5.1	Introduction	73
5.2	Collection of simultaneous multiwavelength data	73
5.3	Results of Fermi Large Area Telescope analysis	75
5.3.1	Comparison of results	78
5.4	Results of multiwavelength analysis	79
5.5	Summary	82
6	Centaurus A	83
6.1	Introduction	83
6.2	Collection of simultaneous multiwavelength data	84
6.3	Results of Fermi Large Area Telescope analysis	86
6.4	Results of multiwavelength analysis	87

6.4.1	Comparison of results	88
6.4.2	Other possible origins for VHE γ -ray emission from Centaurus A	89
6.5	Summary	90
7	Discussion	91
7.1	Introduction	91
7.2	Spectral energy distributions of radio galaxies	91
7.2.1	Other explanations for VHE γ -ray emission	93
7.2.1.1	Multiple zone SSC	93
7.2.1.2	Isotropic halo of electrons in the Interstellar Medium	93
7.2.1.3	PeV neutrinos and UHECRs	93
7.3	Dark matter annihilation in radio galaxies	94
7.3.1	Future dark matter work	95
7.4	Calculation of γ -ray luminosities	95
7.5	Collection of core radio data	99
7.6	Calculation of core and total radio luminosities	104
7.7	Luminosity function and the isotropic γ -ray background	105
7.7.1	Correlation between core radio luminosity and γ -ray luminosity	107
7.7.2	Selection of a reliable total radio luminosity function	108
7.7.3	Transformation of radio luminosity function frequency	110
7.7.4	Transformation of radio luminosity function cosmology	110
7.7.5	Selection of a reliable core radio luminosity function	111
7.7.6	Correlation between core radio luminosity and total radio luminosity	111
7.7.7	Calculation of the γ -ray luminosity function of the population	112
7.7.8	Calculation of diffuse γ -ray emission of the extended population	113
7.8	Alternate theories for the origin of the IGRB	113
7.9	Summary	114
8	Summary	115
A	Fermi Large Area Telescope analysis	117
A.1	Raw results for each object in the region of interest	117
A.1.1	M 87	117
A.1.2	NGC 1275	121
A.1.3	Pictor A	124
A.2	Spectral fit results	130
A.2.1	M 87 - power law	130
A.2.2	NGC 1275 - log parabola	130
A.2.3	Pictor A - power law	130
A.2.4	Centaurus A - power law	130

B Calculations	131
B.1 Derivation of the luminosity distance d_L	131
B.2 Calculation of $\alpha_{R,core}$ from TANAMI measurements	131
B.2.1 Pictor A	133
B.2.2 Centaurus A	133
B.2.3 OH -342 (Trial 1)	133
B.2.4 OH -342 (Trial 2)	134
B.3 Extrapolation of TANAMI and MOJAVE $S_{R,core}$ from various frequencies to 5 GHz	134
B.3.1 Pictor A	135
B.3.2 Centaurus A	135
B.3.3 OH -342 (Trial 2)	135
B.3.4 NGC 1275	135
B.3.5 M 87	135
B.3.6 NGC 6251	136
B.4 Calculation tables for d_L , L_γ , $L_{R,core}$ and $L_{R,tot}$	136
Bibliography	139
Acknowledgements	153

Chapter 1

Introduction and motivation

1.1 Introduction

The discovery of a diffuse background of gamma-rays (γ -rays) filling the universe in every direction was in 1972 by the OSO-3 satellite [1], and the γ -ray detection of astrophysical point sources, one of the most notable discoveries in the history of astronomy [2]. The first dedicated sky survey of γ -ray emitting sources was conducted by the COS-B satellite [2]. Since then, the nature of this background radiation has been under critical investigation [3], and has heralded the invention of new spaceborne and ground-based telescopes. Due to our position on earth in the Milky Way galaxy, this background consists of a galactic component as well as an extragalactic component. The galactic γ -ray background can originate from cosmic rays interacting with local interstellar radiation or gas [4]. The extragalactic component, currently referred to as the Isotropic Diffuse Gamma-ray Background (IGRB), can be partly accounted for by unresolved emission from point sources outside of our galaxy, however the origin of the remaining fraction is still unknown [5], [6].

γ -ray point sources such as Active Galactic Nuclei (AGN) can accelerate particles to the highest energies yet known. Many of the sources have not been matched to sources emitting in lower energy ranges, as detected by the existing suite of radio, optical, ultraviolet and X-ray telescopes, and are therefore deemed unidentified γ -ray sources. The need for multiwavelength studies in unifying γ -ray emitting sources with their counterparts as well as in exploring their nature, is present [2].

Historical observations by radio, optical, UV, and X-ray telescopes between 10^{-6} eV and 600 keV of blazars did not allow deep exploration of the γ -ray emission mechanism in AGN. The Energetic Gamma-Ray Experiment Telescope (EGRET), aboard the Compton Gamma-Ray Observatory (CGRO), made observations between 20 MeV and 30 GeV [7], though with a smaller detector area, and moderate sensitivity which was one of the reasons for the incomplete understanding of the emission mechanisms [8]. An improvement has been made in the detector area and sensitivity by way of the Fermi Large Area Telescope (Fermi-LAT), which can detect γ -rays above 10 GeV with a sensitivity two orders of magnitude greater than what was capable with its predecessor EGRET [8]. Together with the MAGIC, VERITAS, and H.E.S.S. Cherenkov detectors, a view of the sky between 20 MeV and 50 TeV has become attainable, as well as a probe into the physical processes which produce very high energy (VHE) γ -rays [8].

Recent results from four years of data collection by the Fermi-LAT has revealed a measured IGRB from 100 MeV to 820 GeV [6]. The study has shown that 10% to 50% of the detected IGRB originates from blazars [5]. The IGRB below 10 GeV, is partly accounted for by flat spectrum radio quasars (FSRQs) (8 to 11%), and BL Lacertae (BL Lac) objects (10%), whereas the high energy part of the IGRB above 100 GeV is heavily explained by BL Lac objects [5]. Diffuse processes, such as γ -rays from dark matter annihilation, star formation, or ultra high energy cosmic rays (UHECRs) interacting with the extragalactic background light (EBL) can constitute up to 28% of the IGRB [5]. One of the focuses of this work will be to explore the annihilating dark matter particle characteristics. Star forming galaxies (SFGs) generate γ -rays through the interaction of cosmic rays resulting from a high rate of formation, with the interstellar medium. They have been estimated to contribute 4 to 23% of the total IGRB [5], and misaligned active galactic nuclei (MAGN) such as radio galaxies, approximately 20% [9].

Since observational data for radio galaxies is not as abundant as for blazars, correlation studies are employed to extrapolate γ -ray luminosity predictions from measured radio luminosities, and subsequently the luminosity functions and contributions to the IGRB [6]. These studies have estimated that the detected γ -ray emitting radio galaxies must be a subset of a much larger population, which is as of yet unresolved, and contributes to the IGRB (above 20%) [9], [10], [5].

Overall however, direct detection and extrapolation studies of γ -ray emitting populations have not been able to explain the entirety of the IGRB, even while considering added contributions from diffuse processes. The purpose of this work is to examine a sample of γ -ray emitting radio galaxies in detail and with consistent analysis methods, using simultaneous data across the multiwavelength spectrum, in order to gain insight into their emission mechanisms, and provide the basis for a calculation of the diffuse γ -ray emission of the extended population which would contribute to the IGRB. Radio galaxies are selected for study as they may not be as numerous detected in γ -rays as blazars due to the orientation of their jets [5], and therefore provide a challenge. As AGN emission is variable with respect to time, calculation of the spectral energy distributions (SEDs) based on simultaneous, multiwavelength data across the electromagnetic spectrum is important and produces a reasonably accurate representation of the state of the object in a given time range. In order to achieve this, raw γ -ray data from the Fermi-LAT is analyzed in time ranges simultaneous to very high energy γ -ray Cherenkov detectors such as MAGIC, VERITAS, and H.E.S.S., and X-ray detectors such as Suzaku and Swift-XRT, as well as optical and ultraviolet detectors. Studying the multiwavelength SEDs of γ -ray emitting sources has the potential for determining the physical parameters of the particle distributions, such as the magnetic field strength and doppler factor [11]. The potential for dark matter annihilation, the signatures of which are not variable with respect to time, is also probed where possible, as it is a diffuse process which can also contribute to the total IGRB.

The thesis outline is as follows:

- (1) Introduce AGN, blazars and radio galaxies as well as the physics governing their emission mechanisms
- (2) Understand dark matter and the γ -ray signal produced by dark matter annihilation in the vicinity of AGN black holes
- (3) Detail the multiwavelength instrumentation used to gather observational data
- (4) Highlight the importance of simultaneous multiwavelength observational data and arrival at the selected sample of γ -ray emitting radio galaxies
- (5) Detail the raw data analysis technique, synchrotron self-Compton (SSC) modeling technique, and dark matter annihilation modeling technique
- (6) In dedicated chapters for each γ -ray emitting radio galaxy in the sample, explain the simultaneous multiwavelength data collection, conduct Fermi-LAT raw data analysis, conduct multiwavelength SSC analysis, and conduct

dark matter analysis using a combined model

(7) Summarize the extracted SED and dark matter characteristics

(8) Calculate the γ -ray luminosities and core and total radio luminosities of an extended γ -ray emitting radio galaxy population

(9) Set up the basis for a diffuse γ -ray emission calculation for the extended population

The specific sample will be arrived upon based on maximum availability of observational data at several energies including very high energy data, in this case, the subset of γ -ray emitting radio galaxies M 87, NGC 1275, Pictor A and Centaurus A. The novelties of this work lie in its use of simultaneous data and identical methods across the sample, for Fermi-LAT analyses, spectral analyses, and dark matter analyses, as well as its scope, and the large collection of gathered data.

1.2 Active galactic nuclei and their unification

The types of observed AGN thus far span from radio galaxies to seiyfert galaxies to blazars, and more. The widely accepted unification model by Urry and Padovani [12] postulates that all the classes of sources are in fact the same, but appear to have differing characteristics due to the jet-to-line-of-sight angle. The anatomy of an active galaxy includes in every case six primary features: a relativistic jet, obscuring torus, broad line region, narrow line region, accretion disk, and black hole [13]. The relativistic plasma jet is a formation of magnetized plasma that has a relativistic bulk velocity [8]. It can extend from between tens of kpc to one Mpc, and is formed within 100 Schwarzschild radii of the central black hole [12]. The particle composition within the jet is the subject of many modeling approaches, to be discussed in §2.5. The torus, or obscuring torus, is composed of dust and gas and can block the broad line region, which is composed of gas clouds moving with high velocity, depending on the orientation of the observer. The narrow line region is composed of gas clouds moving with lower velocity and is considerably farther from the black hole than the broad line region. As matter falls towards the immense gravity of the supermassive black hole, it forms a rotating luminous accretion disk which emits radiation across the electromagnetic spectrum from optical wavelengths to X-rays, due to the interaction of charged particles flowing rapidly in the disk. The supermassive black hole is the centrally located engine that powers the system; its mass

can range from 10^6 to 10^{10} solar masses ($1 M_{\odot} = 1.989 \times 10^{30}$ kg), as shown in Figure 1.1. The parameters of each feature vary. A supermassive black hole of mass $10^8 M_{\odot}$ can have a narrow line region 10^{13} km to 10^{15} km in length, an obscuring torus inner radius of 10^{12} km, and a black hole radius of 10^8 km. It is worth noting that radio jets can extend to lengths longer than individual galaxies themselves, from 10^{12} to 10^{19} km [12].

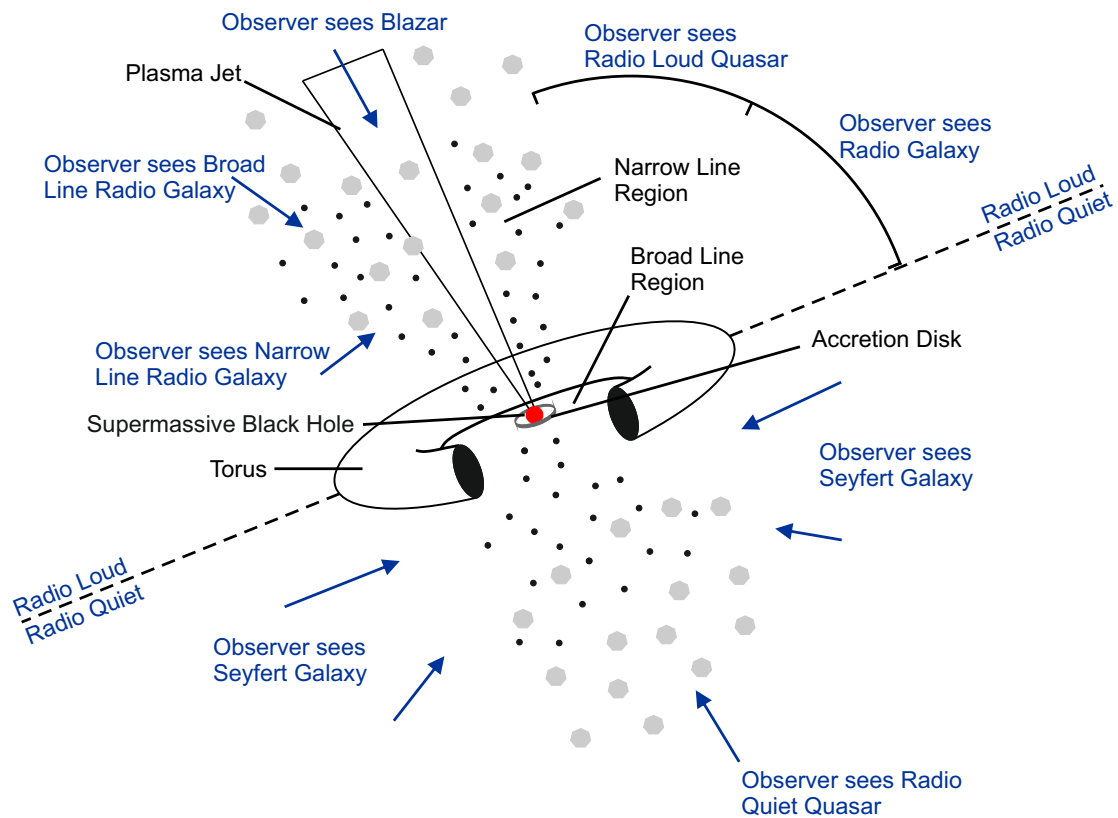


Figure 1.1: Unification of AGN, not to scale. The viewing angle of the observer with respect to the jet axis determines what class of object is seen. Original image, modified from [12] and [14].

Active galactic nuclei can be further divided as being radio quiet or radio loud. Radio quiet galaxies include seyfert galaxies and quasars. Within the radio loud classification, there exist radio galaxies, quasars and blazars, blazars being characterized by a jet pointing direction that is nearly along the line-of-sight [8], [5], as well as nonthermal radiation from within the jet, that is doppler boosted and variable with respect to time [8].

1.2.1 Blazars

Blazars are then classified as being either BL Lac objects or FSRQs [8] depending on the absence or presence of strong broad emission lines in the optical to ultraviolet energy range. They are also categorized depending on the energy of the first peak in the double-hump spectral energy distribution typical for blazars; high synchrotron peaked (HSP), intermediate synchrotron peaked (ISP), or low synchrotron peaked (LSP). BL Lacs are divided into HSP objects and ISP plus LSP objects, by a ratio of approximately 1 to 1 [5]. FSRQs are nearly entirely LSP objects [5]. High frequency peaked BL Lac objects (HBLs) have the lower synchrotron peak in the double-hump spectrum between ultraviolet and X-ray energies, and the higher inverse-Compton peak between GeV and TeV energies [15]. The radiation emitted by blazars range over the entire electromagnetic spectrum, i.e. 10^{-6} eV to 10 TeV, with an emitted power varying by up to two orders of magnitude [8]. Blazar variability has been observed on timescales as short as minutes and as long as tens of years, with the short timescale variability understood to originate due to the small jet to line-of-sight angle [16].

1.2.2 Radio galaxies

Radio galaxies are misaligned active galactic nuclei, their plasma jets at larger angles to the line-of-sight. Due to doppler boosting effects, radio galaxies may present weaker luminosities than blazars and therefore might not be as numerously detected [5]. They do however emit strongly at radio wavelengths, with the maximum luminosity at radio wavelengths, and are generally identified with sources in radio catalogs. Radio galaxies are generally elliptical though can have more complex morphology.

There are two classifications within radio galaxies, depending on their luminosity. Low luminosity radio galaxies have their highest luminosity feature nearer to the black hole, and are designated as FRI, whereas high luminosity FR II radio galaxies have radio lobes which extend away from the black hole, and have luminosity peaks at the outer edges, or in distinct regions, deemed hot spots [12]. The frequency cutoff between FRI and FR II radio galaxies is approximately 178 MHz [12].

1.3 Physics

1.3.1 Jet relativistics and beaming

Doppler beaming, also known as doppler boosting, can be considered the apparent anisotropy when observing the relativistic-speed plasma flows of a two-sided AGN jet that appears as being one-sided [17]. This effect is in part analogous to a ship observing the light beam emanating from a lighthouse; the beam appears more luminous when directed toward the observer than it does when directed away. Quantities that are descriptive of the AGN jet in the frame of the jet, are beamed and thus transformed into apparent quantities by the time they reach the observer. The factors which determine the beaming are [18]:

The Lorentz factor γ , where v is the velocity of the jet and c is the speed of light:

$$\gamma = \frac{1}{\sqrt{1 - \frac{v^2}{c^2}}} \quad (1.1)$$

The jet-to-line-of-sight angle θ , and the doppler factor, δ :

$$\delta = \frac{\sqrt{1 - \frac{v^2}{c^2}}}{1 - \frac{v}{c} \cos \theta} = \frac{1}{\gamma(1 - \beta_o \cos \theta)} \quad (1.2)$$

The velocity in the frame of the jet is defined as

$$\beta_o = \frac{v}{c} \quad (1.3)$$

Quantities describing the AGN jet in the observer frame are the observed velocity, observed brightness temperature, and observed luminosity, respectively:

$$\beta = \frac{\beta_o \sin \theta}{1 - \beta_o \cos \theta} \quad (1.4)$$

$$T = \delta T_o \quad (1.5)$$

$$L = \delta^n L_o \quad (1.6)$$

[18] where β_o , T_o , and L_o are the speed, temperature, and luminosity in the jet-frame, and n is a quantity affected by the spectral index [17].

From Figure 1.2 and Table 1.1 it becomes evident that as the jet-to-line-of-sight angle increases, the doppler factor decreases rapidly. In the case of radio galaxies, approaching an inclination angle of 90° causes the luminosity of the object to be greatly dimmed, such that there is more emission seen from the giant radio lobes, and the emission from the jet may be nearly invisible in γ -rays.

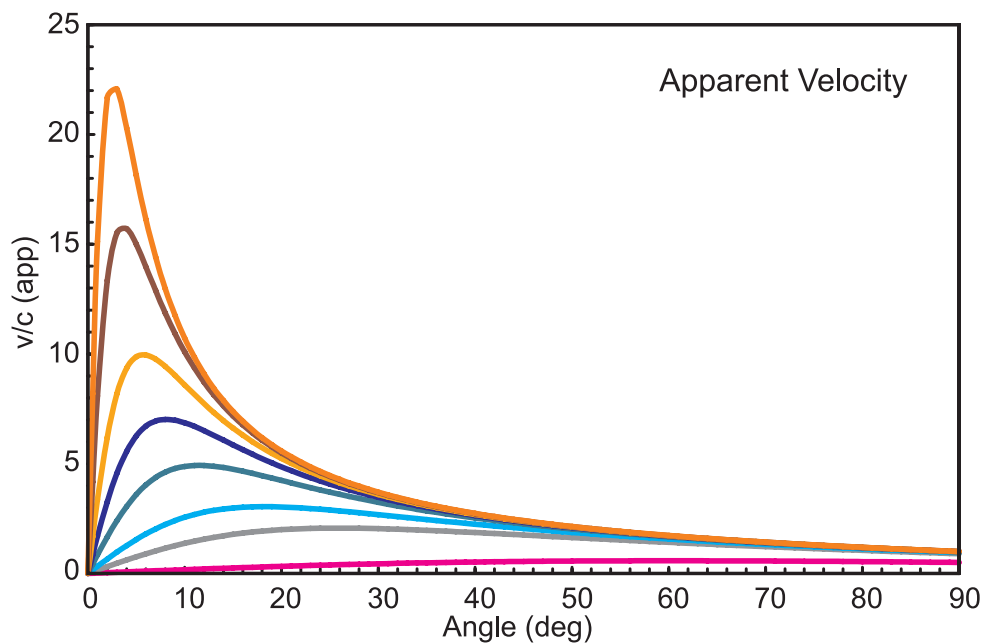


Figure 1.2: Plot of apparent or observed velocity with increasing jet-to-line-of-sight angle for varying values of β_o by Kellerman et al. 2007 [17]. See Table 1.1.

Table 1.1: Examples of doppler factor values with varying jet-to-line-of-sight angles and velocities. Lorentz factors and velocities as in [17].

Line	β_o	γ	θ	δ
Magenta	0.5	1.15	0°	1.74
Magenta	0.5	1.15	30°	1.53
Magenta	0.5	1.15	45°	1.35
Magenta	0.5	1.15	90°	0.87
Grey	0.9	2.3	0°	4.35
Grey	0.9	2.3	30°	1.97
Grey	0.9	2.3	45°	1.20
Grey	0.9	2.3	90°	0.43
Light Blue	0.95	3.2	0°	6.25
Light Blue	0.95	3.2	30°	1.76
Light Blue	0.95	3.2	45°	0.95
Light Blue	0.95	3.2	90°	0.31
Green	0.98	5.0	0°	10.00
Green	0.98	5.0	30°	1.32
Green	0.98	5.0	45°	0.65
Green	0.98	5.0	90°	0.20
Dark Blue	0.99	7.1	0°	14.08
Dark Blue	0.99	7.1	30°	0.99
Dark Blue	0.99	7.1	45°	0.47
Dark Blue	0.99	7.1	90°	0.14
Light Orange	0.995	10.0	0°	20.00
Light Orange	0.995	10.0	30°	0.72
Light Orange	0.995	10.0	45°	0.34
Light Orange	0.995	10.0	90°	0.10
Brown	0.998	15.8	0°	31.65
Brown	0.998	15.8	30°	0.47
Brown	0.998	15.8	45°	0.22
Brown	0.998	15.8	90°	0.06
Dark Orange	0.999	22.4	0°	44.64
Dark Orange	0.999	22.4	15°	1.27
Dark Orange	0.999	22.4	30°	0.33
Dark Orange	0.999	22.4	45°	0.15
Dark Orange	0.999	22.4	60°	0.09
Dark Orange	0.999	22.4	75°	0.06
Dark Orange	0.999	22.4	90°	0.04

1.3.2 Radiation mechanisms

Emission and absorption processes in general come about as a result of the interactions between charged particles, photons and fields. The accretion disks of AGN for example emit predominantly thermal radiation, and the synchrotron and inverse-Compton mechanisms are responsible for generating very high energy photons in the plasma jet [18].

Matter that is in thermal equilibrium is in a state of balance and has no net gain or loss in energy i.e. is an opaque blackbody, and will emit a spectrum of thermal radiation [19]. In AGN these are referred to as thermal photons. Nonthermal photons in AGN are generated through acceleration by astrophysical phenomena, such as by a black hole engine.

Coherent scattering, also known as elastic or Thomson scattering occurs between a charged particle moving at speeds much lower than c , and a photon. The incident and final energies E_1 and E_2 of the photon are approximately equal [18]. In the case of Compton scattering however, the charged particle is moving at speeds comparable to the photon, and may have a rest mass energy comparable to that of the photon, and the photon transfers some of its energy to the particle so that

$$E_1 < E_2 \quad (1.7)$$

with a specific loss in energy of

$$\Delta E = \frac{hc}{\Delta\lambda} \quad (1.8)$$

where the change in wavelength depends on the scattering angle

$$\Delta\lambda = \frac{h}{mc}(1 - \cos\theta) \quad (1.9)$$

(not to be confused with θ in equation 1.2) and the interaction cross-section is thus lower than in coherent scattering. Rearranging the incoming photon energy E_1 allows ϵ to be defined as

$$\epsilon = \frac{h\nu_1}{mc^2} = \frac{E_1}{mc^2} \quad (1.10)$$

When the incoming photon energy is quite small in comparison to the rest mass of the free charged particle, the total cross-section approaches the Thomson cross-section σ_T (Table 1.2). The total cross-section of interaction for photons with energies lower than $E_1 \simeq 200$ keV can be approximated by

$$\sigma_{KN} \simeq \sigma_T \frac{1 + 2\epsilon + 1.2\epsilon^2}{(1 + 2\epsilon)^2} \quad (1.11)$$

When the incoming energy is much larger than the rest mass of the free charged particle, $E_1 \gg mc^2$, the total cross-section can be approximated by

$$\sigma_{KN} \simeq \frac{3}{8\epsilon} \sigma_T \left(\ln 2\epsilon + \frac{1}{2} \right) \quad (1.12)$$

[18]. Inverse-Compton scattering involves the interaction of the same objects as in coherent scattering however with an energy transfer occurring from the charged particle to the photon; as the charged particle has very high energy and moves at relativistic speeds.

Synchrotron emission is produced when a charged particle experiences a force due to proximity to a magnetic field \vec{B} , causing it to emit photons while it consequently spirals and accelerates. A particle that holds a quantity of charge $q = Ze$, where Z is the atomic number and e is the elementary charge -1.602×10^{-19} Coulombs, and has a Lorentz factor as in equation 1.1, will experience the force [18]

$$\frac{d}{dt}(\gamma m \mathbf{v}) = \frac{Ze}{c} (\vec{v} \times \vec{B}) \quad (1.13)$$

resulting in acceleration perpendicular to the direction of motion of the charged particle. This synchrotron radiation propagates in the shape of a narrow cone centred on the velocity vector of the charged particle i.e. it does not propagate isotropically, with the cone radius being narrower for higher Lorentz factors. β denotes the pitch angle which is measured between the magnetic field and the direction of particle motion \vec{v} . The scenario in which the

same population of very high energy charged particles interact with the synchrotron photons, upscattering them to even higher energies, is deemed the synchrotron self-Compton effect [18].

Finally, pair production is the generating of a particle with its anti-particle owing to the condition that the originating photon has an energy greater than that of the sums of the rest mass energies of the pair. The lowest-mass example is the electron-positron pair, for which the originating photon must have an energy $E > 1022 \text{ keV}$ [18]. To maintain momentum conservation, pair production occurs near another massive particle and the momentum carried by the photon is imparted onto that massive nucleus; other conserved quantities are angular momentum, lepton number, electric charge and of course energy [18]. See Table 1.2 for an overview of the aforementioned radiation mechanisms [18].

Table 1.2: Radiation mechanisms. Cross-sections and interaction conditions for various radiative processes [18]. Subscript ph refers to a photon and subscript p refers to a charged particle. $r_0 = q^2/mc^2$ denotes the radius of a charged particle, such as an electron.

COHERENT SCATTERING	
Interacting Bodies	Photon and free charged particle
Conditions	$v_p \ll c, E_{ph} = h\nu_{ph} \ll m_p c^2$
Differential Cross-section	$\frac{d\sigma}{d\Omega} = \frac{1}{2} (1 + \cos^2\theta) r_0^2$
Total Cross-section	$\sigma_T = 2\pi \int_0^\pi \frac{d\sigma}{d\Omega} \sin\theta d\theta = \frac{8\pi}{3} r_0^2$
COMPTON SCATTERING	
Interacting Bodies	Photon and free charged particle
Conditions	$E_2 = \frac{E_1}{1 + \frac{E_1}{mc^2}(1 - \cos\theta)}, E_{ph} = h\nu_{ph}$ comparable to $m_p c^2$
Total Cross-section	$\sigma_{KN} = \frac{3\sigma_T}{4} \left(\frac{1+\epsilon}{\epsilon^3} \left(\frac{2\epsilon(1+\epsilon)}{1+2\epsilon} - \ln(1+2\epsilon) \right) + \frac{\ln(1+2\epsilon)}{2\epsilon} - \frac{1+3\epsilon}{(1+2\epsilon)^2} \right)$
Summary	As frequency increases, Compton scattering efficiency decreases; Klein-Nishina effect has cross-sections reduced at high photon energies
INVERSE-COMPTON SCATTERING	
Interacting Bodies	Photon and free charged particle
Conditions	$E_{ph} = h\nu_{ph} \ll m_p c^2/\gamma$, therefore σ_T applies
Differential Cross-section	$\frac{d\sigma}{d\Omega} = \frac{1}{2} (1 + \cos^2\theta) r_0^2$
Total Cross-section	$\sigma_T = 2\pi \int_0^\pi \frac{d\sigma}{d\Omega} \sin\theta d\theta = \frac{8\pi}{3} r_0^2$
SYNCHROTRON EMISSION	
Interacting Bodies	Charged particle and magnetic field
Conditions	Acceleration perpendicular to direction of motion \vec{v} . For multi-particle scenario, pitch angles β and power are averaged to produce a total synchrotron luminosity
Synchrotron Luminosity	$L_{Synch} = \frac{4Z^4 e^4 B^2 E^2}{9m^4 c^7}$

Table 1.2 - Radiation Mechanisms - Continued

Example	For highly relativistic electron or positron with magnetic energy density $U_B = \frac{B^2}{8\pi}$, and approximation that $\frac{v}{c} \approx 1$, $L_e = \frac{4}{3}\sigma_T c \gamma^2 U_B \approx 2.7 \times 10^{-14} \text{cm}^3 \text{s}^{-1} \gamma^2 U_B$
SYNCHROTRON SELF-COMPTON EMISSION	
Interacting Bodies	Charged particle, magnetic field, same charged particle again
Summary	Synchrotron emission photons become seed photons for inverse-Compton scattering by original electron population which was accelerated to output synchrotron emission photons
Conditions	Plasma must be optically thick to allow interaction between electron population and Synchrotron photons
SSC Luminosity Example	$L_{SSC} = L_{Synch} \frac{U_{radio}}{U_B}$, where U_{radio} denotes the energy density of radio-wavelength photons being upscattered
PAIR PRODUCTION	
Interacting Bodies	Photon, massive particle, and particle anti-particle pair
Conditions	$E_{ph} = h\nu_{ph} > 2m_p c^2$
Example	$\gamma + e^- \rightarrow e^- + e^+ + e^-$
Total Cross-section	$\sigma_{\gamma e^-}(E) = \frac{3}{8\pi} \alpha \sigma_T \frac{28}{9} \ln \frac{2E}{m_e c^2} - \frac{218}{27}$ for $\frac{E}{m_e c^2} \gg 4$

1.4 Spectral modeling

The production of multiwavelength radiation including γ -rays in AGN jets is explained by several types of models, two of which are most prominent; leptonic and hadronic models. Leptonic models assume that the jet material is dominated by electrons and positrons which are accelerated by the magnetic

field of the jet and emit synchrotron photons, which in turn upscatter ambient photons through the inverse-Compton mechanism (hence synchrotron self-Compton, or SSC). Within the leptonic scheme an alternative to SSC is external Compton (EC), which has instead of jet leptons emitting synchrotron photons, external photons originating from the accretion disk, or ambient photons which have been collimated into the path of the jet [20]. The main distinguishing factor in recognizing SSC and EC is the observed beaming pattern; EC beaming will be more narrow than SSC beaming [20]. Hadronic models assume that the jet material is dominated instead by protons and neutrons which generate γ -rays by way of inverse-Compton scattering by secondary electrons, shock acceleration, or nuclear interactions [20]. Leptonic SSC modeling will be the model of choice in this work, as well as a type of leptonic-hadronic combined model.

1.5 Dark matter

Dark matter annihilation has long been suspected to produce an observable γ -ray signal [21]. To date there exists a wealth of indirect evidence for dark matter such as galaxy rotation curves, gravitational lensing, and the anisotropy of the cosmic microwave background. Recent results from the Planck experiment measurements of the cosmic microwave background have revealed a Standard Spatially Flat Universe with updated values for the cosmological parameters since the Wilkinson Microwave Anisotropy Probe experiment (WMAP) [22]. The density of baryons in the universe is $\Omega_b h^2 = 0.02205 \pm 0.00028$ and the density of cold dark matter is $\Omega_c h^2 = 0.1199 \pm 0.0027$ [22]. The Hubble constant, or expansion rate, which was previously taken to be between 70 km/s/Mpc and 73 km/s/Mpc, was confirmed by the Planck experiment to be a lower value, $H_o = 67.3 \pm 1.2$ km/s/Mpc. The matter and energy distribution in the universe is 26.8% dark matter, 4.9% normal matter, and 68.3% dark energy [22]. Weakly interacting massive particles (WIMPs) are defined as generic dark matter particles, thought to self-annihilate and produce detectable γ -rays in extragalactic halos and the galactic halo of the Milky Way. The currently accepted WIMP mass range is between a few GeV [23] and 100 TeV [24]. The recent measurement of the IGRB by the Fermi-LAT has constrained the WIMP particle mass more sharply, to between a few GeV to a few tens of TeV [6].

Within the generic WIMPs, the best motivated specific dark matter particle is the neutralino. The hypothesized mass range would allow for a relic dark matter density matching the observed relic density in our present universe. Additionally, it is massive enough to be non-relativistic and form structure through gravitational and weak interactions, and would allow for the dark matter density in the universe of 26.8%. Namely:

neutralinos with masses at the electroweak symmetry breaking scale

$$E_{\text{ew}} = 1/\sqrt{\sqrt{2}G_{\text{F}}} \approx 246 \text{ GeV} \quad (1.14)$$

have undergone thermal freeze-out leading to the relic density

$$\Omega_{\text{dm}}h^2 = 0.1123 \pm 0.0035 \quad (1.15)$$

which agrees with the currently observed relic density [25]. In this work it will be assumed that the dark matter particle is the neutralino.

1.5.1 AGN as dark matter laboratories

Regions with high concentrations of mass, such as galaxy clusters, provide the optimal conditions for detecting neutralino annihilation signatures. The same is true for the dense regions near the black holes of AGN. Thus many indirect dark matter detection studies focus on building the SEDs of these areas, with the primary challenge to distinguish the nonthermal multiwavelength data from the dark matter annihilation signatures, and the additional advantage that γ -ray emission from dark matter remains constant over time, whereas γ -ray emission from the jet processes are variable. In this work, dark matter annihilation in M 87 and NGC 1275 will be modeled.

1.5.2 A brief mentioning of supersymmetry

The particle which serves as a solution to the dark matter problem exists in the Minimal Supersymmetric Model (MSSM) as the Lightest Supersymmetric Particle (LSP). In the Standard Model of particle physics, every particle is described by a mass, charge, and spin, and there exist three generations of matter which describe increasing steps in quark masses [26]. These are the

up and down quarks, the charm and strange quarks, and the top and bottom quarks. Leptons include electrons and electron neutrinos, with increasingly massive muon and tau particles, plus their respective muon neutrinos and tau neutrinos. The gauge bosons or force carriers are considered to mediate the three forces which are accounted for by supersymmetry (SUSY) [26]. In SUSY the photon mediates the electromagnetic interaction, the gluon mediates the strong interaction, and the W and Z bosons mediate the weak interaction. The Higgs boson is thought to induce a scalar field, giving mass to all of these particles [26].

Supersymmetry provides a superpartner particle for every standard model particle, with their spins differing by 1/2. The neutralino in this context would be a massive, neutrally charged particle composed of these constituents, which is stable on cosmological time scales, and has not decayed thus far. There are convenient properties which emerge from squarks, selectrons, and Higgsinos in SUSY, the most important being the convergence of the three aforementioned forces at very high energies [27]. The coupling constants, which represent the strengths of the forces, become equal at energies representing the conditions of the Big Bang in the early universe. The fourth force, gravity, is not explained through SUSY but rather String Theory, which is beyond the scope of this work. The LSP, i.e. the neutralino, is well motivated from a particle physics perspective as being a dark matter candidate.

The neutralino self-annihilates with 100% branching ratio into $b\bar{b}$, W^+W^- , $\tau^+\tau^-$ or $\mu^+\mu^-$ channels [6]. It first produces pairs of standard model particles such as leptons, heavy quarks, and W bosons, and the decay channels resulting from the hadronization of these pairs involve an output of γ -rays and particles [28]:

$$\chi\bar{\chi} \rightarrow \bar{l}l, q\bar{q}, W^+W^- \quad (1.16)$$

$$\pi^0 \rightarrow \gamma + \gamma \quad (1.17)$$

$$\pi^+ \rightarrow \mu^+ + \nu_\mu \quad (1.18)$$

$$\mu^+ \rightarrow e^+ + \nu_e + \bar{\nu}_\mu \quad (1.19)$$

$$\pi^- \rightarrow \mu^- + \bar{\nu}_\mu \quad (1.20)$$

$$\mu^- \rightarrow e^- + \bar{\nu}_e + \nu_\mu \quad (1.21)$$

where equations 1.17, 1.18 and 1.20 are primary emission modes, and equations 1.19 and 1.21 are secondary emission modes [28]. The first of two γ -ray signals which can be detected is the decay of the neutral pion into two γ -rays at very high energy, deemed Prompt Pion Emission. The second γ -ray signal is the upscattering of cosmic microwave background (CMB) photons by highly energetic charged electrons and positrons in the neutralino decay chain, from approximately 3 Kelvin to γ -ray energies:

$$e^{\pm} + \gamma \rightarrow e^{\pm} + \gamma \quad (1.22)$$

This is in fact an inverse-Compton interaction with the CMB photons gaining an energetic kick from the electron or positron [28]. The inverse-Compton energy denoted by E_{IC} is related to the energy of the 3 Kelvin photons E_{3K} through the Lorentz factor

$$E_{IC} = \frac{4}{3} E_{3K} \gamma^2 \quad (1.23)$$

[28]. Therefore a neutral pion peak and inverse-Compton peak can be detected in the tens of GeV energy range of ground-based Cherenkov detectors. This will be seen in §3 and §4.

1.5.3 Summary

In this chapter the goals and strategy of this thesis have been outlined, followed by a background on AGN, unification, jet relativistics and radiation mechanisms. Spectral modeling in general has been introduced, as well as the concept of dark matter and its self-annihilation. The connection between dark matter annihilation and AGN black holes has provided the motivation to search for a γ -ray signal near the estimated mass of the dark matter particle in the SEDs of γ -ray emitting radio galaxies, as will be conducted in the following radio galaxy chapters. These however will be preceded by the

methods chapter, which will detail all the analysis techniques including the dark matter analysis technique.

Chapter 2

Methods

2.1 Introduction

The electromagnetic spectrum defines all frequencies and energies known at present, ranging from extremely low frequency, to radio, microwave, infrared, visible, ultraviolet, soft X-ray, hard X-ray, γ -ray, and very high energy γ -ray frequencies. Recall the relation between the energy, frequency, and wavelength of a particle

$$E = h\nu = h\frac{c}{\lambda} \quad (2.1)$$

where the planck constant, h , is equal to $6.626 \times 10^{-34} \text{ m}^2\text{kg/s}$. Each energy range has seen its own evolution of detectors. As data from several energy ranges is employed in this work, this chapter will be dedicated to explaining the utilized multiwavelength instrumentation. This will be followed by the radio galaxy sample that is of interest, its selection criteria, and the collected simultaneous data. Finally the method for analyzing raw Fermi-LAT data for each galaxy will be presented, as well as the method for modeling the multiwavelength spectral energy distributions of each galaxy, and the method for modeling potential annihilating dark matter in the high density regions of each galaxy.

2.2 Multiwavelength instrumentation

Observational data has been gathered from many telescopes, both ground-based and spaceborne. The following sections summarize locations, energy ranges, and key features of each telescope. They appear in order of increasing detection energy. Special attention is given to the Fermi telescope, as raw data collected over the first two years of operation will be analyzed in time ranges simultaneous to data in other wavelengths.

2.2.1 The Very Long Baseline Array

Detectable energy range: 5×10^{-6} eV to 4×10^{-4} eV (Radio)

The Very Long Baseline Array, known as the VLBA, is an interferometer spread over thousands of kilometers reaching from the western Leeward Islands to Hawaii, with a detectable energy range of 5×10^{-6} eV to 4×10^{-4} eV (radio frequencies). It is made up of ten 25 m antennae radio telescopes, each with a station where signals are amplified and recorded before being sent to the Science Operations Center in New Mexico from where the detectors are actually controlled [29]. As shown in Figure 2.1, the stations are located in the Leeward Islands (Virgin Islands), New Hampshire, Iowa, Texas, New Mexico, Arizona, California, Washington, and Hawaii; the longest line from detector to detector is approximately 8000 km.



Figure 2.1: The Very Long Baseline Array operates on the principle of Very Long Baseline Interferometry (VLBI). This giant radio interferometer has a detectable frequency range of 1.2 GHz to 96 GHz. Image from [30].

Direct imaging of the radio synchrotron radiation from AGN by the VLBA has confirmed that the relativistic outflows from AGN are in fact jets of matter that are highly collimated, and have apparent superluminal speeds of up to $40c$ [31].

The Monitoring of Jets in Active Galactic Nuclei with VLBA Experiments (MOJAVE) program is a specific long term observing campaign designed to further study these relativistic outflows. It investigates the variations in polarization in the AGN jets, and their radio brightness [32]. The sample has 133 AGN in the northern sky, some of the data from which will be used in the chapters to follow.

2.2.2 The Long Baseline Array

Detectable energy range: 3.5×10^{-5} eV and 9.1×10^{-5} eV (Radio)

The Long Baseline Array (LBA) in Australia is a network of radio antennae located in Parkes, Mopra, Hobart, Ceduna, Tidbinbilla, and The Australia Telescope Compact Array (ATCA), with a total detectable energy range of 3.5×10^{-5} eV to 9.1×10^{-5} eV. Tracking Active Galactic Nuclei with Austral Milliarc-second Interferometry, or TANAMI, is a multiwavelength monitoring program that includes these Australian radio detectors as well as TIGO in Argentina, The German Antarctic Receiving Station (GARS O'Higgins) on the South Pole, and The Hartebeesthoek Radio Astronomy Observatory (HartRAO) located in South Africa [33]. See Figure 2.2.

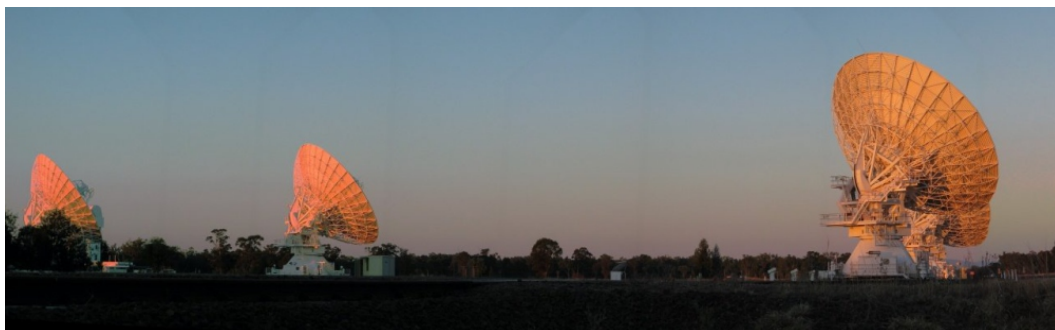


Figure 2.2: The Australia Telescope Compact Array. ATCA is a network of six 22 m radio antennae at the Paul Wild Observatory, participating in the TANAMI program. Image from [34].

The objectives of TANAMI include multifrequency blazar spectral energy distribution studies, therefore there is close collaboration with the Swift mission

(§2.2.4) and the Fermi-LAT mission (§2.2.6) in order to collect simultaneous optical, ultraviolet, X-ray and γ -ray observations [33].

Measurements are taken by TANAMI at 8.4 GHz and 22 GHz, for approximately 60 minutes every four months [33].

2.2.3 Chandra

Detectable energy range: 90 eV to 10 keV (X-ray)

The Chandra X-Ray Observatory is a NASA spacecraft providing a detectable energy range of 90 eV to 10 keV, with a more than 15 year expected life span, launched on July 23 1999. With two solar panel wings extending from the sides of a cone-shaped body, Chandra has a mass of 4790 kg, is 19.5 m from wing-to-wing, 13.8 feet in length and houses four pairs of X-rays mirrors which focus the X-ray beam. It follows an elliptical orbit around the earth, reaching an apogee altitude of 140 000 km. For reference, earth's moon is located at a distance of 384 400 km [35], [36].

As shown in Figure 2.3, there are four scientific instruments aboard the satellite. The High Resolution Camera (HRC) contains millions of lead-oxide tubes through which the incident X-rays produce electron cascades, providing high spatial resolution capabilities [37]. The Advanced Charged Coupled Imaging Spectrometer (ACIS) has an imaging resolution of 0.5 arcseconds over an energy range of 200 eV to 10 keV and provides simultaneous spectroscopy and time-resolved imaging using a Charge-coupled array for spectroscopy, and another Charge-coupled array for imaging [36]. After being focused by the High Resolution Mirror Assembly (HRMA), the incoming X-rays pass through a low energy and a high energy diffraction grating, before reaching the HRC and ACIS. The Low Energy Transmission Grating (LETG) provides spectral resolution in the energy range of 20 eV to 3 keV, and the High Energy Transmission Grating (HETG) provides spectral resolution in the energy range of 400 eV to 10 keV [36].

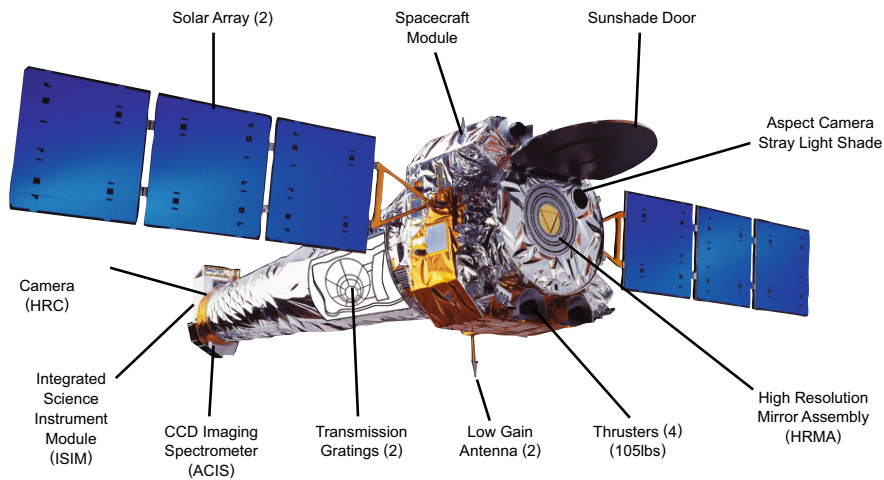


Figure 2.3: The Chandra Telescope. Incoming X-rays are focused by mirrors before passing through the Low Energy Transmission Grating, High Energy Transmission Grating, High Resolution Camera, and Advanced Charged Coupled Imaging Spectrometer. Image modified from [38].

2.2.4 Swift-UVOT, Swift-XRT, and Swift-BAT

Detectable energy range: 200 eV to 150 keV (Optical, ultraviolet, and X-ray)

The Swift Gamma-Ray Observatory is a multiwavelength data collection satellite with three instruments on board, providing a detectable energy range of 200 eV to 150 keV. It was launched by NASA on November 20th 2004 with the primary objective of observing Gamma-Ray Bursts (GRBs) and their afterglows in the optical, ultraviolet, and X-ray energy regimes. It has a total power of 1650 W, total mass of 1270 kg, and is in a circular orbit approximately 600 km above the earth at a $< 22^\circ$ inclination [39].

The first instrument is the Ultraviolet/Optical Telescope (UVOT), intended to capture the optical and ultraviolet photons emanating in the first minute after a burst of γ -rays, plus long term observations. The ultraviolet measurements in particular, of sky events aboard Swift are valuable, as they cannot be detected by ground-based instruments [39]. The detector is a Microchannel plate Charge-coupled detector (MCP Intensified CCD), with a 256 pixel by 256 pixel detection element, which operates by counting photons with wavelengths between 170 nm and 600 nm [40]. Its position on the spacecraft is shown in Figure 2.4.

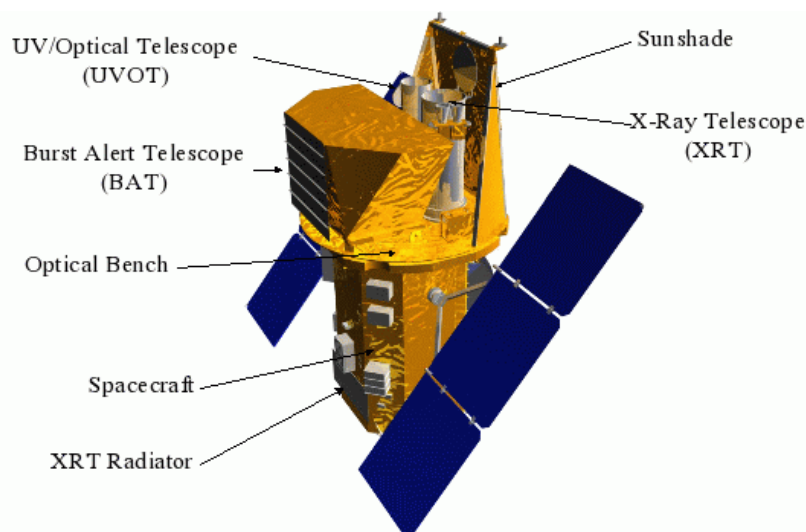


Figure 2.4: The Swift Gamma-Ray Observatory launched by NASA in 2004. The three instruments aboard provide γ -ray burst detection as well as optical, ultraviolet, and X-ray observational capabilities. Image from [41].

The second instrument is the X-Ray Telescope (XRT). It is a Wolter Telescope with 3.5 m focal length, a position accuracy of 3 arcseconds, and an effective area of approximately 125 cm^2 at 1.5 keV, which decreases with increasing photon energy. It is able to determine the positions of γ -ray burst afterglows within 100 s after being alerted of a burst by the Swift-BAT instrument, and X-ray spectroscopy allows the determination of other relevant properties of the burst [42].

The Burst Alert Telescope (BAT) is the instrument that initially detects the GRB, and triggers an automatic slew of the entire spacecraft to point in the direction of the event. The burst is realized by the BAT within the first 20 s of the start of the event, and the event direction is localized to within 4 arcminutes or less. The repointing occurs in less than 70 s, and optical, ultraviolet, and X-ray observations are made. The BAT has a detecting area of 0.524 m^2 and a sensitivity of nearly $10^{-8} \text{ erg/cm}^2/\text{s}$.

These instruments in unison provide a detectable energy range of 200 eV to 150 keV. Much of the data collected by Swift is available in [43], which has been analyzed when used in this work by [44].

2.2.5 Suzaku

Detectable energy range: 200 eV to 600 keV (X-ray)

The Suzaku spacecraft consists of three separate instruments, with a total weight of 1600 kg, known as the XRS, XIS, and HXD, allowing X-ray detection between 200 eV and 600 keV. It was launched on July 10 2005 from the Uchinoura Space Center, and its mission was declared complete after 10 years, on August 28 2015. Japan's fifth X-ray mission, it was jointly funded by the Japan Aerospace Exploration Agency, and NASA [45]. Its orbit around the earth was circular, at an altitude of 550 km, a period of approximately 96 minutes, and an inclination angle of 31deg maintained by the help of the Star Tracker Telescope (STT).

The X-Ray Spectrometer (XRS) is a high efficiency imaging spectrometer. The detector array is located behind a mirror assembly, and the device is cryogenically cooled. The energy range for detection is 300 eV to 12 keV and the XRS is considered the primary Suzaku instrument. There are 4 individual X-ray Imaging Spectrometers (XIS), which are composed of Charge-coupled device (CCD) cameras, and are co-aligned. The field of view of the XRS sits at the centre of the XIS alignment. The energy range for detection is 200 eV to 12 keV. The Hard X-Ray Detector (HXD) is a collimated system of detectors sensitive to the hard X-ray band, and does not produce images like the other two instruments aboard Suzaku. Instead it is responsible for rejecting particle background and detecting γ -ray bursts and other high energy phenomena in the range of 10 keV to 600 keV [46]. Note that X-rays with energies below 10 keV are considered soft X-rays. See Figure 2.5.

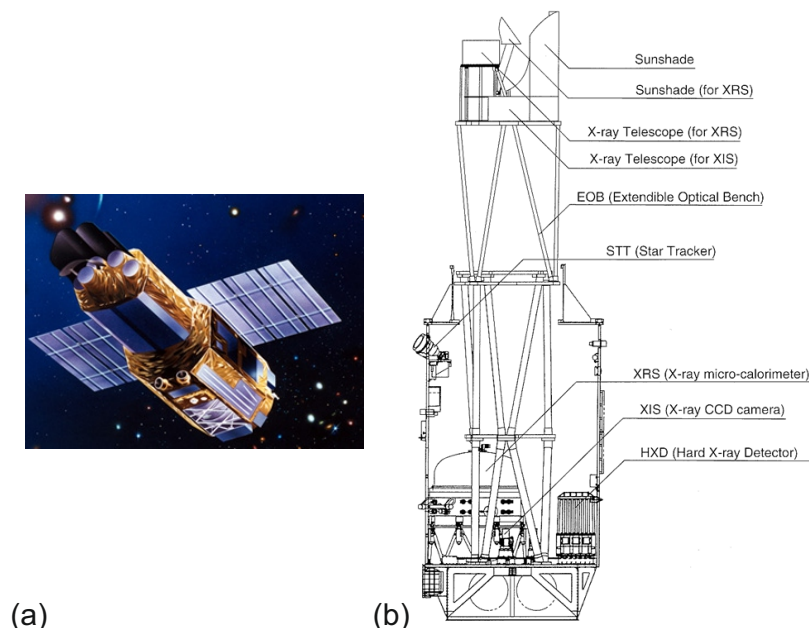


Figure 2.5: Suzaku. (a) Outer appearance of the Suzaku spacecraft. (b) Instrument positions on Suzaku, including the XRS, XIS, and HXD. Images modified from [47].

2.2.6 The Fermi Large Area Telescope

Detectable energy range: 20 MeV to 300 GeV

2.2.6.1 Mission and data

The Fermi γ -ray space telescope spacecraft was launched by NASA on June 11 2008 and has a detectable energy range of 20 MeV to 300 GeV. The primary instrument on board is the Large Area Telescope (LAT), built through collaboration by institutes in the USA, France, Italy, Sweden and Japan, with 7 specific mission goals [48]:

- (1) Collect data to allow rapid notification of γ -ray bursts and their transient energies
- (2) Conduct an all-sky survey in order to build a large listing of high energy emitting sources
- (3) Measure the spectra of objects between 20 MeV and 50 GeV
- (4) Localize point sources between 0.3 arcminutes and 2 arcminutes
- (5) Map extended sources such as nearby galaxies, molecular clouds, and supernova remnants

- (6) Measure the diffuse isotropic γ -ray background to TeV energies
- (7) Explore the discovery space for dark matter [48]. See Figure 2.6.



Figure 2.6: Artist's Conception of the Fermi γ -ray space telescope spacecraft in earth orbit. Image from [49].

Collection of data over the first two years of operation, from August 4 2008 to July 31 2010 between 100 MeV and 100 GeV has detected 1873 sources above 4 sigma, 11 of which are radio galaxies. These have been published in the LAT 2-year Point Source Catalog (2FGL) [50]. Besides the detected sources, all the original data collected by the Fermi-LAT as well as the software packages for its analysis have been made available for private download. This made the identification of an additional radio galaxy by [51] possible, and will also be the raw data used in this work. Since then, the catalog of four years of data collection between August 4 2008 and July 31 2012 has also been released in the LAT 4-year Point Source Catalog (3FGL) [52], although only the 2FGL data set will be used here. Table 2.1 lists the radio galaxies detected by the Fermi-LAT as of July 31 2010:

Table 2.1: Radio galaxies detected at γ -ray energies by the Fermi-LAT after two years of data collection, and their positions [50].

Source Name	R.A.	Dec
IC 310	49.169	41.322
NGC 1275	49.965	41.513
Fornax A	50.6	-37.292
OH -342	96.777	-35.479
3C 207.0	130.191	13.18
PKS 0943-76	145.712	-75.976
M 87	187.701	12.406
Centaurus A	201	-43.500
Centaurus B	201.418	-43.015
NGC 6251	206.663	-60.466
3C 380.0	247.355	82.614
Pictor A (by [51])	80.17	-45.61

Note that the radio lobes belonging to Centaurus A have been published in the catalog as a separate source. The energy flux for each source in the 2 year time range, between 100 MeV and 100 GeV in units of $\text{erg}/\text{cm}^2/\text{s}$, is also found in [50], which will be shown in each SED in the chapters to follow as an upper limit.

2.2.6.2 Detector design

The Large Area Telescope is a pair conversion telescope, with a total depth of 10.1 radiation lengths [48]. When an incident γ -ray enters the telescope, it encounters 16 planes of material (Conversion Foils) that are very high in

atomic number (Z). γ -rays cannot be reflected or refracted, but can interact with a medium and convert into an electron-positron pair. The high Z material helps in ensuring this.

Interleaved in these 16 layers are detectors sensitive to the position of charged particles, which measure the electron and positron paths in order to reconstruct the directions of the incident γ -rays. This is designated the Precision Converter Tracker [48]. Next the charged particles encounter the Calorimeter, which is composed of 96 CsI(Tl) crystals arranged in 8 horizontal layers, to a depth of 8.6 radiation lengths. The energy deposited by the electron and positron are read out by photodiodes attached to the ends of the crystal. The position of the deposited energy along the crystal is measured by comparing the difference in the scintillation light transmitted to both ends of the crystal, through read out with photodiodes [48]. Such a high mass calorimeter poses the problem of secondary particles. The initial γ -ray produces an electromagnetic shower of particles, any of which may Compton scatter in the layers of material, generating recoil electrons, and producing false signals. A third component to the LAT is the Anti-Coincidence Detector, designed to attack this issue and provide background rejection of charged particles through an extremely high detection efficiency requirement (99.97%) [53]. See Figure 2.7. The Data Acquisition System (not shown) processes events on board in order to reduce the number of events relayed from the spacecraft to the earth.

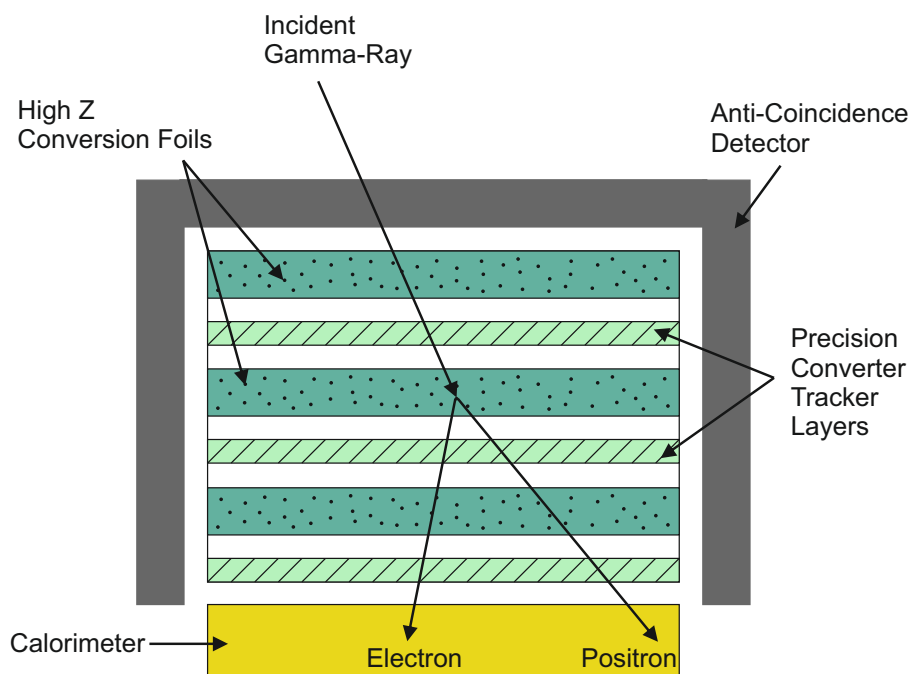


Figure 2.7: Sketch of cross-section of the Large Area Telescope on the Fermi spacecraft. Pair conversion occurs in the high Z Foils, and particle cascade pathways are tracked in the Precision Converter Tracker. Adjacent crystal layers in the Calorimeter are rotated by 90° . The Anti-Coincidence Detector is segmented into 89 tiles and has an average detection efficiency of 99.97% [53].

2.2.7 MAGIC

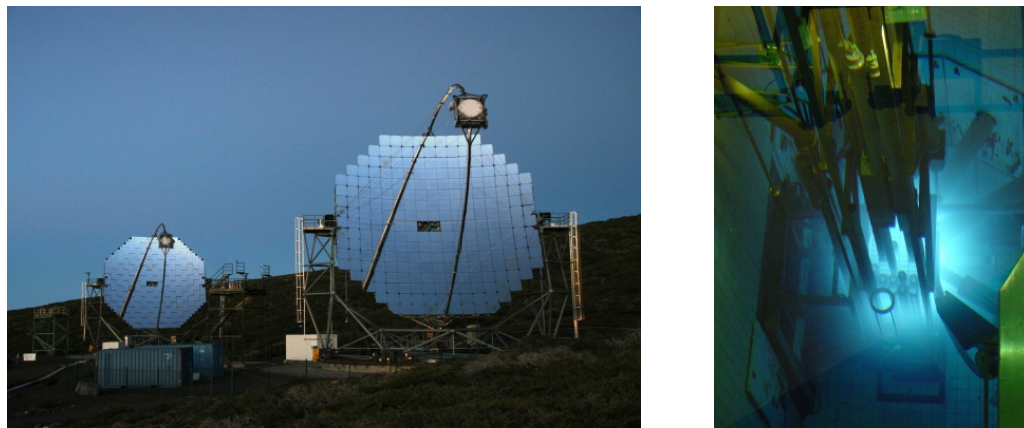
Detectable energy range: 50 GeV to 50 TeV

Located 2200 m above sea level on La Palma in the Canary Islands [54], the ground-based Major Atmospheric Gamma Imaging Cherenkov (MAGIC) telescope system is composed of two giant Imaging Atmospheric Cherenkov Telescopes (IACTs) which can measure the Cherenkov emission that results from γ -rays entering the earth's atmosphere and generating particle cascades. It can detect energies between 50 GeV and 50 TeV.

The telescope dishes are an array of mirrors, which reflect the gathered light onto a focal plane and camera. The field of view of the total stereoscopic system is 3.5° , with 547 trigger pixels and a signal readout sampling rate of 2.05 Giga samples per second. There is electrical noise in the signals, as well as changes in the night sky background, which may contribute error [55].

When a charged particle travels through an insulating or dielectric material, positive and negative charges are momentarily shifted from their rest

positions in its wake. Cherenkov light, mostly emitted in the optical and ultraviolet wavelengths, is produced when the charged particle moves at a velocity greater than the phase velocity of light in the medium, and the disturbed charges release energy in a coherent manner while returning to their equilibrium positions. This phenomenon is analogous to the sonic boom generated by aircraft traveling at velocities greater than that of sound. A beautiful characteristic blue glow of Cherenkov radiation can be observed in the water tank of a nuclear reactor. See Figure 2.8 [55], [56].



(a)

(b)

Figure 2.8: MAGIC telescopes and the phenomenon of Cherenkov emission. (a) The MAGIC telescopes are two Imaging Atmospheric Cherenkov Telescopes which detect the Cherenkov radiation produced by the interaction of γ -rays with the earth's atmosphere. (b) Cherenkov radiation is emitted when a charged particle travels through a dielectric medium at a speed greater than the speed of light in the medium, as seen in the water tank of the McMaster Nuclear Reactor. Images from [55] and [56].

The directions and energies of the incoming γ -rays are calculated through a stereoscopic reconstruction of simultaneous data from both telescopes, using the spatial distribution, angular distribution, and amount of detected Cherenkov radiation, which form elliptical images on the focal planes of the telescopes [55].

2.2.8 VERITAS

Detectable energy range: 50 GeV to 50 TeV

The Very Energetic Radiation Imaging Telescope Array System in Arizona, known as VERITAS, is also a Cherenkov detector with a detectable energy

range of 50 GeV to 50 TeV. It has high sensitivity in the range from 50 GeV to 50 TeV, and maximum sensitivity between 100 GeV and 10 TeV. It is composed of four telescopes, a 3.5° field of view [57], and 350 mirrors per reflecting dish [58].

VERITAS is positioned at an altitude 1280 m above sea level [54]. Although the detectable energy range is 50 GeV to 50 TeV, spectral energy distributions of the γ -rays being emitted from astrophysical objects can only be reconstructed between 100 GeV and 30 TeV. The accuracy of the location of the emitting object can be determined up to 50 arcseconds, and the system observes the sky for the equivalent of 3 to 4 days per calendar month (70 to 100 hours). See Figure 2.9.



Figure 2.9: VERITAS. The Very Energetic Radiation Imaging Telescope Array System at the Fred Lawrence Whipple Observatory in south Arizona, consisting of four detectors. Image modified from [59].

2.2.9 H.E.S.S.

Detectable energy range: 100 GeV to 50 TeV

The High Energy Stereoscopic System (H.E.S.S.) is composed of five Cherenkov telescopes located in Namibia at an altitude of 1800 m, with a total detectable energy range of 100 GeV to 50 TeV. It was originally a square array of four identical telescopes, 120 m per side, until a fifth, larger telescope was added to the centre which greatly improved the total energy threshold [60]. Named after Victor Hess, to whom the discovery of cosmic rays are credited, the observatory is a working collaboration between 12 countries.

The detector pixels consist of photomultiplier tubes and Winston cone light collectors, with 960 pixels existing on each of the corner detectors [61]. The largest detector has an area of 614 m² [60]. See Figure 2.10.



Figure 2.10: The H.E.S.S. telescope array. The four corner telescopes have a reflecting area of 108 m², and the centre telescope has a reflecting area of 614 m² [62]. Image modified from [63].

2.2.10 The joint campaign of Cherenkov detectors

Between December 2009 and June 2010, all three Cherenkov observatories conducted a joint monitoring campaign of the radio galaxy M 87. The partnership was initiated between MAGIC and VERITAS, until evidence of a very high energy flare was captured, prompting observation by H.E.S.S. also.

Data from M 87 was collected for an approximate total of 80 hours in the 6 month time period. Each observatory collected and analyzed data independently, before the results being combined in [54]. This time period has been selected for an independent analysis in this work, as described in §3.

Other detectors which focused their observation on M 87 after its flare, include Chandra and the VLBA [54].

2.2.11 Archival data

Data from older telescopes, deemed 'historical' or 'archival' data, is well documented in the NASA/IPAC Extragalactic Database [64], and is used to supplement energy ranges in the SED for which little or no current data is available.

2.3 Collection of simultaneous multiwavelength data

2.3.1 Simultaneous data

Multiwavelength spectral energy distributions are the first step in attaining a coherent and complete understanding of the processes occurring in the black hole-driven active galactic nucleus. Due to possible flaring episodes, it is essential to plot these distributions using simultaneous multiwavelength data from various detectors across the electromagnetic spectrum. Generally, very high energy Cherenkov data from MAGIC, VERITAS and H.E.S.S. between 50 GeV and 50 TeV is the limiting resource as these detector systems are fewer, and time allocation highly sought after. In some cases in the chapters that follow, the Cherenkov observations are not simultaneous to the other observations, but are still included as they are essential in completing the upper energy region of the SED.

2.3.2 Sample selection

γ -ray emitting radio galaxies or misaligned active galactic nuclei, are selected for study in this work as they may present weaker luminosities than blazars due to doppler boosting effects and therefore might not be as numerously detected [5], making them a more interesting and elusive population. Of the 12 radio galaxies detected in the first 2 years of survey data by the Fermi-LAT as listed in Table 2.1, it was determined that only 4 of these have also been observed by the highest energy-reaching Cherenkov telescope systems (Table 2.2):

Table 2.2: Radio galaxies detected at γ -ray energies by the Fermi-LAT, and in very high energy γ -rays by atmospheric Cherenkov detector systems.

Source Name	VHE γ -ray Detector	Time Range
M 87	MAGIC, VERITAS, H.E.S.S.	Dec 2009 to June 2010
NGC 1275	MAGIC, VERITAS	Aug 2010 to Feb 2011, Jan 15 2009 to Feb 26 2009
IC 310	MAGIC	Oct 2009 to Feb 2010
Centaurus A	H.E.S.S.	2004 to 2008

Pictor A will be included in the sample as its recent discovery has made it a source of interest in general, and a potential target for VHE γ -ray observation. Therefore the sample of 5 γ -ray emitting radio galaxies that will be studied in the chapters to follow are M 87, NGC 1275, IC 310, Pictor A and Centaurus A.

2.4 Analysis of raw Fermi-LAT data

The data collected by the Fermi-LAT is available to the public from the Fermi Science Support Center [65], in the form of FITS files and a BROWSE table, along with documentation and analysis tools (version ScienceTools-v9r23p1-fssc-20111006). The instrument response function (IRF) is P7SOURCE_V6 (for more information, see [50] and [65]). Input of a time range, energy range and search centre produces a specialized download file. The tools used in this analysis are summarized in Table 2.3:

Table 2.3: Selection of Fermi-LAT data analysis tools from [66].

Fermi Tool	Function
gtselect	Performs cuts on the events file
gtmktime	Creates good time intervals using spacecraft data
gtbin	Bins events in time or energy
gtltcube	Calculates a livetime cube; integrated livetime as a function of position and angle
gtexpcube2	Generates exposure map for different energies from a livetime cube
gtltsum	Sums livetime cubes
gtdiffrsp	Calculates integral over solid angle of source convolved with IRF
gtexpmap	Calculates exposure map for unbinned likelihood analysis
gtfindsrc	Optimizes point source location using likelihood test statistic
gtlike	Performs binned or unbinned likelihood analysis
gtsrcmaps	Convolve source model components with IRF
gttsmap	Calculates test statistic map for source localization and detection
farith	Generates residual maps by subtracting model map from event data

Mission Elapsed Time (MET) has been adopted by Fermi as the number of seconds that have passed since 0 hours, 0 minutes, and 0 seconds on the date of January 1 2001 which corresponds to the Modified Julian Date (MJD) 51910. good time intervals (GTIs) are the time ranges when the collected data can be considered valid, and devoid of any significant contamination. Pass 7 data is grouped into three classes: event class transient (1), source

(2), and diffuse (3). Event class 2 photons are used throughout the analysis. Error is known to increase below 300 MeV due to a high excess of photons, and the difficulty in ascertaining which photons have a high likelihood of originating from the source of interest. Above 100 GeV, there are low statistics for events.

Raw data for the sample of radio galaxies is analyzed in the following way. After the Fermi-LAT data is procured in a circular region, a box-shaped region with dimensions 16° by 16° showing the counts map, contained by the circle, is constructed in such a way that it contains the source of interest and major γ -ray emitters in the vicinity. Thus the source of interest is not always in the exact centre of the region, and it need not be. A counts map represents the relative numbers of events throughout a region using colour-coding, with black being zero events and the number of events increasing from blue, to red, to yellow, to white (each counts map is accompanied by a colour legend). The region has 80 pixels per side with an image scale of 0.2 degrees/pixel, and a zenith angle cut of 100° is made to exclude background radiation originating from the earth.

The continuum of events is processed through a binned likelihood analysis, which uses the known distribution of sources in the γ -ray sky to calculate the probability of capturing events by the LAT. Background model files representing the galactic γ -ray background (gal_2yearp7v6_0), and the isotropic γ -ray background (iso_p7v6source), are input along with the prominent sources in the region [67]. The likelihood statistic optimizes the fit parameters which allow convergence upon either data points or upper limits, most often in power law form.

A power law spectrum is defined as

$$\frac{dN}{dE} = N_o \left(\frac{E}{E_o} \right)^\Gamma \quad (2.2)$$

where Γ is the photon spectral index of the fit, E_o is the scale, and N_o is a prefactor.

A log parabola spectrum is defined as

$$\frac{dN}{dE} = N_o \left(\frac{E}{E_b} \right)^{-(\alpha + \beta \log(E/E_b))} \quad (2.3)$$

[67], where N_o is a prefactor, E_b is a fixed scale parameter close to the minima of the energy range of the spectrum [68], and α and β are spectral indices.

In this work, a test statistic (TS) value of 16.0, corresponding to approximately 4 sigma, will be applied as a constraint for detection, and between 3 and 4 sigma will be taken as an upper limit. The power law equation describes the spectral index and differential flux; an integral flux will also be calculated, which will allow quantitative comparison with other Fermi-LAT results. The Fermi-LAT analysis technique is consistent for each of M 87, NGC 1275, Pictor A, and Centaurus A, and the Fermi-LAT SEDs will also be fitted. The analysis and fitting will also be followed through for IC 310, with details explained in §4. EBL absorption, or the interaction of γ -rays emitted from sources in each region of interest (ROI) with the γ -ray background, to produce electron-positron pairs, will not be taken into account. The shown Fermi-LAT SEDs will be the observed SEDs.

2.5 Synchrotron self-Compton multiwavelength modeling

The spectral energy distributions of the nonthermal emission of many AGN are characterized by two peaks, the first being in the radio to X-ray range and the second in the X-ray to γ -ray range [69]. This results in what is known as a double-hump signature. One approach in explaining this emission is with a synchrotron self-Compton model. In this scenario, the double-hump is attributed to (1) synchrotron radiation being emitted from relativistic electrons and positrons accelerated by the magnetic field of the AGN jet, and (2) the self-Compton emission resulting from the further upscattering of these synchrotron photons, from the original source population of electrons and positrons [70]. Current models employ variations on the number and type of lepton emission zones traveling through the jet, as well as whether hadrons are considered in addition to electrons and positrons.

2.5.1 The one-zone SSC model

Single-zone synchrotron self-Compton models have been reasonably successful in explaining the multiwavelength emission from BL Lac objects, including γ -ray SEDs. FRI objects which are interpreted as being misaligned BL Lac objects, can usually be explained through a single-zone SSC scenario [71], [72], [11]. This type of model has been able to fit emission from the Fermi-LAT detected FRI galaxies Perseus A [73] and M 87 [74]. However one-zone SSC models are known for having difficulty explaining higher energy emission such as in the TeV range, and a new model is needed.

2.5.2 The two-zone SSC model by Weidinger et al.

The novel synchrotron self-Compton fitting model developed at the Lehrstuhl für Astronomie, Universität Würzburg, by Matthias Weidinger et al. as described in [75], [76], [77], [78], employs the benefit of two radiation zones, deemed the Acceleration Zone and the Radiation Zone, which travel down the jet in a nested arrangement [78]. Leptons are accelerated by both Fermi I and Fermi II acceleration mechanisms, or Shock and Stochastic processes respectively, in the acceleration zone, where leptons also suffer energetic losses due to synchrotron and inverse-Compton processes [78]. Leptons are then modeled to enter the radiation zone where no further acceleration occurs, but particles again undergo synchrotron and inverse-Compton losses. Each zone is a spherical, homogenous sphere or ‘blob’ with the radiation zone approximately one order of magnitude larger in size than the acceleration zone [75]. See the schematic in Figure 2.11 [78]. The time-dependent kinematic equations are solved in the blob-frame, forward in time, while receiving a continuous monoenergetic injection of electrons, where the acceleration zone kinetic equation is solved first, leading to the radiation zone kinetic equation [75]. Transforming from the reference frame of the blob to the reference frame of the observer, the spectral energy distribution is self-consistently generated [75], [76], [77], [78].

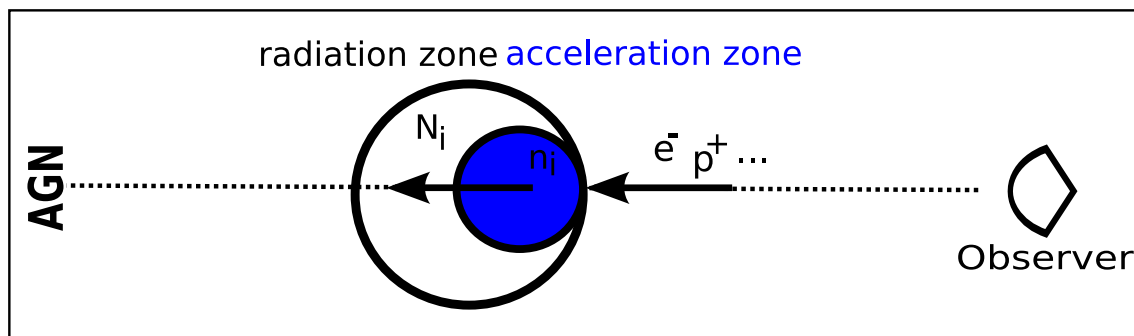


Figure 2.11: The nested arrangement and radiation and acceleration zones of Weidinger and Spanier [78].

The model parameters listed in Table 2.4 manipulate the resulting SED in several ways. B , R_{acc} , R_{rad} and t_{acc} affect the position and shape of the synchrotron amplitude [75], while the ratio of shock to stochastic acceleration ‘ a ’ affects the general curvature of the SED and the minimum, or dip, between the synchrotron and inverse-Compton peaks. t_{esc} corresponds partially to the rise in a flaring blazar lightcurve [75] and the ratio of t_{acc} and t_{esc} determine the power law spectral index of the particle distribution.

Notable merits of this model are its ability to explain the dynamics of an object over 20 orders of magnitude, well explaining also the TeV energy regime [75]. The fit parameters are self-consistently arrived upon, and the complete time-dependency of the acceleration and radiation mechanisms implies that variability can be accurately considered. As well, conservation of both total energy and matter (particles) are satisfied in each radiation zone independently, and both zones together [75]. Previous one-zone models assumed a generic injected distribution of electrons of power law form and exponential cutoff; however here, the distribution *evolves* during the simulation, from a monoenergetic electron number density. Thus, in addition to employing two zones, being fully self-consistent and time-dependent, the two-zone model provides the additional advantage of explaining such previously ‘ad-hoc,’ or assumed, distributions [75], [76], [77], [78], while circumventing the pitfalls associated with older models.

The model has been further developed into a time-dependent, self-consistent, two-zone Hybrid consideration, which has hadrons as well as leptons being accelerated by Fermi I and Fermi II processes, before incurring radiative losses due to synchrotron and inverse-Compton mechanisms [77], [78]. It is the first model to resolve the non-linear processes due to photo-hadronic

Table 2.4: Two-zone SSC parameter descriptions by Weidinger et al. [75], [76], [77], [78].

Parameter	Description	Units
B	Magnetic field in the jet	G
R_{acc}	Radius of acceleration sphere	cm
R_{rad}	Radius of radiation sphere	cm
t_{acc}	Acceleration timescale	s
t_{esc}	Timescale for electrons escaping acceleration sphere	s
Γ	Lorentz factor	-
δ	Doppler factor	-
K	Injected electron number density	cm^{-3}
a	Ratio of Fermi I to Fermi II acceleration	-
K_p	Injected proton number density (Hybrid)	cm^{-3}
Γ_p	Proton Lorentz factor (Hybrid)	-

interactions and free pair production time-dependently. Neglecting the presence of hadrons in this hybrid scenario would result in the purely leptonic case [77], [78]. For additional details regarding the radiation model code, see [75], [76], [77], [78].

2.5.3 Other models to one and two-zone SSC

Alternative mechanisms to SSC in general, are the Compton Scattered Accretion Disk, or Dust Torus Radiation [71].

The unification models for blazars suggest that FRII galaxies are flat spectrum radio quasars, with the jet being viewed away from our line-of-sight. Similarly, FRI objects are BL Lac objects with the jet being viewed away from our line-of-sight. Therefore we should observe nonthermal radiation from radio galaxy cores that is *de-beamed* in comparison to blazars. Paradoxically however, FRI cores actually appear brighter than what is expected from simply de-beamed BL Lac emission [71].

The beaming angle Θ_b is related to the bulk Lorentz factor by

$$\Theta_b \cong \frac{1}{\Gamma_j} \quad (2.4)$$

therefore a brighter core implies the core emission is from a *slower* region in the radio galaxy, or FRI than in a BL Lac.

This can be explained in two ways [71]:

(1) The Spine Sheath Model. The jet is made of a fast spine producing on-axis blazar emission surrounded by a slow outer sheath producing the off-axis emission seen in radio galaxy cores [79].

(2) The Decelerating Jet Model. In this scenario, on-axis blazar emission is produced by a fast flow closer to the black hole and the off-axis γ -rays seen in radio galaxies are produced by a slow flow farther out along the jet [80], resulting in a decelerating flow.

2.6 Dark matter annihilation modeling

The neutralino is a Majorana particle, meaning that it is its own antiparticle. Following from the particle cascade described in §1.5, the total differential flux generated by dark matter annihilation is expected to consist of a pion decay component and an inverse-Compton component, and the signature invariable with respect to time.

$$\left(\frac{d\Phi}{dE}\right)_{Total} = \left(\frac{d\Phi}{dE}\right)_{\pi^0} + \left(\frac{d\Phi}{dE}\right)_{IC} \quad (2.5)$$

2.6.1 Prompt pion emission

The differential γ -ray flux, i.e. prompt pion emission, which arises from the annihilation of a neutralino with its anti-particle ($\pi^0 \rightarrow \gamma + \gamma$), and subsequent hadronization and decay of the annihilation products, is given by [70]:

$$\left(\frac{d\Phi}{dE}\right)_{\pi^0} = \frac{1}{4\pi} \frac{f(\sigma_A \nu)}{2m_\chi^2} \frac{dN_\gamma}{dE} \frac{1}{D^2} \int_{Source} dV \rho_{NFW}^2(r) \quad (2.6)$$

[70], where the source has volume V , is placed at a distance D , has a boost factor f which quantifies clumping enhancement in the dark matter halo, and m_χ is the mass of the dark matter particle. The thermally averaged annihilation cross-section is denoted by $\langle\sigma_A v\rangle$, and the Navarro-Frenk-White profile for the dark matter density $\rho_{NFW}(r)$ is assumed in this scenario [70], [81].

Neutral pion decay produces the continuous γ -ray rest frame energy distribution per annihilating particle [21]

$$\frac{dN_\gamma}{dE} = \frac{0.42}{m_\chi} \frac{e^{-8x}}{x^{1.5} + 0.00014} \quad (2.7)$$

where $x = \frac{E}{m_\chi}$ and E is the rest frame energy of a γ -ray photon where $E_{max} = m_\chi$ [21]. The study by [21] scanned a large SUSY parameter space with $m_{\chi min} = 70$ GeV and $m_{\chi max} =$ several TeV, resulting in approximately 10^{-15} photons/cm²/s/sr/GeV at 86 GeV.

2.6.2 Inverse-Compton emission

The inverse-Compton upscattering of cosmic microwave background photons ($e^{+-} + \gamma \rightarrow e^{+-} + \gamma$), by highly energetic charged electrons and positrons in the neutralino decay chain is given by

$$\left(\frac{d\Phi}{dE}\right)_{IC} = \frac{1}{E} \frac{f \langle\sigma_A v\rangle}{4\pi m_\chi^2} \frac{1}{D^2} \int_{Source} dV \rho_{NFW}^2(r) \int_{m_e}^{m_\chi} dE' \frac{P(E, E')}{b(E')} \int_{E'}^{m_\chi} d\tilde{E} \frac{dN_e}{d\tilde{E}} \quad (2.8)$$

where the total rate of electron/positron energy loss is given by $b(E')$, photons having energy E absorb the differential power $P(E, E')$ from leptons having energy E' , and the secondary lepton spectrum is $dN_e/d\tilde{E}$ [82].

DarkSUSY is an advanced numerical package written specifically for dark matter calculations [83], and used to generate the charged and neutral pion emission spectra in this work.

2.7 Summary

The multiwavelength instrumentation, sample selection, and technical methods have been explained here, with a focus on simultaneity and consistency in the Fermi-LAT, SSC, and dark matter analyses. In what is to follow, each member of the selected sample of γ -ray emitting radio galaxies will be investigated in a dedicated chapter. General characteristics of the galaxy will be introduced, followed by the collection of simultaneous multiwavelength data. This will be followed by analysis of Fermi-LAT data in an ROI containing the source of interest, in order to calculate the integral flux, differential flux, spectral index, and plotted SED from either a power law or log parabola fit. These results will be combined with the rest of the multiwavelength data and analyzed with the SSC modeling approach. Where possible, the dark matter annihilation model will be applied, taking prompt pion and inverse-Compton emission into consideration.

Chapter 3

M 87

3.1 Introduction

A supergiant elliptical radio galaxy ($z = 0.004$) located in the Virgo cluster, Messier 87 has a γ -ray emitting radio jet and supermassive black hole at its centre. It is one of the best-researched radio galaxies, as it is also one of the closest to earth located ~ 16 Mpc away, and has been confirmed as a VHE γ -ray emitter above 100 GeV [54]. The black hole mass of M 87 is between $3 \times 10^9 M_{\odot}$ and $6 \times 10^9 M_{\odot}$ [74]. Variability is demonstrated in the optical, X-ray and γ -ray bands [74], with three VHE flares documented in 2005, 2008, and 2010. All three instances were similar in their short timescale on the order of days [54]. See Figure 3.1 for a Hubble telescope optical image of the M 87 jet. In this chapter, the collection of observed data for M 87 from detectors across all energy bands will be described, and the Fermi-LAT analysis time range determined. The Fermi-LAT data will be analyzed in the Fermi Tools environment, to determine the γ -ray SED. This will be followed by multiwavelength SSC modeling. Dark matter analysis of a previously constructed M 87 SED shall conclude the chapter.



Figure 3.1: Optical image of M 87 taken from the Hubble telescope. Image modified from [84]. Credit: NASA, ESA, and the Hubble Heritage Team (STScI/AURA).

3.2 Collection of simultaneous multiwavelength data

Searches for multiwavelength M 87 data revealed simultaneous Swift-XRT, Swift-UVOT and Swift-BAT data in the time range from January 1 2010 to April 12 2010 [43], and VHE joint monitoring campaign data from MAGIC, VERITAS and H.E.S.S. from December 2009 to June 2010, as mentioned in §2.2.10 [54]. Although [54] illustrated only the light curve and not the SED of M 87, the simultaneous time range is nevertheless selected for Fermi-LAT analysis in this work, with localization at R.A = 187.71 and Dec = 12.39. Figure 3.2 shows the collection of multiwavelength data forming a double-hump structure which is typical for blazars. Figure 3.3 illustrates the overlapping time ranges of the simultaneous data.

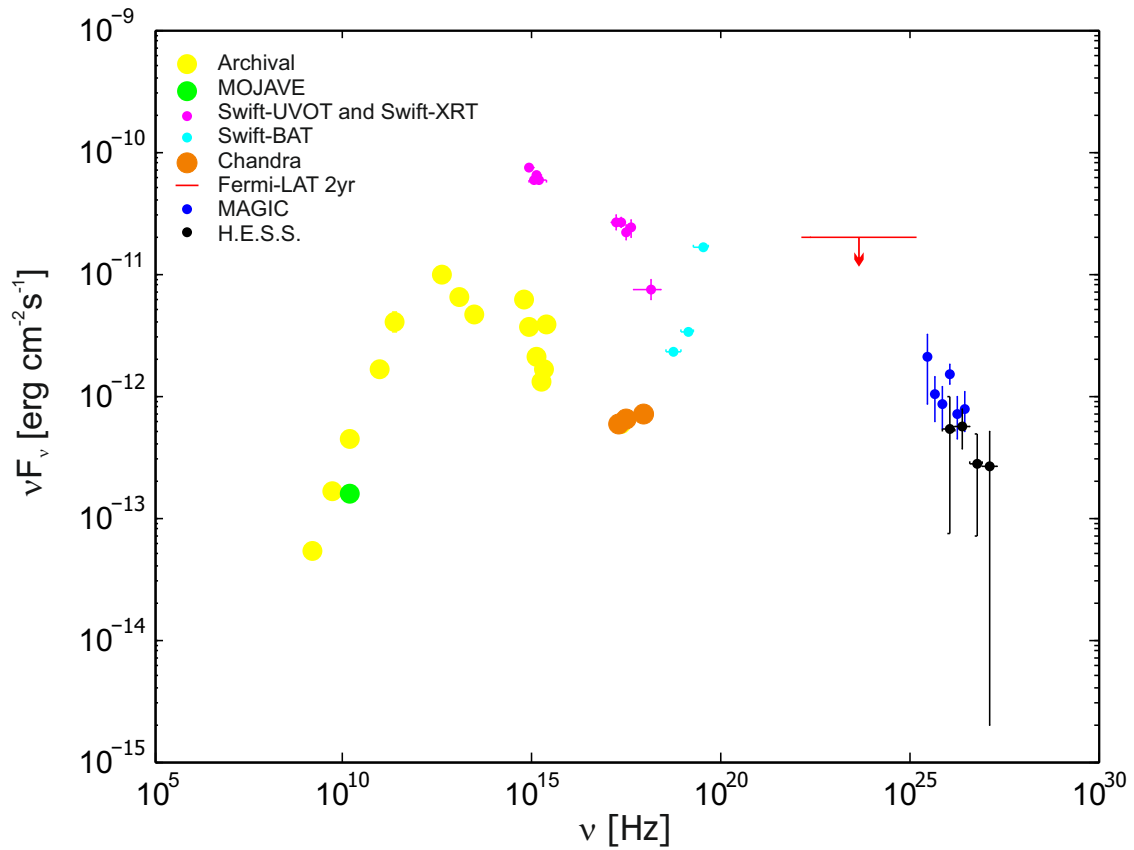


Figure 3.2: Collection of multiwavelength data for *M 87*. Simultaneous data: Swift-UVOT and Swift-XRT from January 1 2010 to April 12 2010 in magenta. Non-simultaneous data: NED archival data as in [74] in yellow, MOJAVE VLBA 15 GHz measurement of core from January 7 2009 in green, Chandra measurements of the core from January 7 2009 in blue, Swift-BAT 3 sigma upper limits from March 2005 to January 2009 in three hard X-ray bands as in [74] shown in cyan. Fermi-LAT 2 year upper limit between 100 MeV and 100 GeV is shown by the red line, MAGIC detection from March 2005 to June 2007 in blue, H.E.S.S. low state data from 2004 in black.

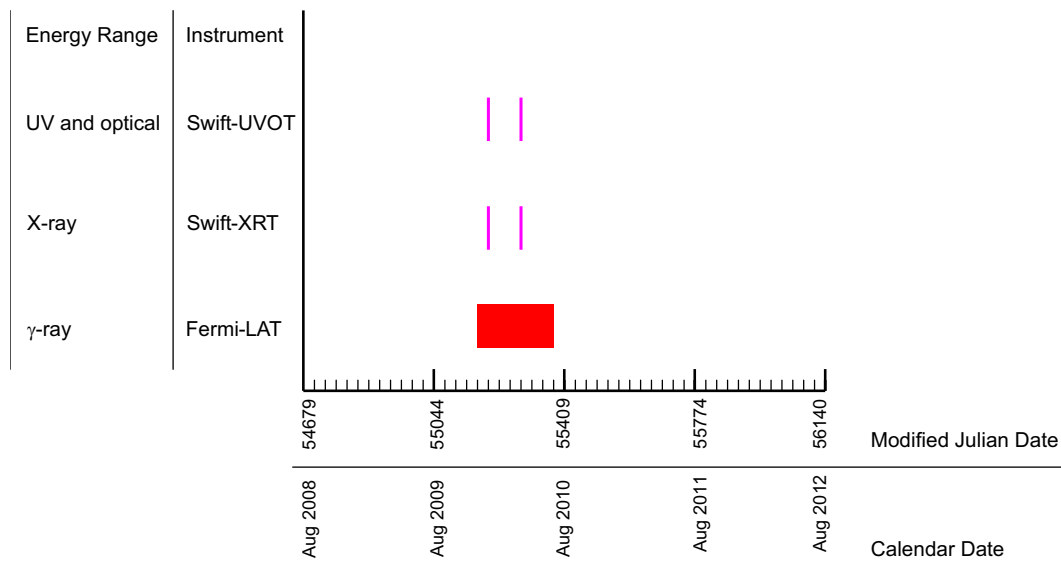


Figure 3.3: Schematic of simultaneous observation times for M 87 from different instruments in various energy regimes.

3.3 Results of Fermi Large Area Telescope analysis

Event class 2 photons are analyzed around a 20° search region centred on R.A. = 186.54512, Dec = 15.942496, containing significant bright sources. The selected time period is MET 281318400 to 299635199 (December 2009 to June 2010). The Fermi Tools `gtselect`, `gtmktime` and `gtbin` are applied between 300 MeV and 100 GeV within the Fermi Tools environment to construct an 80 pixel by 80 pixel, 0.2 degree/pixel counts map and counts cube, from good time intervals. With the additional consideration of the galactic background and isotropic background model files, a total region model is derived. Through application of `gtltcube`, `gtexpcube2` and `gtsrcmaps`, the 10 most prominent sources in the region are identified. See Figure 3.4 and Table 3.1.

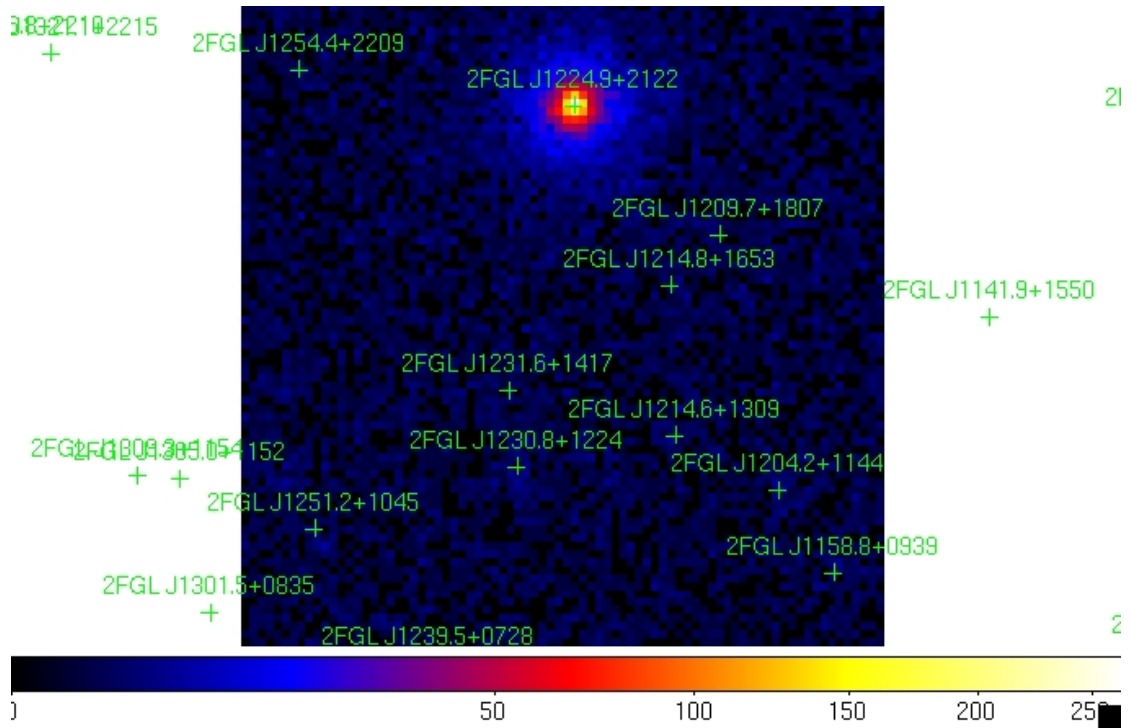


Figure 3.4: Fermi-LAT counts map centred at R.A. = 186.55, Dec = 15.94, with M 87 located at R.A. = 187.71, Dec = 12.39. Colour scheme indicates the number of counts detected by the telescope during the selected time range, at each x-y coordinate, where the map is composed of 80 pixels in each direction.

Table 3.1: Brightest sources and their test statistic values in the 16° by 16° region of interest selected for radio galaxy M 87, corresponding to Figure 3.4.

Common Name	Catalog Designation	TS
TXS 1252+224	2FGLJ1254.4+2209	19.7
1RXS J125117.4+103914	2FGLJ1251.2+1045	18.4
4C +21.35	2FGLJ1224.9+2122	23347.7
GB6 J1231+1421	2FGLJ1231.6+1417	14.7
M 87	2FGLJ1230.8+1224	57.4
MG1 J120953+1809	2FGLJ1209.7+1807	8.8
TXS 1212+171	2FGLJ1214.8+1653	8.9
4C +13.46	2FGLJ1214.6+1309	15.7
1RXS J120413.0+114549	2FGLJ1204.2+1144	42.2
GB6 J1158+0937	2FGLJ1158.8+0939	35.6

Freeing the normalization and index parameters for these sources, and fixing the sources that were located outside the region of interest, a likelihood analysis was executed. The NEWMINUIT optimizer converged on fits for each source (see details in §A.1.1 and Figures A.1 to A.4). Localization of M 87 at R.A. = 187.71, Dec = 12.39, produced an integral flux of $7.95 \times 10^{-9} \pm 1.64 \times 10^{-9}$ ph/cm²/s (§A.2.1) and power law SED as depicted in Figure 3.5:

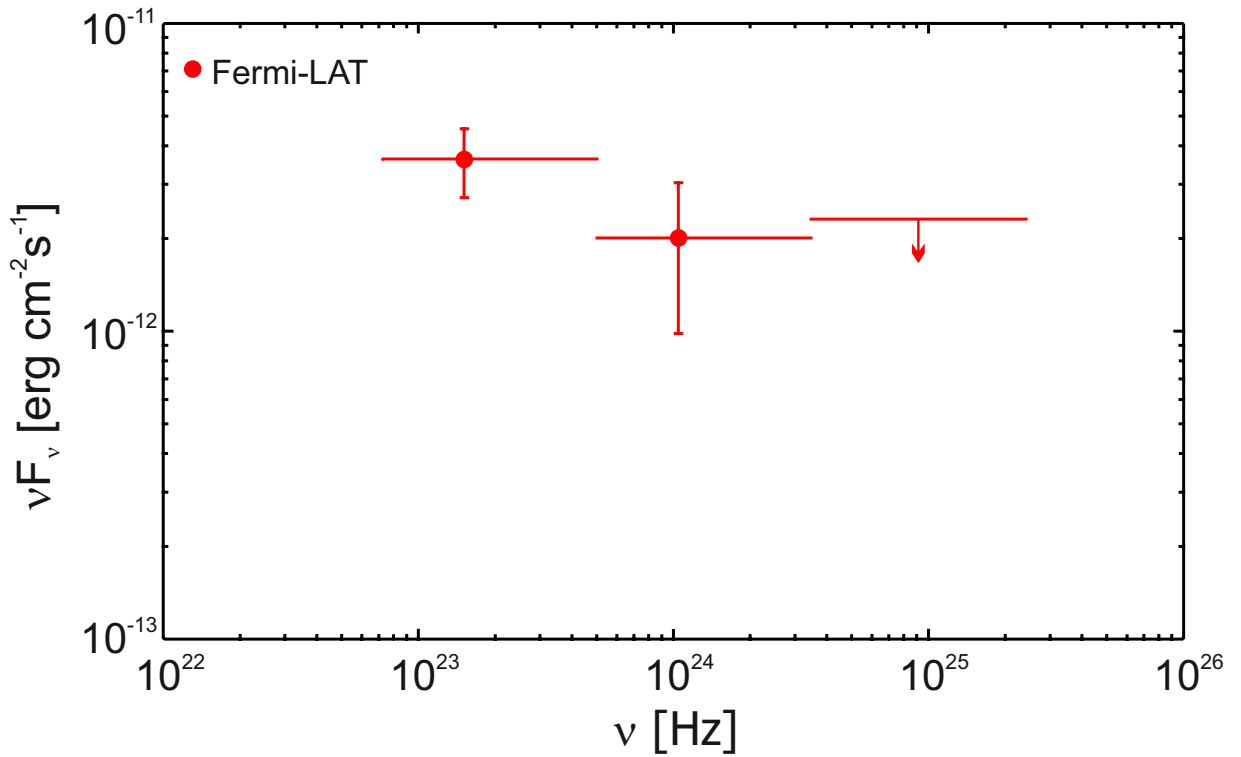


Figure 3.5: Power law Fermi-LAT spectral energy distribution of M 87.

The fit of M 87 as shown in Figure 3.5 has a high TS value of 57.4, with a log likelihood equal to 25214.6. The farith Fermi Tool calculates a data-model subtraction at every point, and in this case yielded nearly zero at every point, indicating a good fit to the data. Assuming a TS limit of 16.0, corresponding to 4 sigma, the Fermi-LAT γ -ray SED over three bins generated two points and one upper limit.

3.3.1 Comparison of results

The joint campaign of Cherenkov detectors [54] also conducted a Fermi-LAT analysis over the time range of August 4 2008 to August 4 2010 (MET 239557417 to 302630530) over the slightly wider energy range of 100 MeV to 300 GeV. This resulted in an integral flux equal to $2.66 \times 10^{-8} \pm 0.36 \times 10^{-8}$ ph/cm²/s, and a photon index of 2.16 ± 0.07 . Using this longer energy range as the limits for integration for the analysis in this work, yields a comparable integral flux of 3.25×10^{-8} ph/cm²/s.

3.4 Results of multiwavelength analysis

The results of the Fermi-LAT analysis of M 87 as depicted in Figure 3.5 are incorporated into the total SED from Figure 3.2. M 87 is fit with the aforementioned SSC model in Figure 3.6:

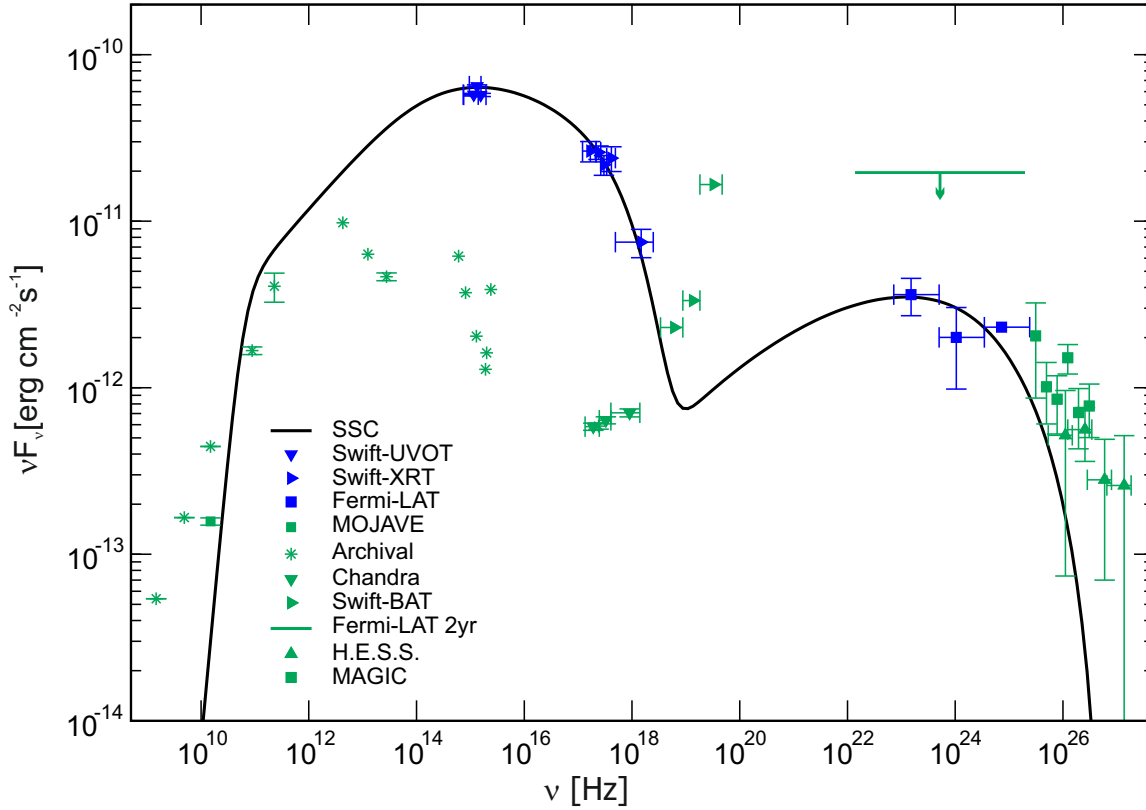


Figure 3.6: SSC fit of M 87 based on Swift-XRT data, Swift-UVOT data, and Fermi-LAT analysis in this work. Blue data points are considered in the fitting, and green data points and one upper limit are used for reference.

The injected electron number density is $K = 1.9 \times 10^6 \text{ cm}^{-3}$, Lorentz factor is $\Gamma = 10$, and magnetic field in the jet is $B = 0.24 \text{ G}$. The radiation and acceleration zone radii are $R_{rad} = 6.0 \times 10^{15} \text{ cm}$ and $R_{acc} = 1.0 \times 10^{14} \text{ cm}$, with an acceleration to escape timescale ratio of $\frac{t_{acc}}{t_{esc}} = 1.43$, and a Fermi I to Fermi II acceleration ratio of $a = 20$. The doppler factor is $\delta = 14.5$.

Abdo et al. 2009 [74] has fit non-simultaneous Fermi-LAT and H.E.S.S. data with a one-zone SSC model, with bulk Lorentz factor $\Gamma = 2.3$ and doppler factor $\delta = 3.9$.

Acquiring simultaneous very high energy γ -ray observations in the future, from either MAGIC, VERITAS, or H.E.S.S., would be of benefit in completing the multiwavelength SED of M87.

3.5 Results of dark matter analysis

Before the above analysis of simultaneous multiwavelength observations of M 87, non-simultaneous multiwavelength observations were also explored. Non-simultaneous, quiescent-state data for M 87 from Chandra, Fermi-LAT, MAGIC and H.E.S.S. [70], with significant flaring excluded, also produced a reasonable fit using an older one-zone version of the SSC code [85], with the injected electron number density $K = 1.0 \times 10^6 \text{ cm}^{-3}$, Lorentz factor $\Gamma = 10$, and magnetic field in the jet $B = 3.0 \text{ G}$. The single spherical zone radius was $R = 3.5 \times 10^{13} \text{ cm}$ with doppler factor $\delta = 3.9$. See Figure 3.7.

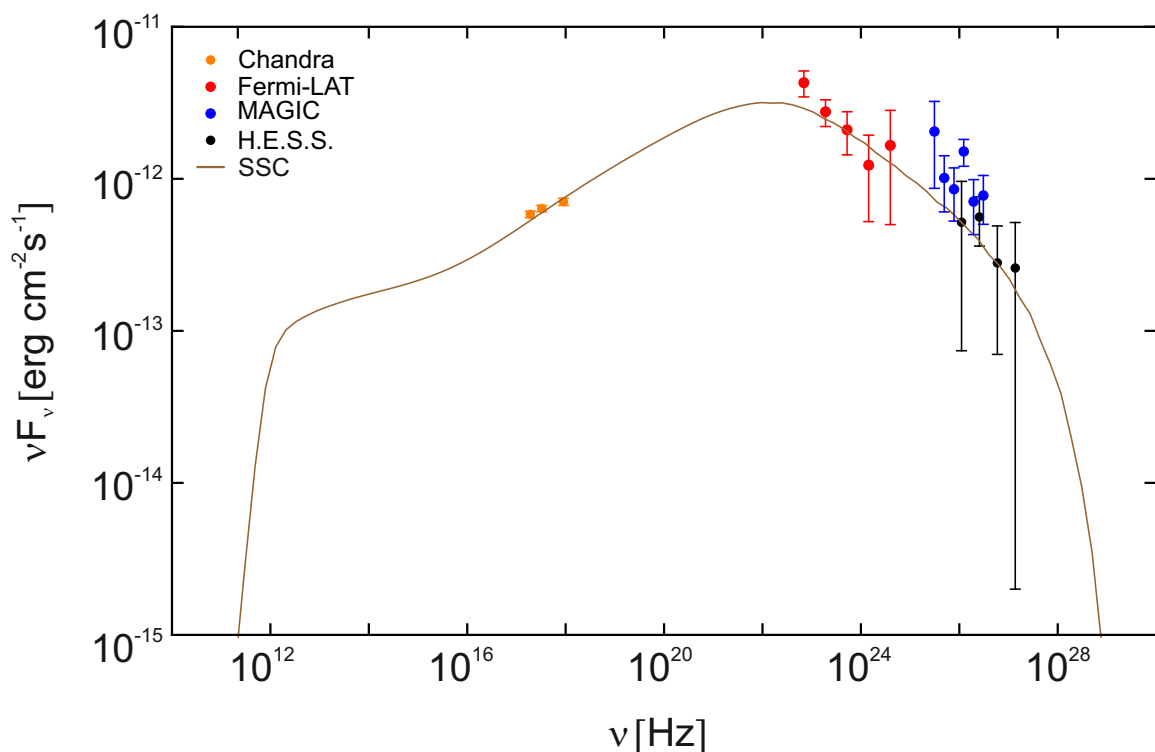


Figure 3.7: Single-zone SSC estimate of the long-term quiescent-state emission of M 87. The multiwavelength SED is collected from the Chandra observatory, the Fermi-LAT, and the MAGIC and H.E.S.S. Cherenkov detectors. A modified image has been published in Saxena et al. [70].

There was a notable excess in the VHE γ -ray regime detected by the MAGIC telescope, which was not explained by the SSC model. Applying the dark matter model described in §2.6 with a thermally averaged annihilation cross section $\langle \sigma_A v \rangle = 3 \times 10^{-24} \text{ cm}^3/\text{s}$, the DarkSUSY code introduced in §2.6.2 is used to generate the charged and neutral pion emission spectra, with a total of 10^6 neutralinos. The first peak is the decay of neutral pions into γ -rays, and the second inverse-Compton peak originates from the decay cascade of

charged pions resulting in electrons and positrons which upscatter cosmic microwave background photons. Combining the two models allows fitting of the entire spectrum, and explains the excess in γ -ray frequencies. See Figure 3.8.

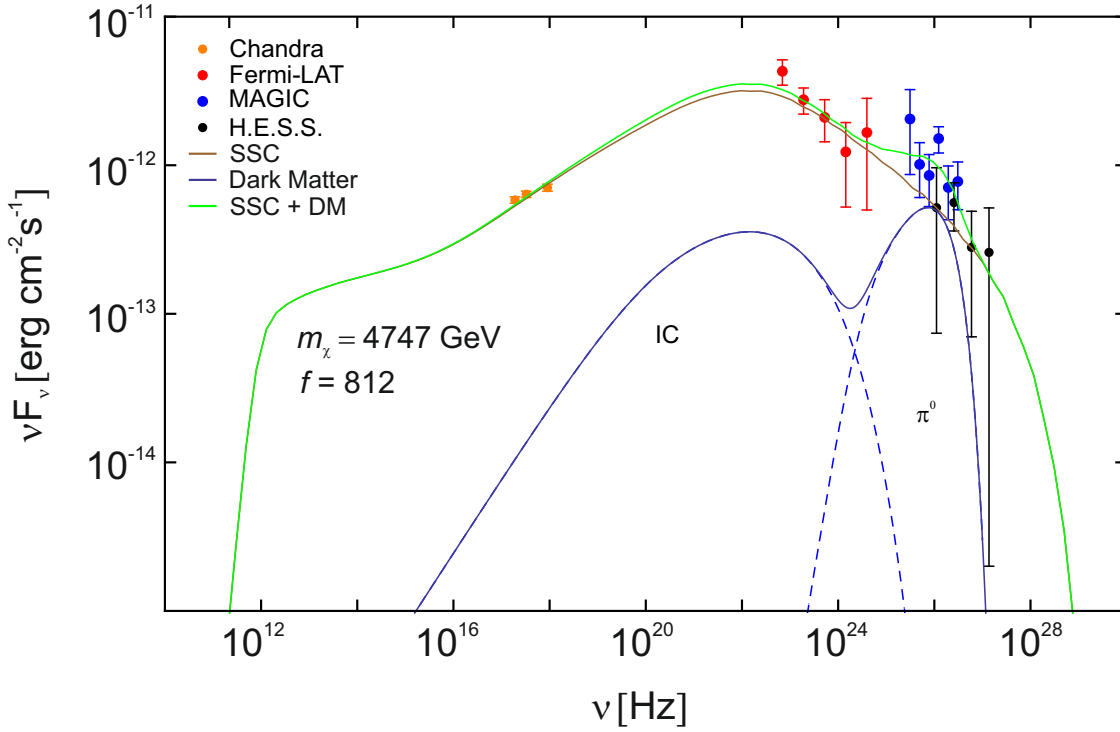


Figure 3.8: Spectral energy distribution of M 87. The brown line indicates the SSC fit, the blue lines indicate the dark matter contributions, and the green line denotes the total fit which takes into account both SSC modeling and dark matter modeling. A modified image has been published in Saxena et al. [70].

The best fitting model combining SSC fitting to the nonthermal jet emission as well as dark matter WIMP annihilation, is determined using a Chi-squared (χ^2) test, where values for the neutralino mass and boost factor are found within acceptable ranges given current particle physics models [70]:

$$m_\chi = 4747 \text{ GeV} \quad (3.1)$$

$$f = 812 \quad (3.2)$$

A minimal Chi-squared value $\chi^2/\nu = 2.5$ is found for the SSC fit to the data alone, and the combined model improves this to $\chi^2/\nu = 1.6$ as illustrated in Figure 3.9.

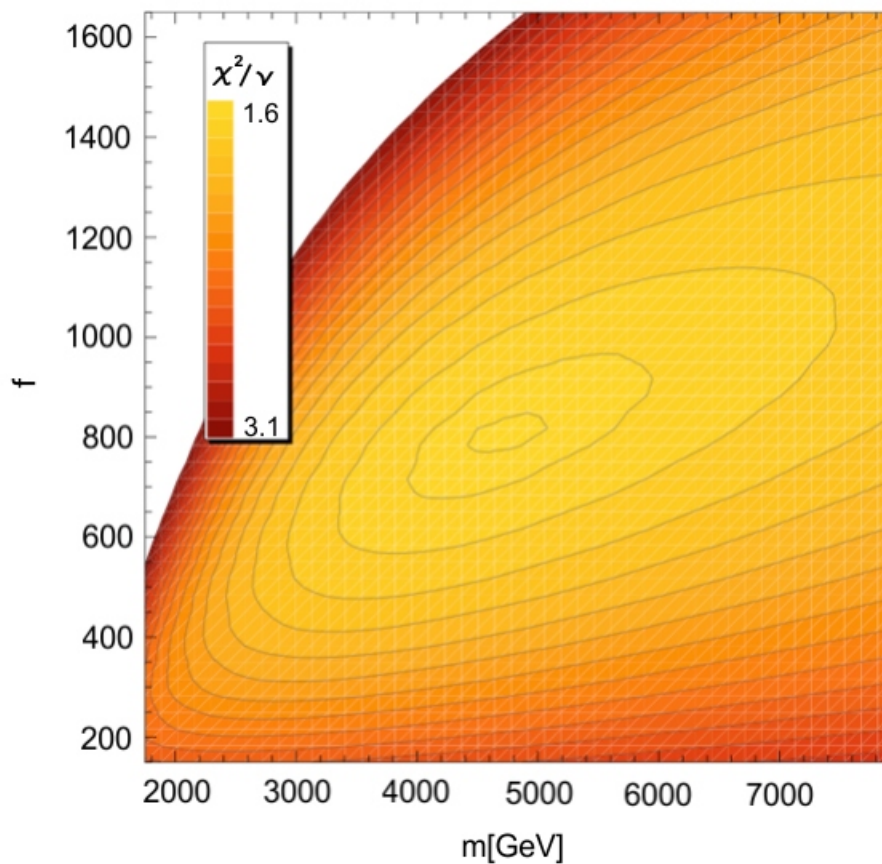


Figure 3.9: Island plot from [70] converging on the best fit boost factor value $f=812$, and WIMP mass $m_\chi=4747$ GeV.

3.6 Summary

A clear picture of M 87 has been obtained through rigorous analysis of the Fermi-LAT spectrum in the range of 300 MeV to 100 GeV γ -rays, and simultaneous optical, ultraviolet and X-ray observations from Swift. The two-zone synchrotron self-Compton model explains the data well and exhibits a double-hump structure, peaking in the optical to ultraviolet range and in γ -rays. The occurrence of a significant excess in VHE γ -rays has motivated a dark matter study. Extraction of dark matter parameters with consideration of annihilating neutralinos close to the black hole has revealed a neutralino mass and boost factor in the range of this excess, of 4747 GeV and 812, respectively, within the predicted mass range of ~ 1 GeV to ~ 10 TeV [86]. The data is more accurately fit by considering the combined SSC and dark matter models rather than SSC alone, and lends support to the annihilation theory.

Chapter 4

NGC 1275

4.1 Introduction

The giant elliptical radio galaxy NGC 1275 ($z = 0.018$) is the central dominant galaxy of the Perseus cluster, with an FRI morphology. Abdo et al. 2009 [87] have investigated the multiwavelength SED of NGC 1275 and noted that overall, it is similar to the SEDs of low frequency BL Lac objects [88]. There are two pronounced components to the SED; these are peaks in the optical to infrared region and in γ -rays, likely due to synchrotron effects in the lower energy regime, and inverse-Compton effects in the higher energy regime, being an SSC case. NGC 1275 is a low peaked BL Lac object, and a TeV emitting source, flaring recently in October 2016 and December 2016 [87], [89]. See Figure 4.1. In this chapter the multiwavelength data for NGC 1275 will be described, and the Fermi-LAT analysis time range determined. The raw data will be analyzed using the Fermi Tools environment, followed by SSC modeling of the source across all energy bands. This will be followed by an analysis of dark matter annihilation near the black hole. A brief study of IC 310 is included at the end, as it is located close to NGC 1275 within the Perseus cluster, and due to low statistics did not warrant an independent chapter.

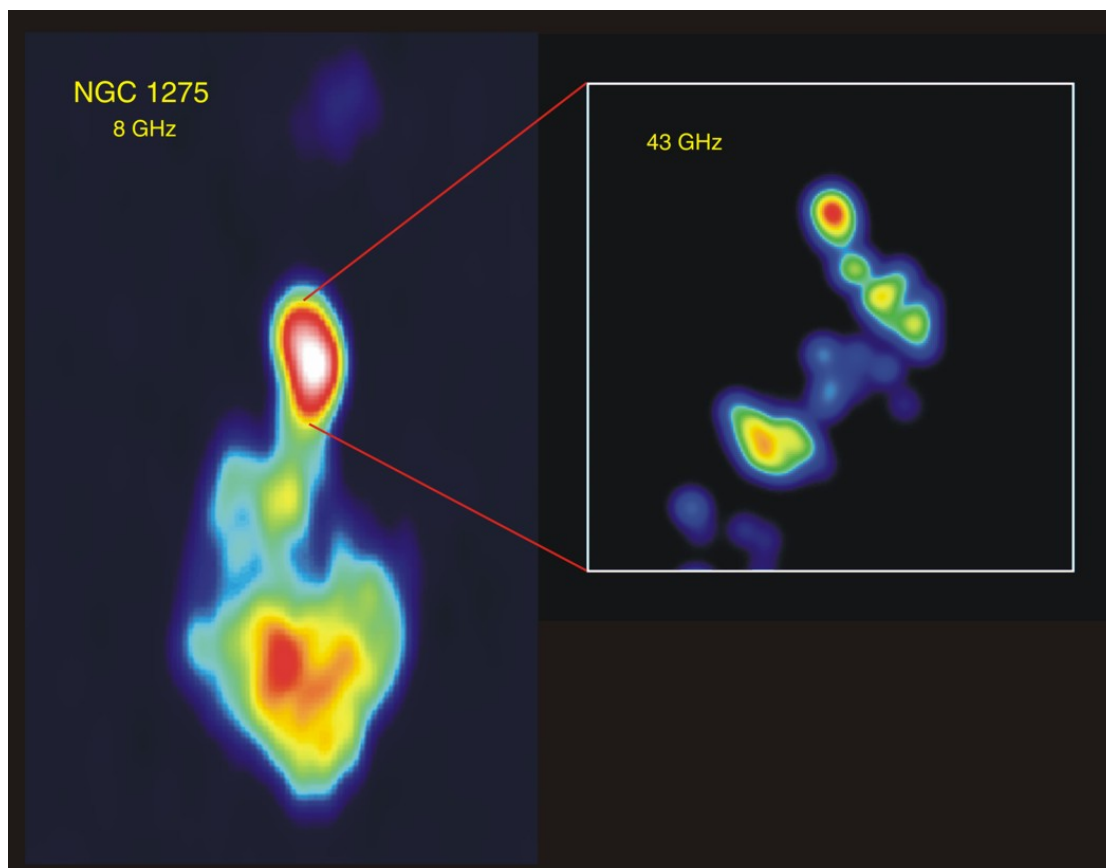


Figure 4.1: NGC 1275 at 8 GHz and 43 GHz. Image courtesy of NRAO/AUI.

4.2 Collection of simultaneous multiwavelength data

A check was made for multiwavelength, simultaneous observations of NGC 1275. In the X-ray regime, there exist publicly available Swift-XRT, Swift-UVOT and Swift-BAT data from July 15 2010 to August 9 2010. In the VHE γ -ray regime there is MAGIC data from August 2010 to February 2011 and a VERITAS upper limit ranging from January 15 2009 to February 26 2009. Thus the Fermi-LAT time interval that will be taken here for the analysis of the raw data, will be certain to directly overlap the MAGIC data, corresponding to Mission Elapsed Time (MET) 302313600 to 320544000. The ROI is around the known coordinates of Fermi-detected γ -ray emission from NGC 1275: R.A. = 49.95 and Dec = 41.51. See Figures 4.2 and 4.3 for the spectral energy distribution of the collection of data thus far, and a schematic representation of the overlapping simultaneous observation times.

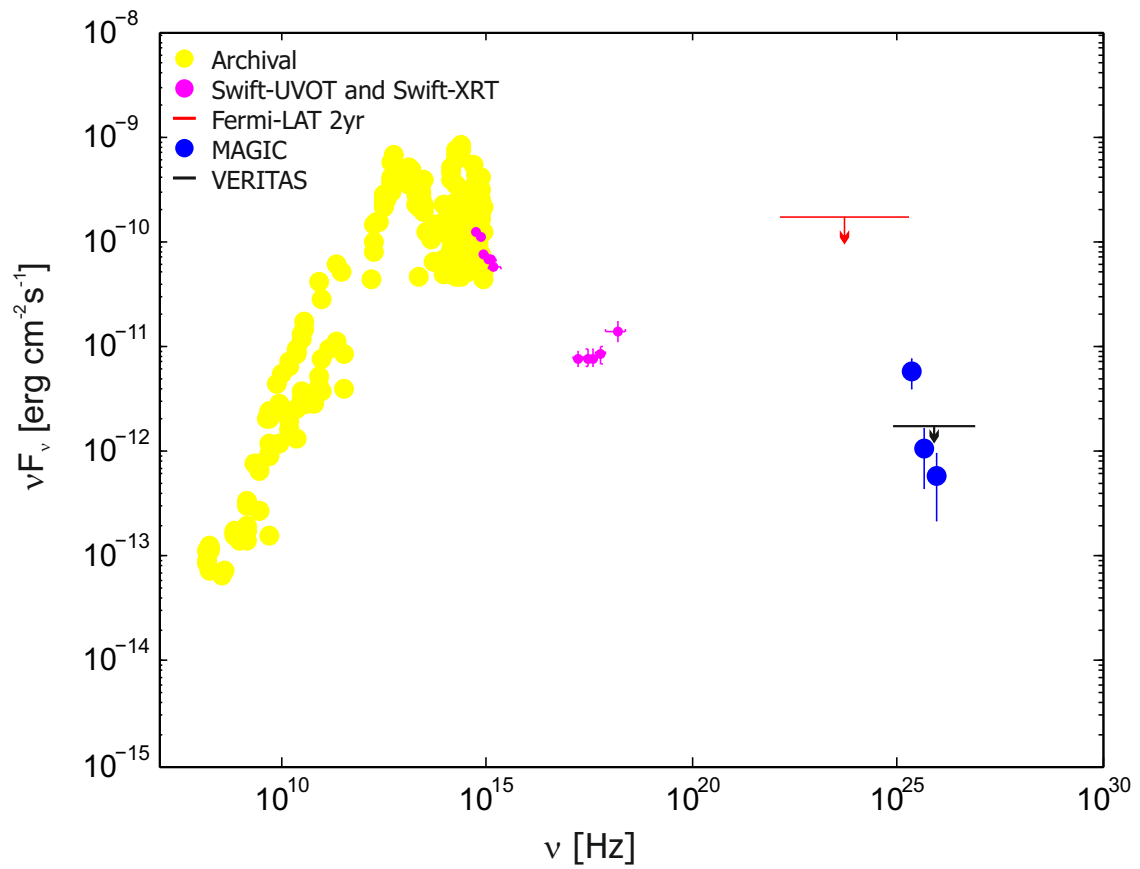


Figure 4.2: Collection of multiwavelength data for NGC 1275. Simultaneous data: Swift-UVOT and Swift-XRT July 15 2010 to August 9 2010. MAGIC data August 2010 to February 2011. Non-simultaneous data: NED archival, Fermi-LAT 2 year upper limit between 100 MeV and 100 GeV is shown by the red line, and the VERITAS upper limit from January 15 2009 to February 26 2009 by the black line.

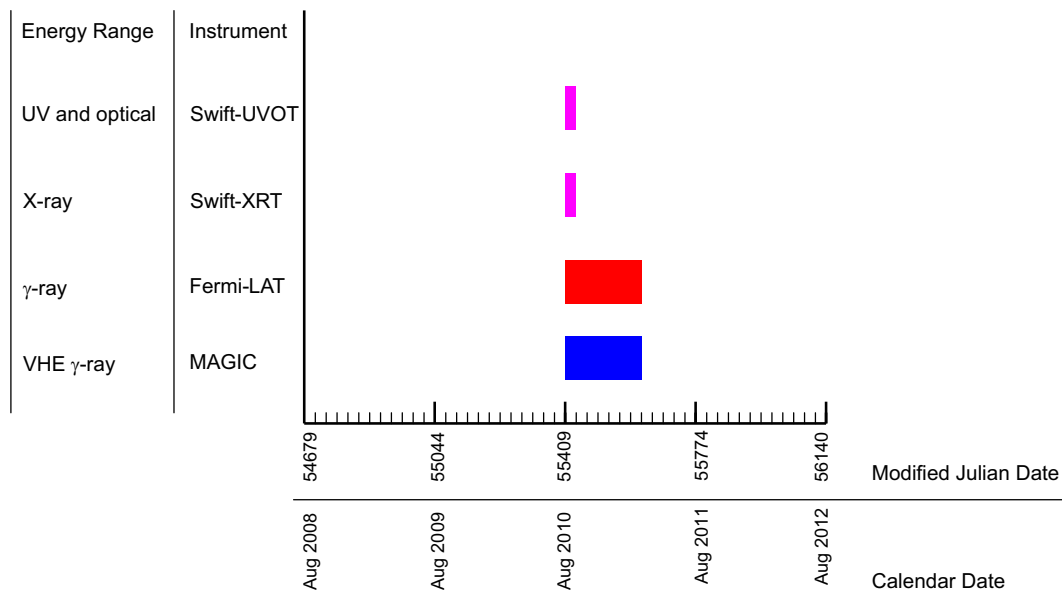


Figure 4.3: Schematic of overlapping observation times for NGC 1275 from different instruments in various energy regimes.

4.3 Results of Fermi Large Area Telescope analysis

Using Fermi Science Tools Version v9r23 as explained in §2.4, the search region was selected, with radius 20° , event class 2 photons, time range MET 302313600 to 320544000, and an energy selection of 300 MeV to 100 GeV. A 3-dimensional counts cube (CCUBE) was constructed in the environment followed by calculation of the largest square contained by the 20° circular region, in order to select the counts map (CMAP). The 2-dimensional CMAP is a square region of 16° by 16° , or 80 pixels in the x-axis and 80 pixels in the y-axis with an image scale of 0.2 degrees/pixel, as shown in Figure 4.4. The colour scheme indicates the number of counts detected by the telescope during the selected time range, at each x-y coordinate.

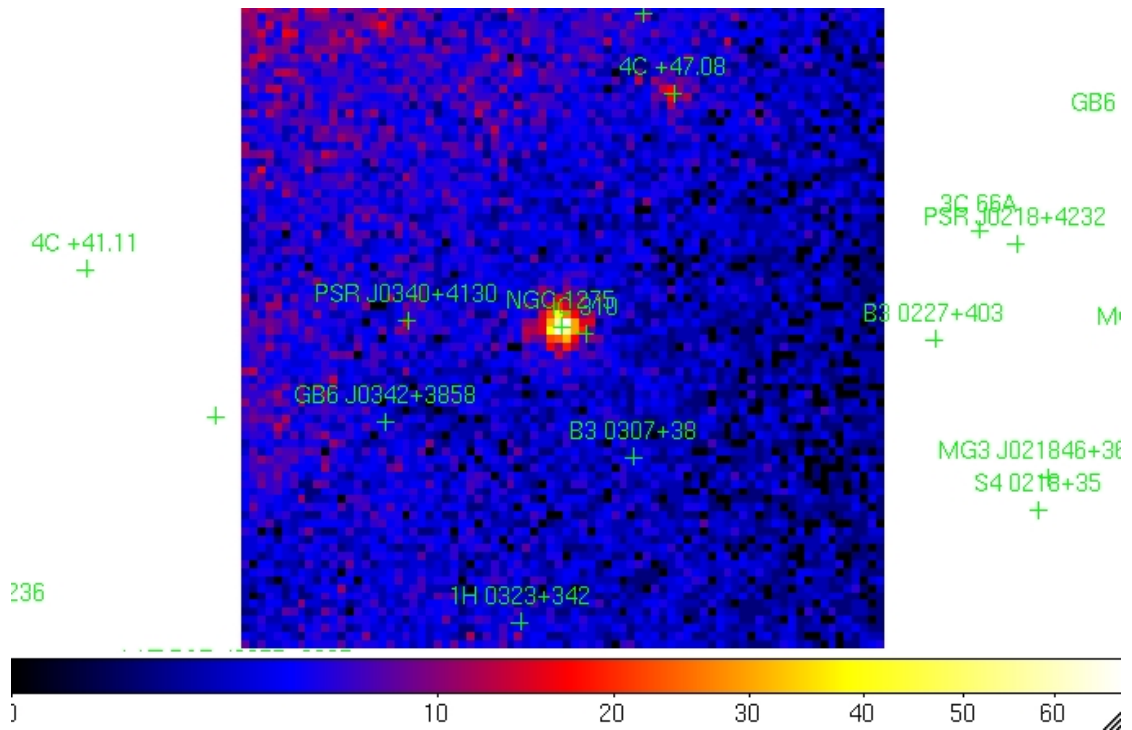


Figure 4.4: Fermi-LAT counts map centred on NGC 1275 (R.A. = 49.95, Dec = 41.51).

A model file of the region describing every source in the region, was constructed in the analysis environment by considering the galactic diffuse background and isotropic diffuse background data, as well as the cumulative collected data for this region in the specific time and energy selections. Utilizing the binned analysis algorithm to create the exposure map or ‘exp cube,’ and running the source maps tool, a likelihood fit was followed through. The likelihood fit was approached twice in series: first with a coarse optimization algorithm, then with a finer algorithm. The first optimization algorithm, DRMNF, was run with an altered model file that had only the 8 most prominent sources captured in the box region. The fit parameters were set to ‘free’ instead of ‘fixed.’ In the case of convergence, this alteration allowed the likelihood tool to calculate a more precise fit. The 8 sources in the box region are listed in Table 4.1:

Table 4.1: Brightest sources and their test statistic values in the 16° by 16° region of interest selected for radio galaxy NGC 1275, corresponding to Figure 4.4.

Common Name	Catalog Designation	TS
NGC 1275	2FGLJ0319.8+4130	3291.3
IC 310	2FGLJ0316.6+4119	0.02
PSR J0340+4130	2FGLJ0340.4+4131	88.2
GB6 J0342+3858	2FGLJ0342.4+3859	0.8
B3 0307+38	2FGLJ0310.7+3813	7.3
1H 0323+342	2FGLJ0324.8+3408	22.9
4C +47.08	2FGLJ0303.5+4713	212.9
No Association	2FGLJ0307.4+4915	10.8

Convergence time for the coarse optimizer was negligible, yielding a log likelihood value of 49016.4, total number of observed counts 24248, total number of model events 24248.4, and fit details for each source. These served as a reasonable first estimate. Conducting a second iteration of the likelihood routine using the fine optimizer NEWMINUIT, lasted much longer and yielded a log likelihood value of also 49016.4, total number of observed counts 24248, total number of model events 24248.7, and fit details for each source. The best fit for NGC 1275 was a log parabola with an integral flux of $1.06 \times 10^{-7} \pm 3.64 \times 10^{-9}$ ph/cm²/s (§A.2.2). The Fermi-LAT spectral energy distribution resulted in 7 points, as shown in Figure 4.5. Further fitting details for NGC 1275 can be found in §A.

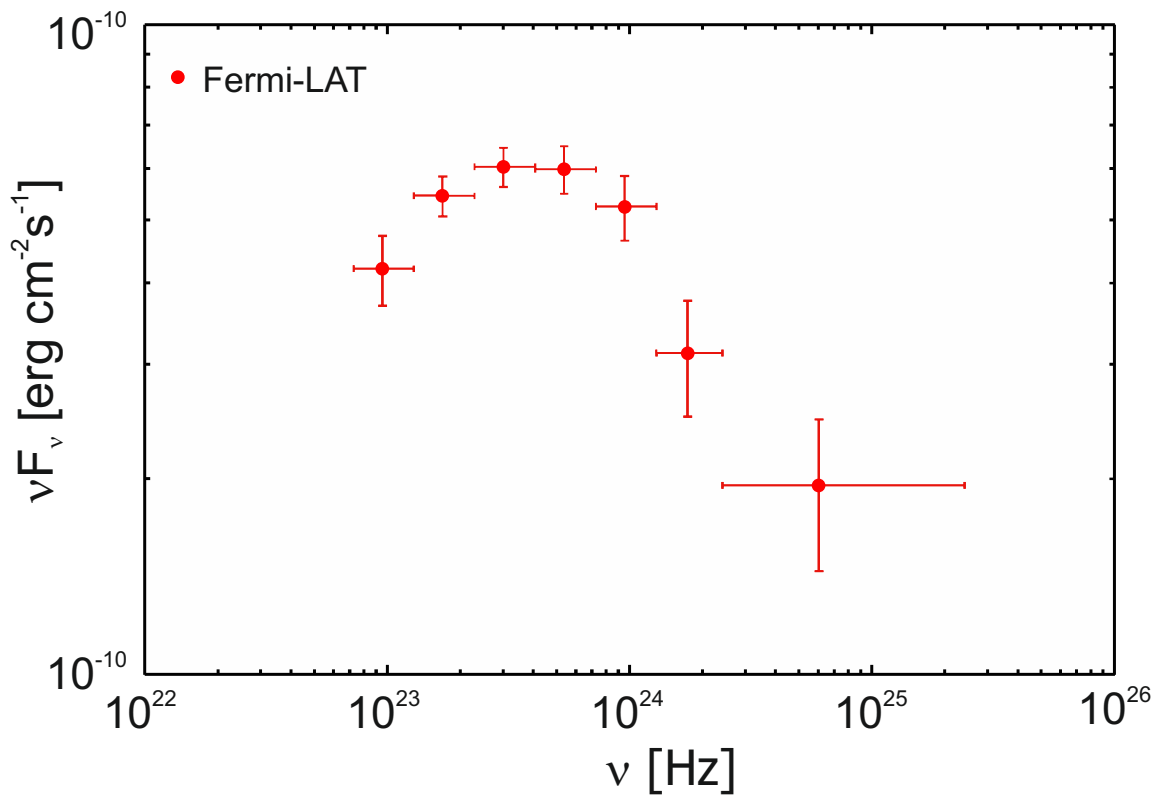


Figure 4.5: The Fermi-LAT spectral energy distribution of NGC 1275.

IC 310 was not a significant detection in the region of NGC 1275. The TS value of IC 310 was found to be 0.02, or nearly zero, most likely due to the very short time range of 6 months and insufficient collection of events, whereas other investigations with time intervals of approximately two years have been able to find a detection for this source. IC 310 will be revisited at the end of this chapter. The TS value of NGC 1275 was 3291.3, indicating a detection far above 5 sigma. Figures A.5 to A.8 in §A.1.2 show the counts versus energy distribution coming from the entire region of interest, the residuals plot, test statistic map, and count spectrum.

4.3.1 Comparison of results

Another Fermi-LAT analysis is described in [87], over a shorter 4 month time period (August 4 2008 to December 5 2008, MET 239557417 to 250134308), from 100 MeV to 300 GeV. The following power law spectrum was found:

$$\frac{dN}{dE} = (2.45 \times 10^{-9} \pm 0.26 \times 10^{-9}) \left(\frac{E}{100 \text{ MeV}} \right)^{-2.17 \pm 0.04} \text{ ph/cm}^2/\text{s/MeV}. \quad (4.1)$$

When this spectrum is integrated over the energy selection from this analysis in this work, an integral flux of 0.58×10^{-7} ph/cm²/s is achieved, on a similar order of magnitude as the analysis above.

4.4 Results of multiwavelength analysis

The spectral energy distribution of NGC 1275 is revised from Figure 4.2 by including the results of the Fermi-LAT analysis conducted in Figure 4.5. The multiwavelength data are fit in Figure 4.6 with the two-zone SSC model described in §2.5.2, with the host galaxy modeled by a planck spectrum. The spectrum is dominated by host galaxy contributions in the optical range, and exhibits a double-hump structure.

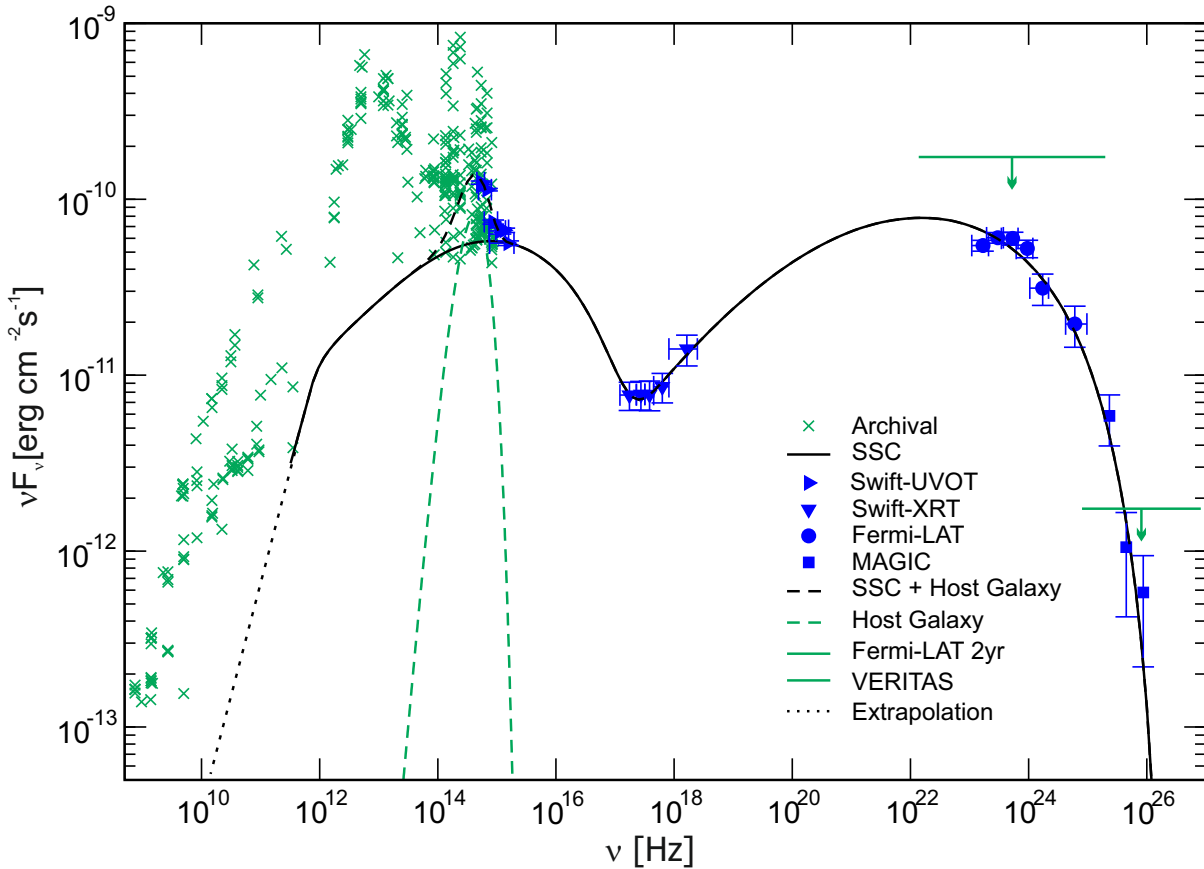


Figure 4.6: Multiwavelength spectral energy distribution and SSC fit of NGC 1275. Blue data is considered in the fit and green data is used as a guide.

The injected electron number density is $K = 1.9 \times 10^6$ cm⁻³, Lorentz factor is $\Gamma = 15$, and the magnetic field in the jet is $B = 0.28$ G. The radiation and

acceleration zone radii are $R_{rad} = 2.5 \times 10^{15}$ cm and $R_{acc} = 3.5 \times 10^{14}$ cm, with an acceleration to escape timescale ratio of $\frac{t_{acc}}{t_{esc}} = 1.40$, and a Fermi I to Fermi II acceleration ratio of $a = 150$. The doppler factor is $\delta = 32.5$.

The Fermi-LAT data is peaked, and the first data point is not considered in the fitting as systematic error is known to be highest in the lowest energy bin. A promising overall model is produced, which is especially consistent in the Swift-XRT regime and archival data regime.

4.4.1 Comparison of results

The γ -ray flux peak height was found here to be comparable to the radio to optical flux peak height, as was also the case in the study by Abdo et al. [87].

In [87], a one-zone SSC model and a decelerating flow model as introduced in §2.5.3, were attempted in order to describe the SED, and both provided an adequate fit. The SSC was conducted as in [90] employing a bulk Lorentz factor of $\Gamma = 1.8$, doppler factor $\delta = 2.3$, comoving radius of jet emission region 2×10^{18} cm, which relates to a variability timescale of approximately 1 year, and $B = 0.05$ G with an inclination angle $\Theta = 25^\circ$. A nonthermal electron distribution was taken as a broken power law ($n(\gamma) \propto \gamma^{-p}$) with number indices $p_1 = 2.1$ for γ between 800 and 960, and $p_2 = 3.1$ for γ between 960 and 4×10^5 . The data in the spectral energy distribution were Fermi-LAT analysis between August 4 2008 and December 5 2008 (MET 239557417 to 250134308), with simultaneous radio data from RATAN-600, core radio MOJAVE data, and optical MITSuME observations. The Swift-UVOT data were December 2007 archival, and there was no simultaneous VHE data. The resulting SSC fit is shown in Figure 4.7. The decelerating flow model as in [80] was implemented with the jet starting with a bulk Lorentz factor of $\Gamma_{max} = 10$ which decelerates to $\Gamma_{min} = 2$ over 5×10^{17} cm. The diameter of the flow cross-section at the inlet is 3×10^{16} , magnetic field at the base $B = 0.2$ G, $\Theta = 20^\circ$, and the injected power law electron distribution $n(\gamma) \propto \gamma^{-p}$ has an index $p = 1.8$ extending from $\gamma_{min} = 800$ to $\gamma_{max} = 1.0 \times 10^5$.

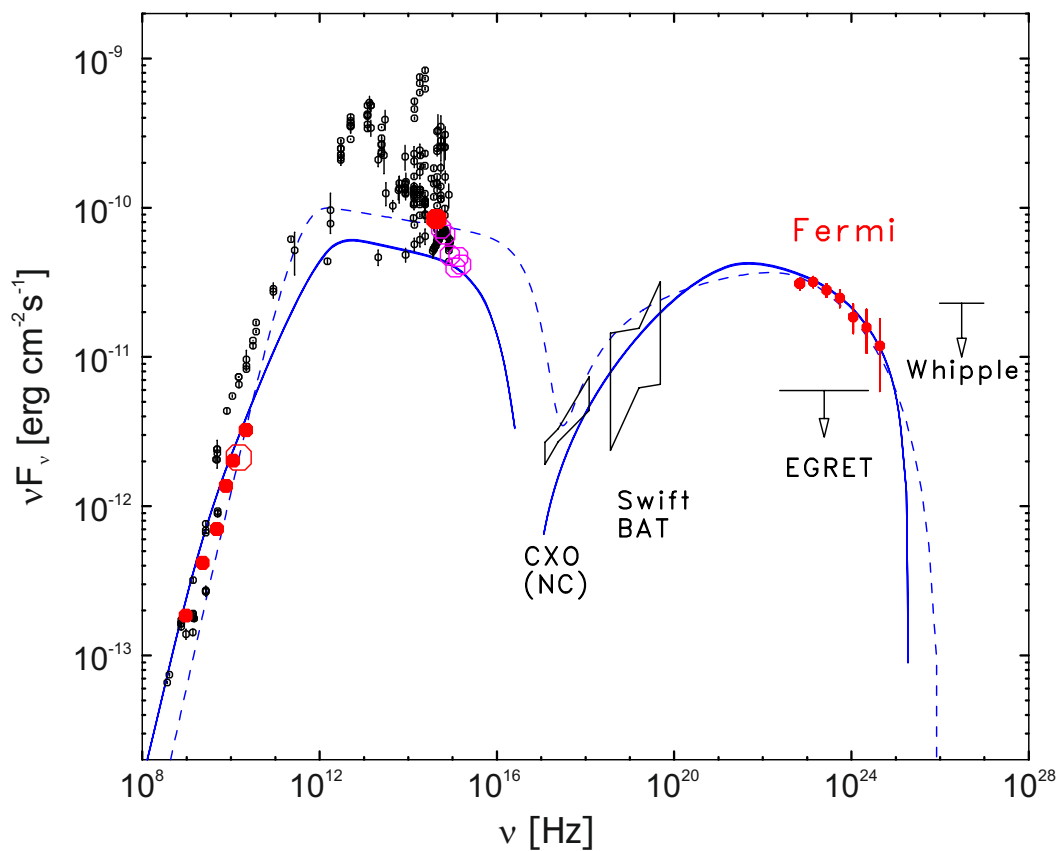


Figure 4.7: Abdo et al. 2009 [87] one-zone SSC fit of NGC 1275 with Fermi-LAT data between August 4 2008 and December 5 2008 (MET 239557417 to 250134308), and simultaneous radio data from RATAN-600, core radio MOJAVE data, and optical MITSuME observations. Swift-UVOT data is archival from December 2007, EGRET and Whipple upper limits are shown for reference but not considered in the fit, and there is no simultaneous VHE data.

4.5 Results of dark matter analysis

Returning to the multiwavelength spectral energy distribution and SSC fit of NGC 1275 in Figure 4.6, the dark matter model from §2.6 is applied with a thermally averaged annihilation cross-section $\langle\sigma_A v\rangle = 3 \times 10^{-24} \text{ cm}^3/\text{s}$. A prompt pion signature is discovered, peaking near 10^{26} Hz :

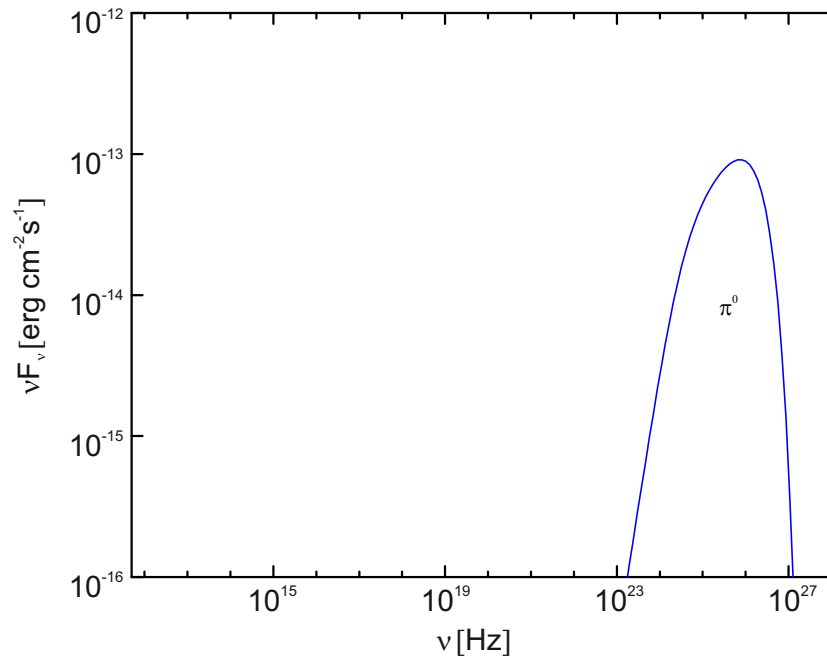


Figure 4.8: Prompt pion peak for annihilating neutralinos in NGC 1275, following from the dark matter model described in §2.6.

An inverse-Compton flux peak for generic annihilating WIMPS is obtained near 10²² Hz:

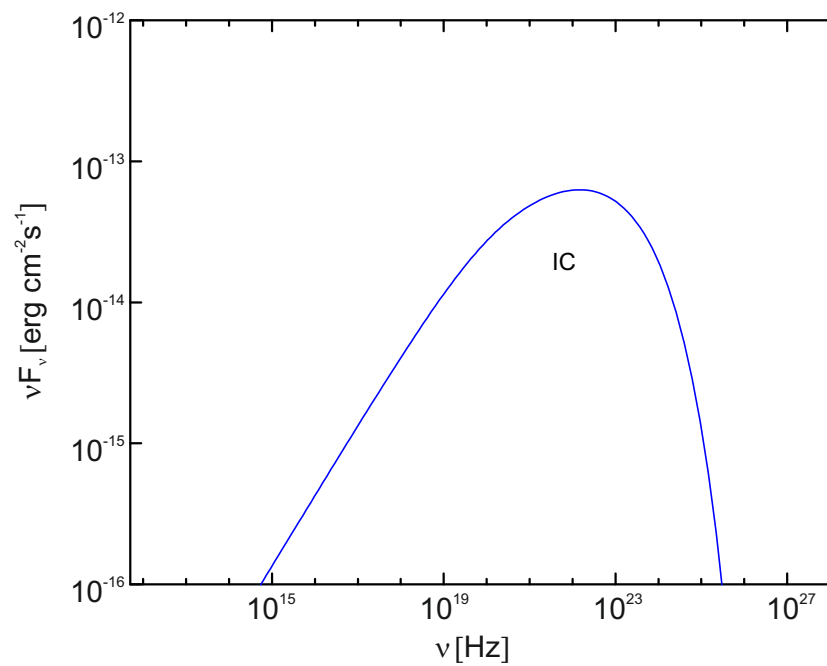


Figure 4.9: Inverse-Compton signature for annihilating neutralinos in NGC 1275.

Summing the fluxes from the dark matter emission with the nonthermal multiwavelength emission calculated for NGC 1275 gives the combined model depicted in Figure 4.10. Minimizing the Chi-squared value of the summed curve with respect to the data points and their error bars, allows the extraction of raw values for m_χ and f as conducted previously for M 87. It is found for NGC 1275 that

$$m_\chi = 4793 \text{ GeV} \quad (4.2)$$

$$f = 141 \quad (4.3)$$

Applying the same analysis methods for NGC 1275 as for M 87 has yielded a lower boost factor, however interestingly, a very similar neutralino mass: $m_{\chi_{M87}} \approx 4.7 \text{ TeV}$ and $m_{\chi_{NGC1275}} \approx 4.8 \text{ TeV}$.

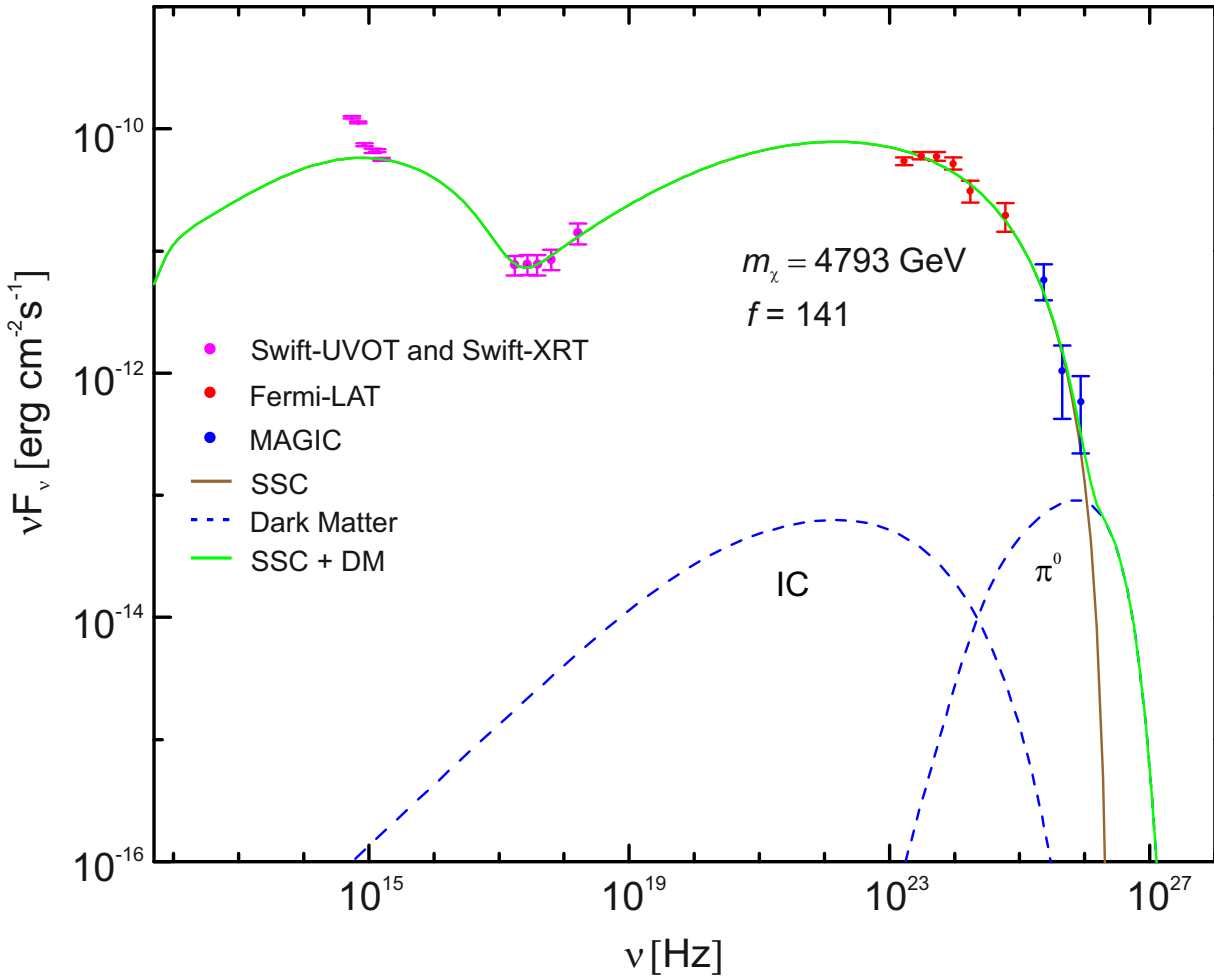


Figure 4.10: The summed curve for NGC 1275 in red, resulting from the addition of the dark matter fluxes in blue, with the SSC model in black.

4.6 IC 310

IC 310 ($z = 0.019$), also located in the Perseus cluster, is located only 0.6° from NGC 1275, and is strongly occulted by it. Given its harder spectrum, IC 310 becomes visible over NGC 1275 only at higher energies [91]. Figure 4.11 illustrates the differences in γ -ray emission by NGC 1275 and IC 310, through images of the same region containing both sources at increasing energy selections.

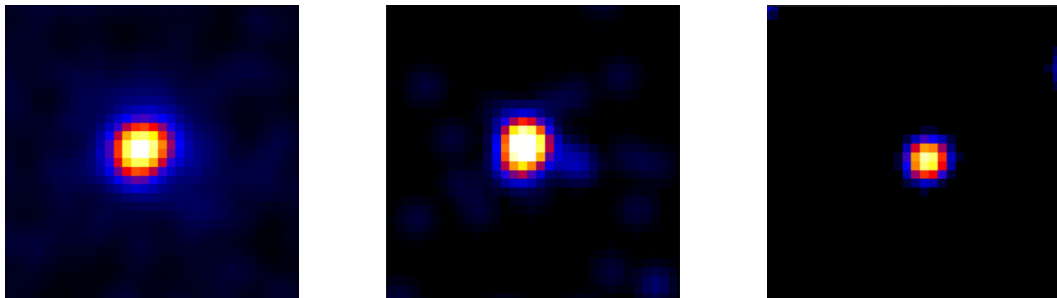


Figure 4.11: IC 310 and NGC 1275. Left panel: The energy range of the image is 1 GeV to 10 GeV. Only γ -ray emission from NGC 1275 is visible. Middle panel: The energy range of the image is 10 GeV to 100 GeV. γ -ray emission from IC 310 becomes visible to the right. Right panel: The energy range of the image is above 100 GeV. γ -ray emission from IC 310 has a high count rate, and γ -ray emission from NGC 1275 is no longer detected. Images from [91]. Credit: NASA/DOE/LAT Collaboration and A. Neronov et al.

4.6.1 Collection of simultaneous multiwavelength data

Multiwavelength data available for IC 310 included VHE stereo-detection by the MAGIC telescope system between October 2009 and February 2010 [92]. As well, there were simultaneous Swift-XRT, Swift-UVOT and Swift-BAT data from the Swift Master Catalog [43] in the X-ray regime, from January 26 2012 to January 30 2012. Therefore Fermi-LAT data which is simultaneous to the MAGIC time period is selected for analysis.

4.6.2 Results of Fermi Large Area Telescope analysis

Due to the steep spectrum of IC 310 and proximity to NGC 1275, 10 GeV was selected as a lower energy limit for the analysis. Research into literature also showed that Neronov et al. [93] made detections of 5 photons between 30

GeV and 300 GeV, over a time period of 1.5 years from August 4 2008 to February 14 2010.

In terms of time selection, the MAGIC-simultaneous time range of four months was initially chosen, which did not yield a TS value above 9. Given the constraints of the steep spectrum, the general weakness of IC 310 as a source, and the naturally occurring low statistics at high energies, it could very well be possible that no photons were detectable in this time period.

After conducting numerous analysis iterations, and more lenient selections ventured in an attempt to capture evidence of the γ -ray emission associated with IC 310, an upper limit of 1.23×10^{-11} erg/cm²/s with a TS value of 7.9 between October 2009 and October 2010 was calculated, centred at R.A. = 49.1793, Dec = 41.3248. As this TS value does not meet the criterion required in this work, IC 310 was excluded from further analysis.

4.7 Summary

NGC 1275 was observed by the ground-based VHE γ -ray telescope MAGIC, in 2010. Fermi-LAT γ -ray data has therefore been analyzed here, from 300 MeV to 100 GeV in the same time period, and 7 data points discovered. Swift-UVOT and Swift-XRT data is included in the multiwavelength spectrum, providing unparalleled coverage of the source over more than ten orders of frequency magnitude. The leptonic SSC study has resulted in a double-hump signature that explains the simultaneous data and even the high energy non-simultaneous data well. In the optical to ultraviolet range the measurements show a peak, which can be explained by the addition of γ -rays from the host galaxy. The neutralino mass has been found to be 4793 GeV, similar to M 87, within the predicted mass range of ~ 1 GeV to ~ 10 TeV [86]. IC 310 is overpowered by NGC 1275, and an above 4 sigma detection for IC 310 is not achieved.

Chapter 5

Pictor A

5.1 Introduction

Pictor A ($z = 0.035$) is an FR II radio galaxy, with its highest surface brightness feature farther from the core, and has been classified as a broad line radio galaxy (BLRG) [94]. The total radio emission is observed in its giant radio lobes [95]. Centaurus A, also known for its large radio lobes, has distinct γ -ray emission originating from the lobes as resolved by [96]. Evidence for γ -ray emission from other AGN lobes, such as Pictor A, is thus far rare, and the discovery of γ -ray emission from Pictor A was recently confirmed by [51] using three years of Fermi-LAT data. Furthermore, γ -ray flux variability on timescales of one year or less has been observed in Pictor A [51]. Here, the multiwavelength data for Pictor A will be described, the Fermi-LAT analysis time range determined, and the data will be analyzed using the same methodology as for M 87 and NGC 1275. The multiwavelength spectrum will then be modeled using both the leptonic and hybrid SSC approaches detailed in §2.5.

5.2 Collection of simultaneous multiwavelength data

As of yet there have been no VHE observations of Pictor A, however optical, ultraviolet and X-ray observations have been documented by Swift [43], providing simultaneous Swift-XRT, Swift-UVOT and Swift-BAT data from October 31 2010. For the purposes of the Fermi-LAT analysis, the localization of the γ -ray emission is taken as stated to be associated with Pictor A [51]: R.A. =

80.17, Dec = -45.61. The ROI is centred on R.A. = 80.57, Dec = -42.66 and uses nearly 4 years of data collected since the start of the Fermi-LAT Mission (August 4 2008 MET 239557417 to June 25 2012 MET 362319933). Figures 5.1 and 5.2 depict the spectral energy distribution of the collected data, and the overlapping time ranges.

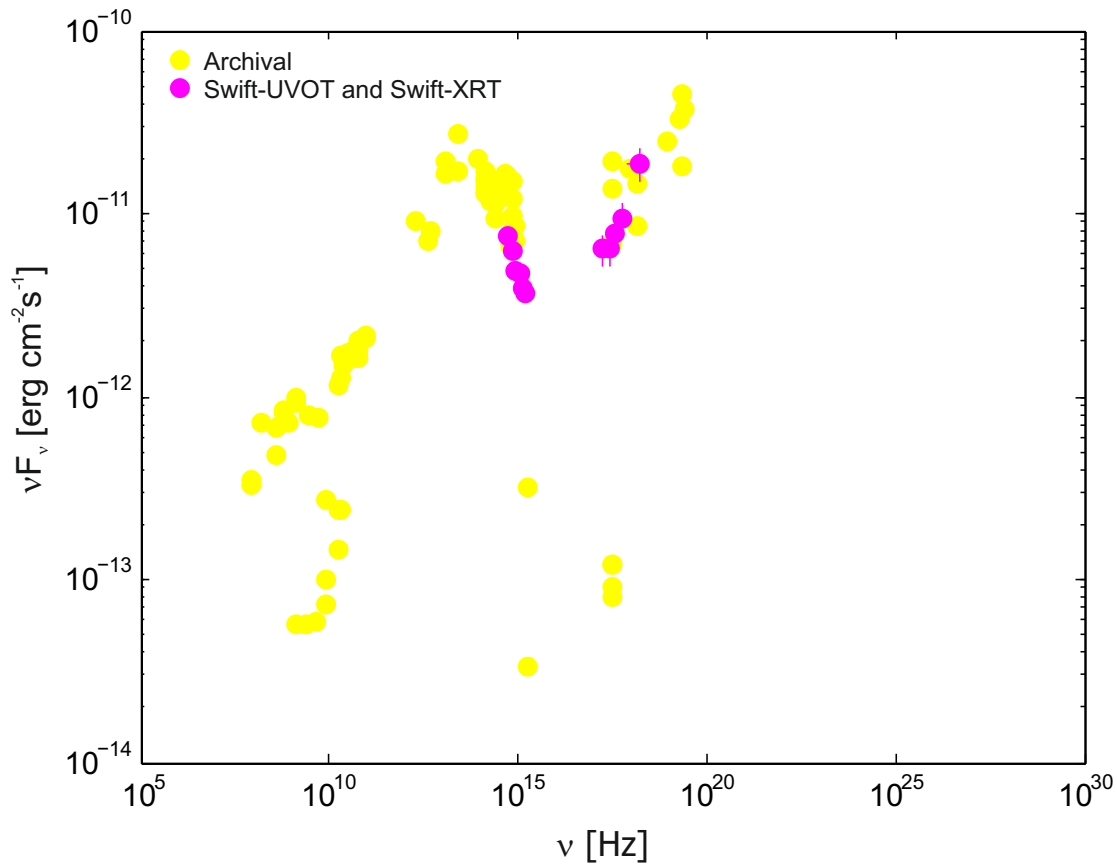


Figure 5.1: Collection of multiwavelength data for Pictor A. Simultaneous data: Swift-UVOT and Swift-XRT from October 31 2010 in magenta. Non-simultaneous data: NED archival in yellow.

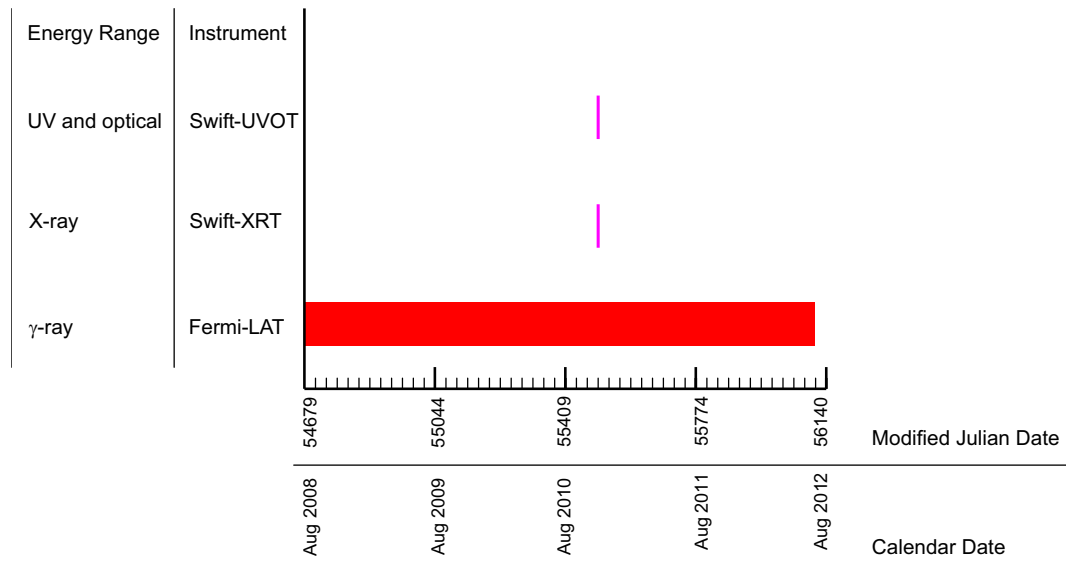


Figure 5.2: Schematic of overlapping observation times for Pictor A from Fermi-LAT, Swift-UVOT and Swift-XRT.

5.3 Results of Fermi Large Area Telescope analysis

The recent interesting publication by Brown and Adams [51], claimed a discovery of Pictor A in the γ -ray energy regime using publicly available data and analysis tools. Using an energy selection of 200 MeV to 300 GeV, the discovery was localized at R.A. = 80.17, Dec = -45.61, with an integral flux of $5.8 \times 10^{-9} \pm 0.7 \times 10^{-9}$ ph/cm²/s and power law fit

$$\frac{dN}{dE} = (4.23 \times 10^{-10} \pm 0.44 \times 10^{-10}) \left(\frac{E}{100 \text{ MeV}} \right)^{-2.93 \pm 0.03} \text{ ph/cm}^2/\text{s/MeV} \quad (5.1)$$

which provided additional motivation for an independent analysis to be conducted in this work. In the analysis conducted here, the full time selection of all cumulative Fermi-LAT data is taken; namely 4 years of data collected since the start of the Fermi-LAT mission (August 4 2008 MET 239557417 to June 25 2012 MET 362319933). The analysis region was not centred exactly on the point defined by [51], rather modified and centred on R.A. = 80.57, Dec = -42.66, in order to ensure inclusion of other relevant nearby bright sources, in the ROI. See Figure 5.3.

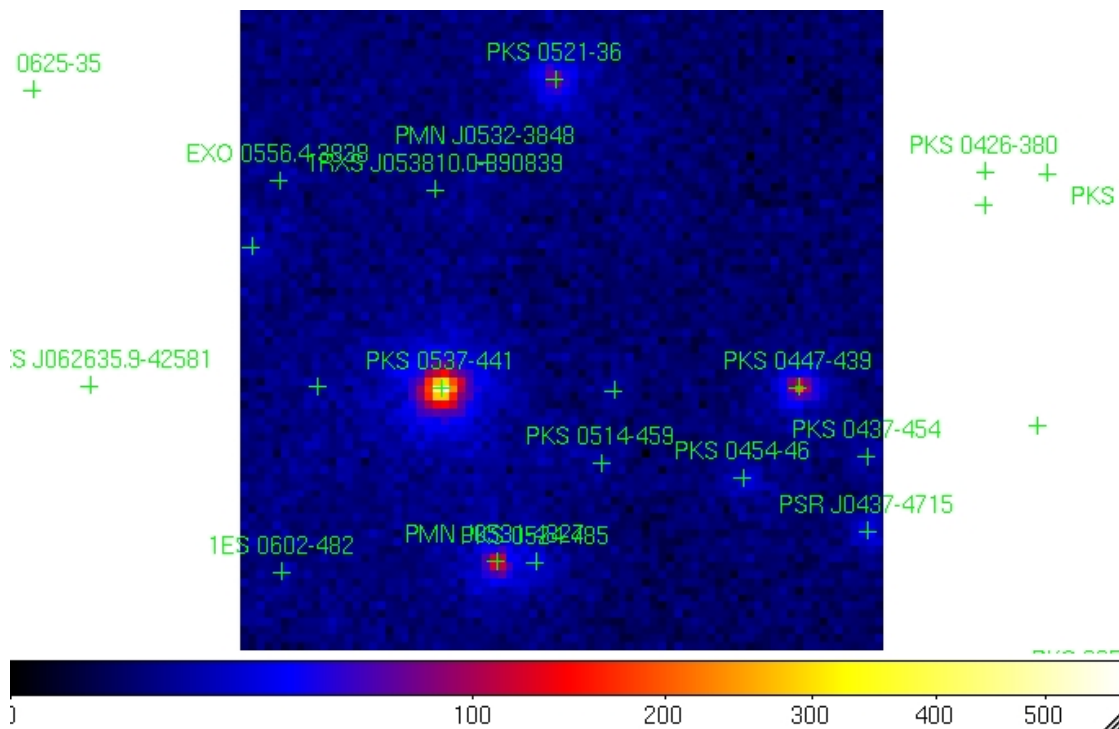


Figure 5.3: The Pictor A region of interest centred on R.A. = 80.57, Dec = -42.66. From a previous study there is evidence of γ -ray emission expected at R.A. = 80.17, Dec = -45.61 [51].

Gtselect was run over the aforementioned time range, and 20° about the search centre, followed by gtmktime which employed the ROI-based zenith angle cut, and gtbin to produce an 80 pixel by 80 pixel CMAP and CCUBE. To construct the model file, the entry for Pictor A was manually input, and fit parameters were set to 'free.' Gtlcube and gtexpcube2 with 300 x-pixels and 300 y-pixels between 300 MeV and 100 GeV were run, followed by gtsr-cmaps, capturing 17 bright sources in the ROI (see Table 5.1).

Table 5.1: Brightest sources and their test statistic values in the 16° by 16° region of interest selected for radio galaxy Pictor A, corresponding to Figure 5.3.

Common Name	Catalog Designation	TS
PKS 0521-36	2FGLJ0523.0-3628	2626.2
PMN J0532-3848	2FGLJ0531.8-3831	48.4
EXO 0556.4-3838	2FGLJ0558.2-3837	70.5
1RXS J053810.0-390839	2FGLJ0538.5-3909	43.4
No Association	2FGLJ0602.7-4011	175.5
No Association	2FGLJ0555.9-4348	30.7
PKS 0537-441	2FGLJ0538.8-4405	31376.7
No Association	2FGLJ0515.0-4411	44.3
1ES 0602-482	2FGLJ0604.2-4817	68.4
PMN J0531-4827	2FGLJ0532.0-4826	4163.1
PKS 0524-485	2FGLJ0526.1-4829	181.4
PKS 0514-459	2FGLJ0516.5-4601	41.9
PKS 0454-46	2FGLJ0456.1-4613	437.5
PKS 0447-439	2FGLJ0449.4-4350	6210.8
PKS 0437-454	2FGLJ0438.8-4521	162.5
PSR J0437-4715	2FGLJ0437.3-4712	660.1
Pictor A	-	13.9568

Binned analysis with `gtlike` and the coarse `DRMNFB` optimizer, followed by the fine `MINUIT` optimizer, successfully converged, and yielded a log likelihood value of 56927.0, plus fit information for the 17 bright sources. See §A.1.3 and Figures A.9 to A.12.

A rough check of the fit was made using the `farith` command, by subtracting the CMAP from a map of the model file for every point. This produced an 80 pixel by 80 pixel image with nearly all zero (black) photon counts at every point. Note that a perfect fit would be represented by a completely flat subtraction, i.e. the map would appear entirely black.

The resulting power law fit for 4 years of data (§A.2.3), considering a 4 sigma detection limit with an integral flux of $1.20 \times 10^{-9} \pm 5.84 \times 10^{-10}$ ph/cm²/s, had three upper limits. This is shown in Figure 5.4.

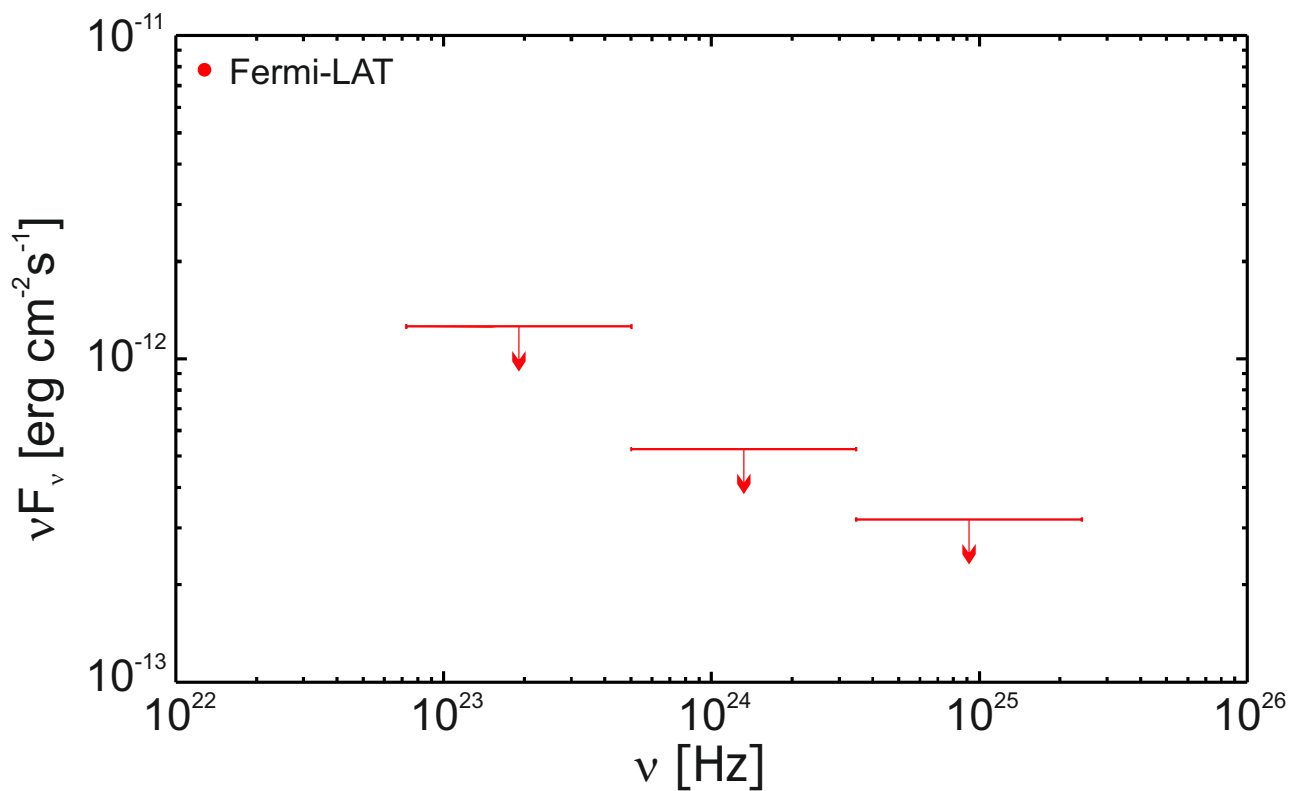


Figure 5.4: Power law Fermi-LAT spectral energy distribution of Pictor A.

5.3.1 Comparison of results

To compare this result with that of [51], this power law fit (§A.2.3, Figure 5.4) was integrated over the 200 MeV to 300 GeV energy selection of [51], resulting in an integral flux on the same order of magnitude i.e. 5.04×10^{-9} ph/cm²/s.

5.4 Results of multiwavelength analysis

The Fermi-LAT analysis as shown in Figure 5.4 is added to the multiwavelength SED as depicted in Figure 5.1. The multiwavelength spectrum of *Pictor A* is fit with both the SSC and the hybrid models which involve leptons and leptons with hadrons respectively (§2.5.2) in Figure 5.5. The hybrid fit has extragalactic background light absorbed, and a fixed ratio between the protons and leptons is implemented.

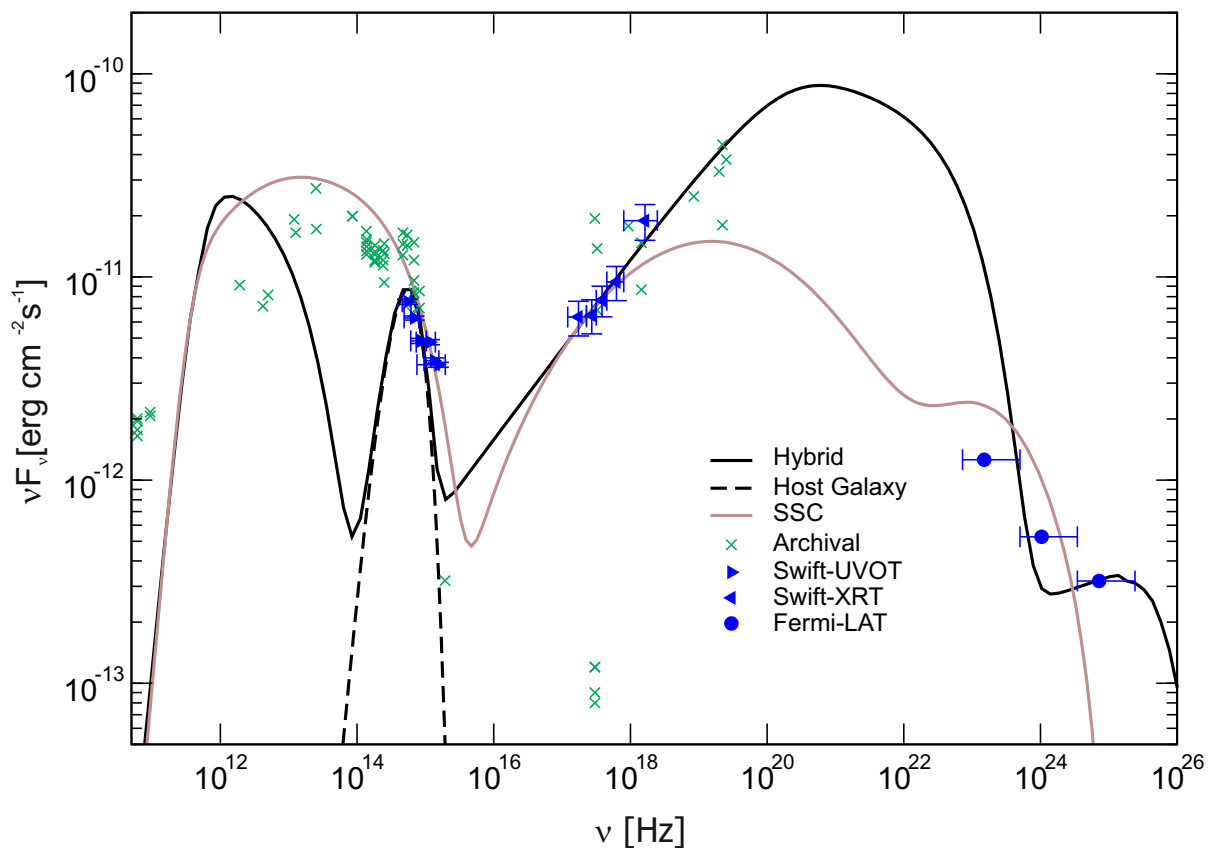


Figure 5.5: SSC and hybrid fits of *Pictor A* modeled on simultaneous Fermi-LAT, Swift-XRT and Swift-UVOT data.

In the leptonic SSC case, the injected electron number density is $K = 2.5 \times 10^5 \text{ cm}^{-3}$, Lorentz factor is $\Gamma = 65$, and magnetic field in the jet is $B = 0.47 \text{ G}$. The radiation and acceleration zone radii are $R_{rad} = 2.95 \times 10^{16} \text{ cm}$ and $R_{acc} = 1.77 \times 10^{15} \text{ cm}$, with an acceleration to escape timescale ratio of $\frac{t_{acc}}{t_{esc}} = 1.11$, and a Fermi I to Fermi II acceleration ratio of $a = 100$. The doppler factor is $\delta = 21$.

In the hybrid scenario, the injected proton number density is $K_p = 1.9 \times 10^{11} \text{ cm}^{-3}$, the proton Lorentz factor is $\Gamma_p = 10$, the injected electron number

density is $K = 8.6 \times 10^9 \text{ cm}^{-3}$, Lorentz factor is $\Gamma = 30$, and magnetic field in the jet is $B = 18 \text{ G}$. The radiation and acceleration zone radii are $R_{rad} = 7.25 \times 10^{16} \text{ cm}$ and $R_{acc} = 3.65 \times 10^{13} \text{ cm}$, with an acceleration to escape timescale ratio of $\frac{t_{acc}}{t_{esc}} = 1.19$, and a Fermi I to Fermi II acceleration ratio of $a = 50$. The doppler factor is $\delta = 11$.

Zhang 2009 [97] predicted the origin of the high energy emission to be from what is known in the radio lobes as the Western Hot Spot (WHS), and Brown et al. 2012 [51] address this question. A one-zone SSC approach is used with historical radio data, infrared, optical and X-ray data, with flux measurements originating from the WHS; the Fermi-LAT analysis is from August 4 2008 to August 8 2011 (MET 239557417 to MET 334486765), and additionally a H.E.S.S. upper limit is measured between 2005 and 2007 which is not simultaneous to the Fermi-LAT data [51]. In the first modeling approach γ -rays are included and X-rays excluded; the parameters are changed in order to fit the radio to optical and γ -ray regions. Attempting to fit the γ -rays overpredicts the X-ray flux compared to the observed data (Figure 5.6). In the second approach X-rays are included and γ -rays excluded; parameters are changed in order to fit the radio to optical, and X-ray regions. This underpredicts the γ -ray flux compared to the observed data (Figure 5.7). Thus both attempts do not succeed in fitting the entire spectrum, and the X-ray and γ -ray data cannot be simultaneously reconciled using the WHS theory [51].

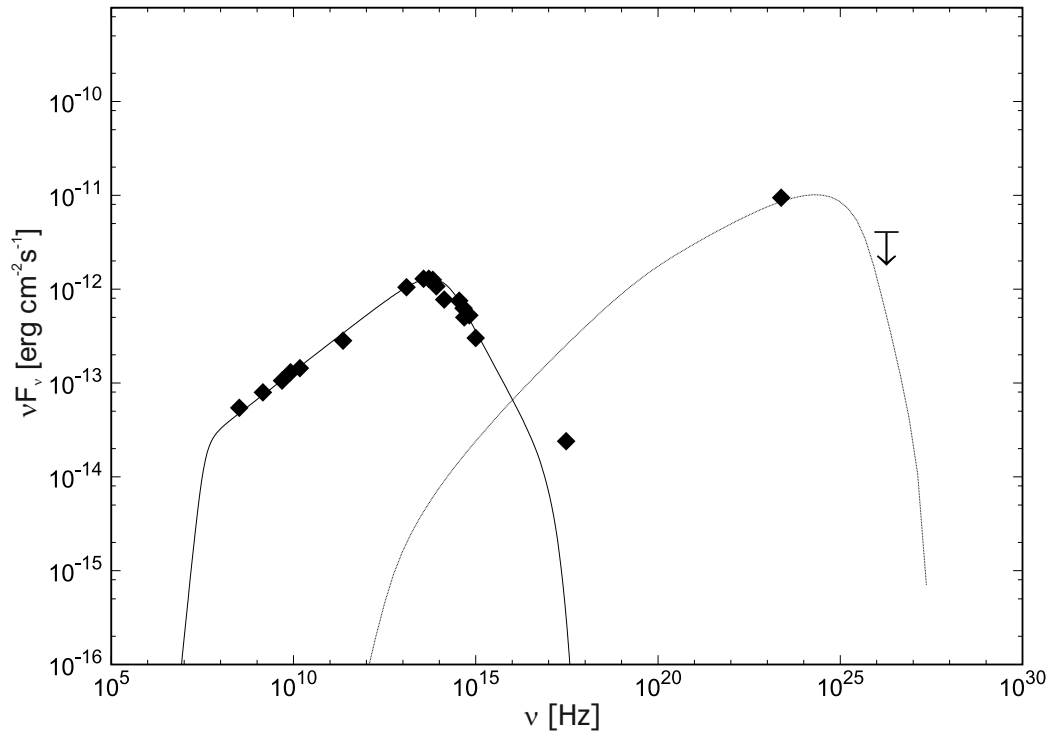


Figure 5.6: SSC fit of Pictor A modified from [51]. Exclusion of X-ray data overpredicts the X-ray flux.

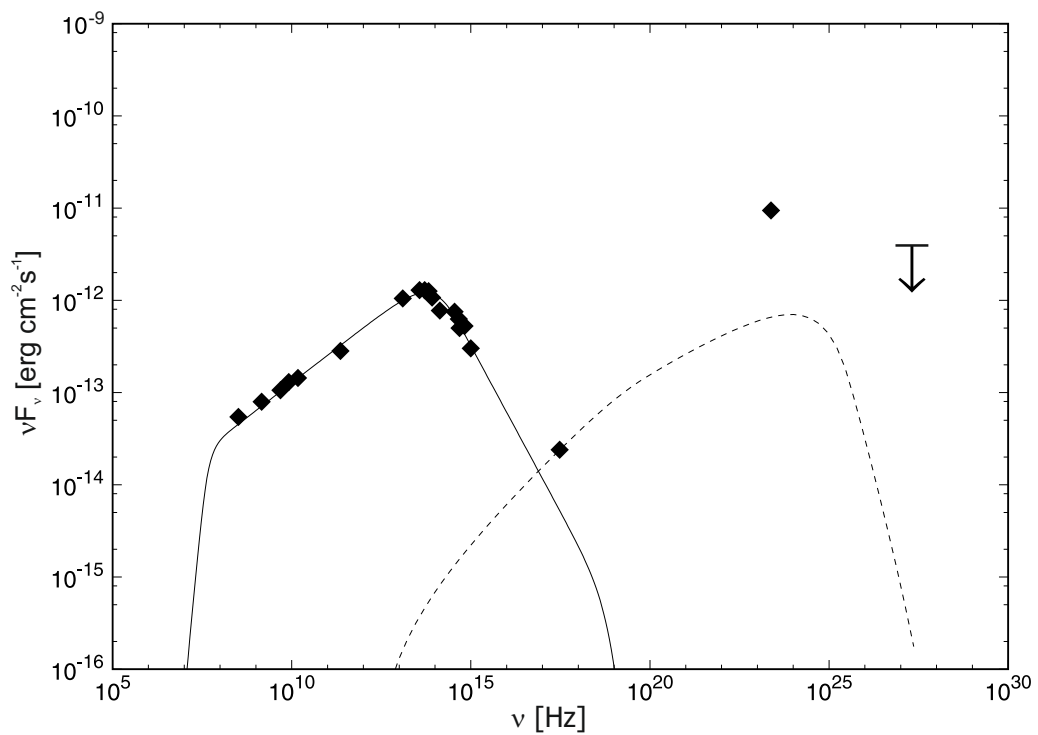


Figure 5.7: SSC fit of Pictor A modified from [51]. Exclusion of γ -ray data underpredicts the γ -ray flux. The X-ray and γ -ray data cannot be simultaneously reconciled.

For the emission of γ -rays to be SSC in origin they cannot be produced in the hot spot region of the radio lobe where the radio to optical and X-ray photons are observed to originate [51]. All the radio to optical data is well described by the process of synchrotron radiation and supports the synchrotron origin of the low emission coming from the WHS. However, the X-ray and γ -ray fluxes cannot be concurrently accounted for by the inverse-Compton part of the one-zone SSC model, i.e. the second peak in a typical SSC spectrum. Additionally, Chandra has found that the X-ray emission appears to originate from the WHS [51]. Thus it is concluded that since the X-ray emission origin is resolved from the WHS, the γ -ray flux cannot also originate from the WHS. In the analysis in this work, the two-zone leptonic and hybrid SSC models are successful in reconciling all the observed data, that is simultaneous Swift-XRT X-ray observations as well as Fermi-LAT γ -ray observations.

5.5 Summary

Pictor A is a recently detected radio galaxy in Fermi-LAT γ -rays, with the potential for future VHE γ -ray studies, therefore included in the sample. Selection and analysis of 4 years of all-sky observations from the continuum of Fermi-LAT data between 200 MeV and 300 GeV has produced a power law SED with three upper limits above 4 sigma. The leptonic and hybrid SSC study of simultaneous optical, ultraviolet and X-ray observations from Swift, plus the Fermi-LAT spectrum, provides a good fit to the data, though the hybrid case exhibits a third host galaxy peak while accounting for the host and fitting the data. Compared to other studies, the two-zone model used here is successful in reconciling the X-ray and γ -rays observations. A future step will be to extend the fits as soon as simultaneous VHE γ -ray observations from Cherenkov telescopes are also available.

Chapter 6

Centaurus A

6.1 Introduction

Centaurus A ($z = 0.001$), is located at a distance of 3.7 Mpc and is the closest radio loud active galaxy to earth [96]. Existing in the giant elliptical host galaxy NGC 5128, it has giant radio lobes which subtend approximately 10° in the north-south direction (Figure 6.1), and is considered a low power radio galaxy [51]. In this chapter, the collection of observed multiwavelength data for Centaurus A will be explained, as well as a widely accepted Fermi-LAT SED from [96]. SSC modeling of the completed SED will then be presented.

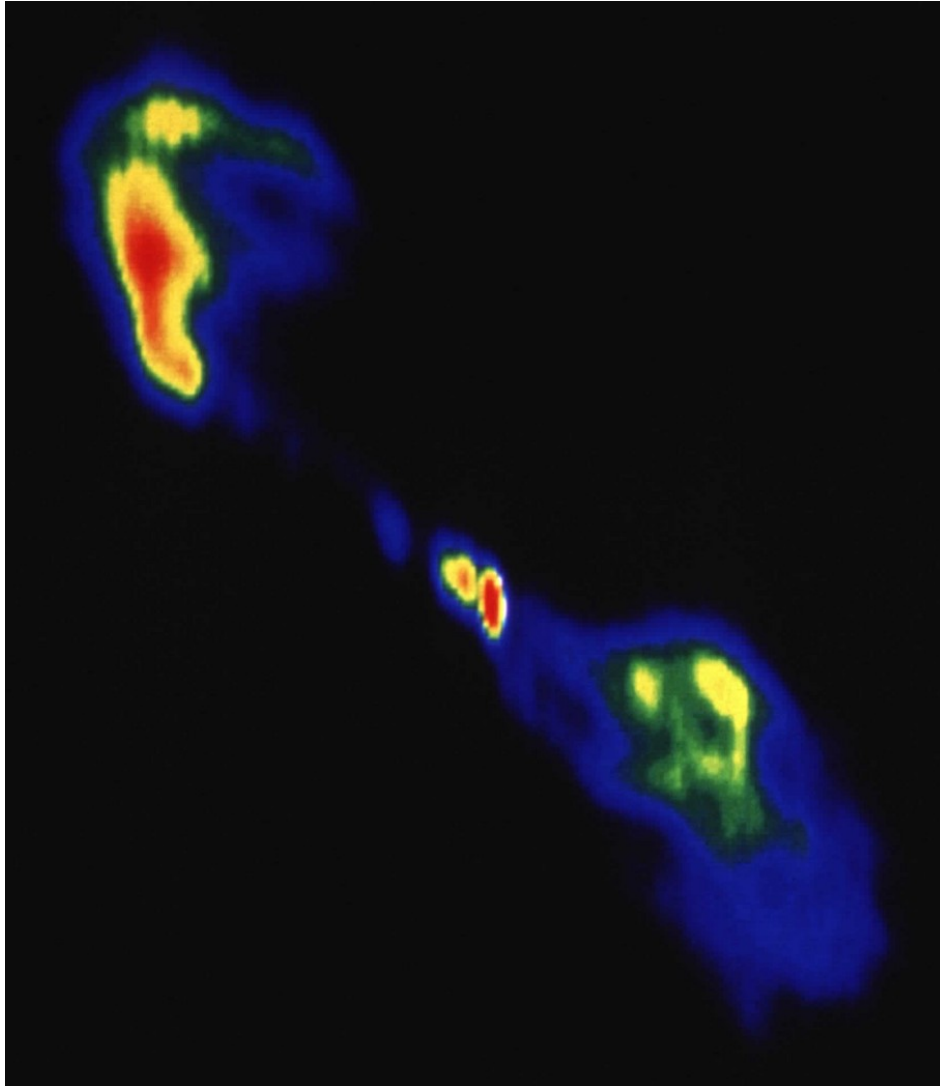


Figure 6.1: Radio image of Centaurus A. Image courtesy of NRAO/AUI.

6.2 Collection of simultaneous multiwavelength data

There exist Swift-XRT observations from January 15 2009 to February 6 2012 and Swift-BAT observations from August 2008 to May 2009, as well as VHE H.E.S.S. data from 2004 to 2008, during which the steady low state emission is not well explained. There is additional data from TANAMI and Suzaku, and archival observations as shown in Figure 6.2.

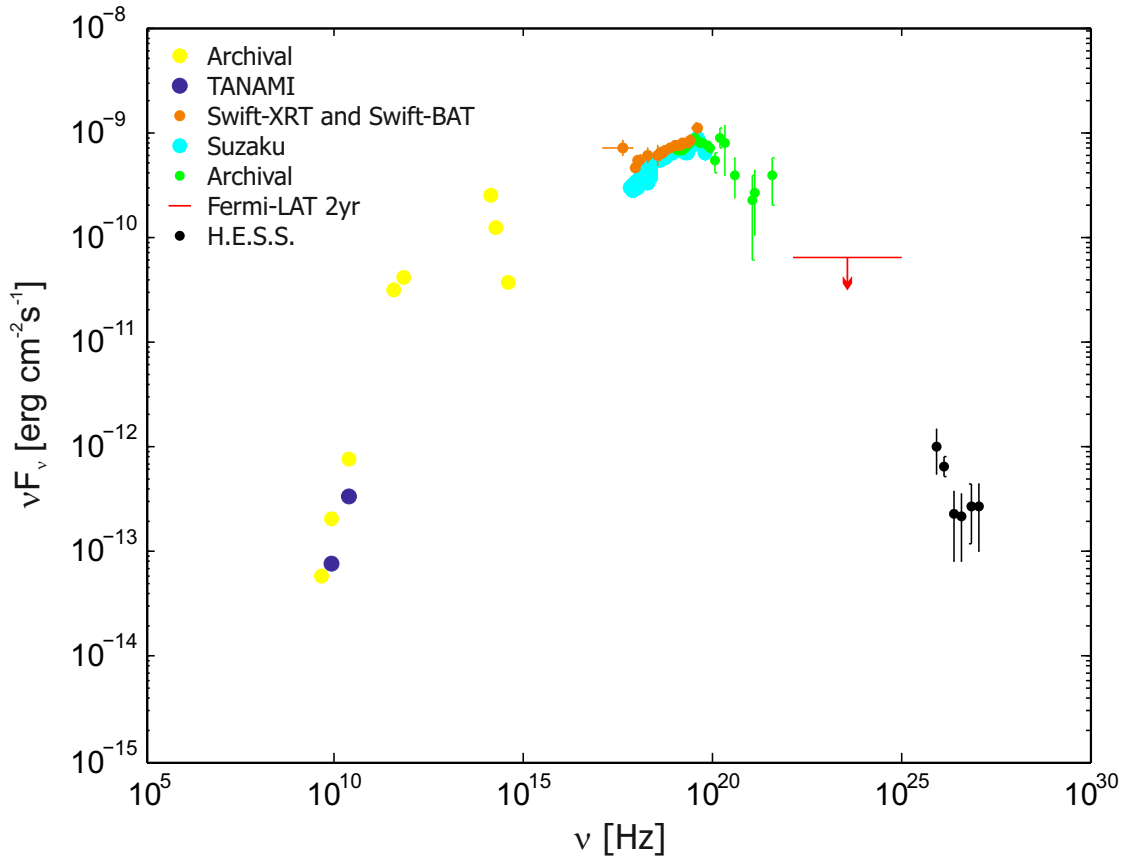


Figure 6.2: Collection of multiwavelength data for Centaurus A. Simultaneous data: Swift-XRT from January 15 2009 to February 6 2012 and Swift-BAT from August 2008 to May 2009 in orange. Nearly simultaneous data: TANAMI data from November 27 and 29 2009 shown in dark blue in the radio epoch. Suzaku measurements from July 20-21, August 5-6 and August 14-16 2009 are shown in cyan in the X-ray epoch. Non-simultaneous data: archival data at low energies in yellow, and at X-ray energies in green [98]. Fermi-LAT 2 year upper limit is shown by the red line, and H.E.S.S. data from 2004 to 2008 in black [99].

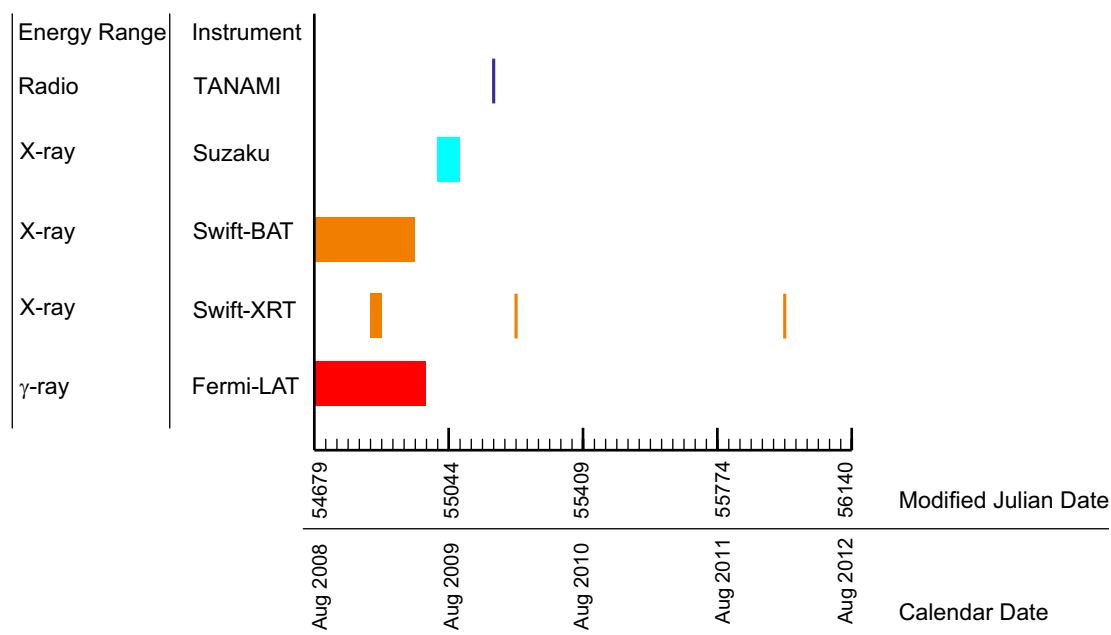


Figure 6.3: Schematic of overlapping observation times for Centaurus A from different instruments in various energy regimes. Suzaku and TANAMI are shown for interest but not used in fitting considerations. All three Swift-XRT observations in orange were necessary to yield a quality set of data points on the multiwavelength spectrum.

6.3 Results of Fermi Large Area Telescope analysis

An analysis was attempted here, to account for the core emission and the lobes, using event class 2 photons from a 20° radius ROI, centred on R.A. = 201.365, Dec = -43.0191. The large radio lobes of Centaurus A make it a very difficult source to analyze, and beyond this step repeated analysis attempts did not converge. The Fermi-LAT spectrum of Centaurus A was therefore taken with permission from the study conducted by [96]. The energy and time selections are 200 MeV to 30 GeV, and August 4 2008 to May 31 2009 (MET 239557420 to 265507200). The power law fit, with a TS value of 378, yielded an integral flux equal to $2.06 \times 10^{-7} \pm 0.20 \times 10^{-7}$ ph/cm²/s between 100 MeV and 30 GeV, with photon spectral index 2.76 ± 0.07 as depicted in Figure 6.4. See details in §A.2.4.

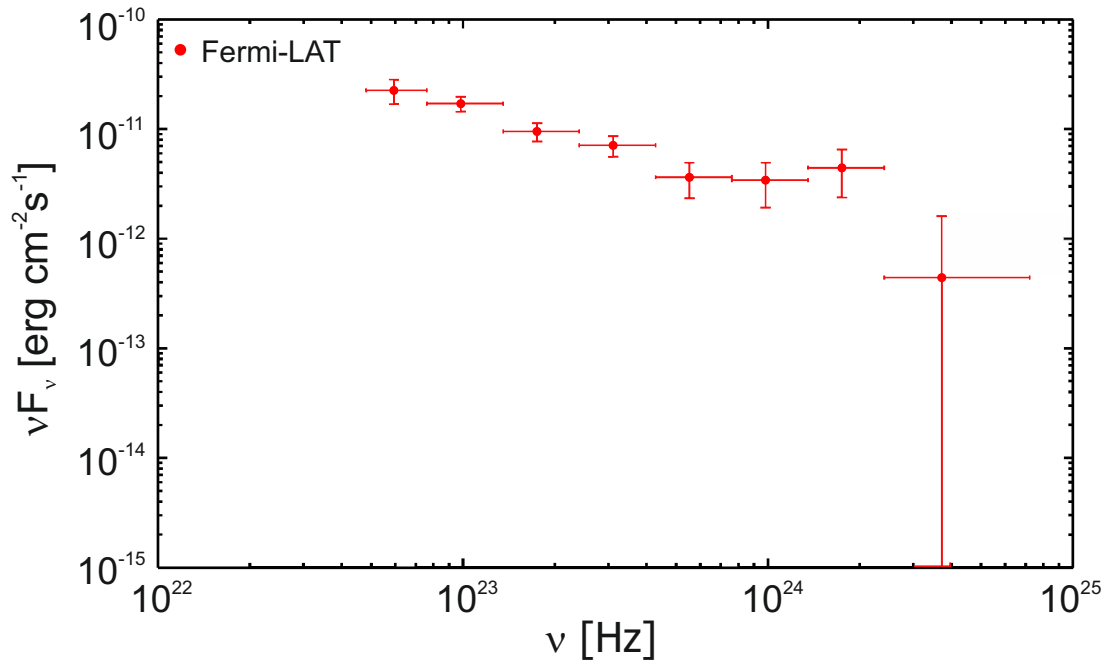


Figure 6.4: Fermi-LAT spectral energy distribution of Centaurus A, containing 8 points over a 10 month time period, modified from [96].

6.4 Results of multiwavelength analysis

Using the assembly of multiwavelength data for Centaurus A as shown in Figure 6.2 as a starting point, the analyzed Fermi-LAT SED of Figure 6.4 is added. This is followed by the two-zone SSC analysis as was done for M 87, NGC 1275, and Pictor A. There exist VHE γ -ray observations from H.E.S.S. from 2004 to 2008, during which the steady low state emission is not well explained, i.e. it is not consistent with the Fermi-LAT extrapolation into higher wavelengths. This makes Centaurus A also an ideal candidate for dark matter model testing as was shown earlier for M87 and NGC 1275, and should be a future step. See Figure 6.5.

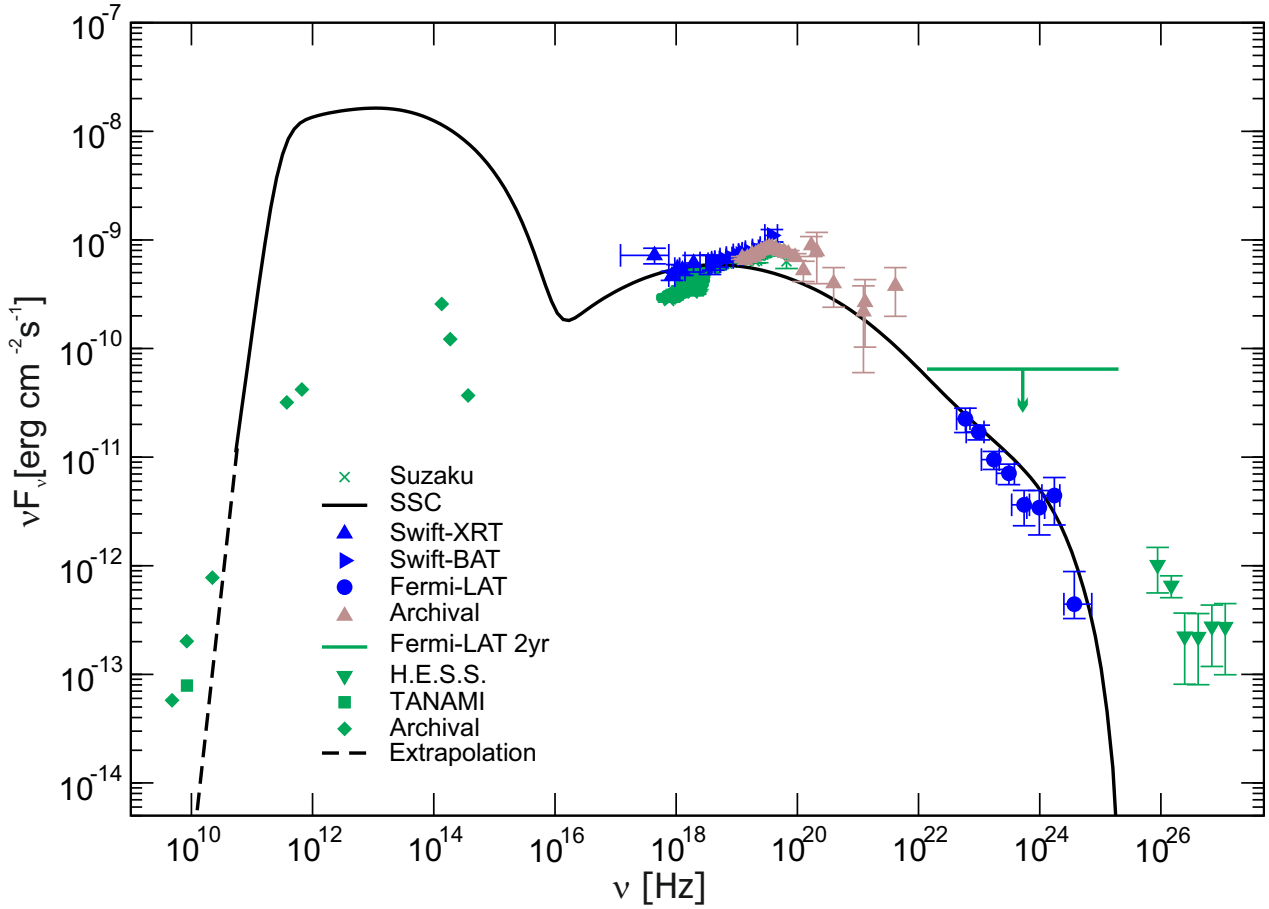


Figure 6.5: SSC fit of Centaurus A. Blue data points are considered in the fitting model, brown data points are used as a reference in the fit, and green data is shown for illustrative purposes.

In the fit, the injected electron number density is $K = 5.5 \times 10^4 \text{ cm}^{-3}$, Lorentz factor is $\Gamma = 50$, and magnetic field in the jet is $B = 0.52 \text{ G}$. The radiation and acceleration zone radii are $R_{rad} = 5.0 \times 10^{15} \text{ cm}$ and $R_{acc} = 5.3 \times 10^{14} \text{ cm}$, with an acceleration to escape timescale ratio of $\frac{t_{acc}}{t_{esc}} = 1.75$, and a Fermi I to Fermi II acceleration ratio of $a = 5 \times 10^3$. The doppler factor is $\delta = 21$.

The SSC model fit is obtained through a simple scaling of the observational angle in the model, which might be too simple to explain the data for this radio galaxy consistently once the archival low energy data is taken into account. Potential for improvement is possible through the hybrid model.

6.4.1 Comparison of results

Abdo et al. 2010 [96] fit multiwavelength data for Centaurus A using 4 models: SSC for all data, SSC model excluding X-rays, SSC fit to the H.E.S.S. data

only (Figure 6.6), and a decelerating jet model [100]. The single-zone SSC model could not reconcile the VHE γ -ray observations with the rest of the data [96]. Furthermore non-simultaneous H.E.S.S. and Fermi-LAT data were used based on the assumption that the H.E.S.S. and Fermi-LAT γ -ray data was not variable. However, they could be variable on longer timescales. [96] also emphasized the importance of simultaneous multiwavelength data.

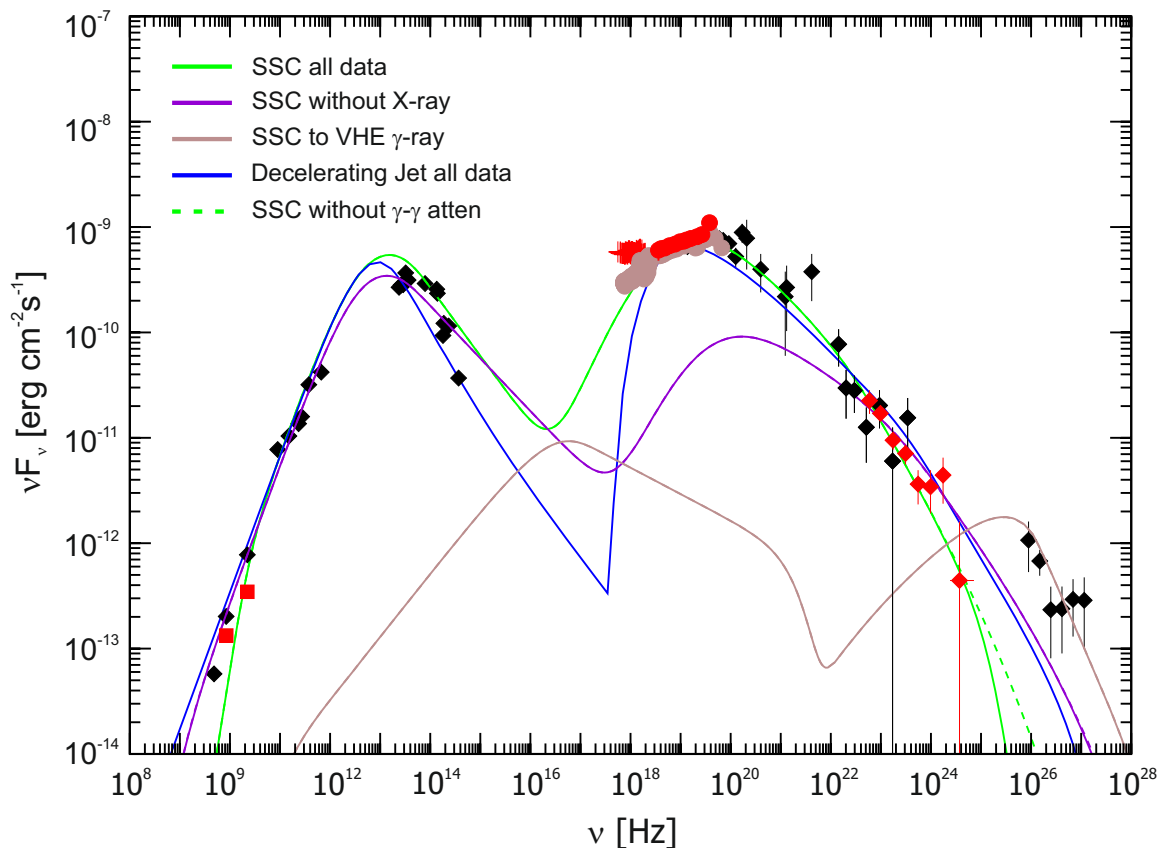


Figure 6.6: Fitting of Centaurus A by [96]. The SSC fit to all available data is shown by the green solid line. The SSC fit to all data excluding X-rays is shown in purple. The fit to the H.E.S.S. data is shown in brown. The decelerating jet model fit is depicted by the blue line. Finally for interest, an SSC fit to all available data excluding γ - γ attenuation is also shown, by the green dashed line.

6.4.2 Other possible origins for VHE γ -ray emission from Centaurus A

Another possible explanation for the VHE γ -ray emission from Centaurus A can be due to the shock front observed in X-rays. There is a shock front located in the southwest inner lobe which can still be considered within the core region, and this can be a source of TeV γ -rays [96]. Centaurus A is a

good candidate for dark matter model testing, as the steady low state emission does not reconcile with the Fermi-LAT extrapolation into higher wavelengths. Further general possibilities are described in §7.2.1.

6.5 Summary

There exist a wealth of archival and current multiwavelength observations for Centaurus A. VHE γ -ray H.E.S.S. observations, Swift-XRT and Swift-BAT measurements, have prompted the analysis of Fermi-LAT γ -ray observations from 2008 to 2009. The clear power law spectrum has 8 data points which have been studied in conjunction with the Swift spectra, using accurate treatment of leptonic interactions from the SSC standpoint. The total spectrum peaks near 10^{13} Hz and 10^{19} Hz. Analysis of Centaurus A with the dark matter model from §2.6 is prioritized as future work.

Chapter 7

Discussion

7.1 Introduction

In this chapter the findings from the dedicated radio galaxy chapters will be reviewed, and other γ -ray emission modalities explored. The selected sample is then extended by looking at a larger population of γ -ray emitting radio galaxies, namely those detected recently in γ -rays by the Fermi-LAT, as well as those that have been detected at radio wavelengths by TANAMI and MOJAVE. The γ -ray luminosities, core radio luminosities, and total radio luminosities are calculated. As will be shown in Table 7.9, there is a significant overlap in the data sets, providing both γ -ray and radio emission information for several sources. An introduction to the luminosity function and its usage in estimating the diffuse γ -ray emission for an extended radio galaxy population is then explained, and the steps in this calculation outlined.

7.2 Spectral energy distributions of radio galaxies

The selected sample of γ -ray detected radio galaxies, M 87, NGC 1275, Pictor A, and Centaurus A, has been surveyed across the electromagnetic spectrum, bringing together observations from radio, optical, ultraviolet, X-ray, γ -ray and VHE γ -ray telescopes. As there is evidence for variability in the sample, simultaneous data has been prioritized and flaring episodes excluded, and Fermi-LAT observations additionally analyzed in simultaneous time ranges to this end. The total SEDs, completed with the Fermi-LAT SEDs, have been examined with an SSC approach, including accurate treatment

of synchrotron and inverse-Compton emission processes. It is found that the two-zone SSC model is able to well explain all the radio galaxies in the sample. Acceleration and radiation zone radii range between 10^{13} - 10^{15} cm and 10^{15} - 10^{16} cm, respectively; with the acceleration zone radius 1 to 2 orders of magnitude smaller than R_{rad} . The escape timescale ratios were consistent in each case, whether leptonic or hybrid, falling between $\frac{t_{acc}}{t_{esc}} = 1.11$ and $\frac{t_{acc}}{t_{esc}} = 1.75$. The Lorentz factors in the leptonic and hadronic cases are shown to cover the range $\Gamma = 15$ to $\Gamma = 65$, with a leptonic doppler factor range of $\delta = 14.5$ to $\delta = 32.5$. The leptonic-hadronic hybrid case also provides a reasonable fit to the data, with a slightly lower doppler factor ($\delta = 11$). The magnetic field strength is consistent for the entire sample in the leptonic case, between $B = 0.24$ G and $B = 0.52$ G, though much higher for the hybrid case ($B = 18$ G). The entire sample demonstrates the double-hump spectral signature. The choice of model and all fit parameters for each multiwavelength analysis are outlined in Table 7.1.

Table 7.1: Fit parameters for multiwavelength spectral energy distributions. Pictor A is fit with both the leptonic SSC and hybrid models, which take into account electrons and electrons with protons respectively, with two additional parameters in the hybrid fit: The proton number density K_p [cm^{-3}] = 1.9×10^{11} and the proton Lorentz factor $\Gamma_p = 10$. K = the injected electron number density, B = the magnetic field, R_{rad} = the radiation zone/blob radius, R_{acc} = the acceleration zone/blob radius, $\frac{t_{acc}}{t_{esc}}$ = the ratio of the acceleration timescale to the escape timescale, a = the ratio of Fermi I to Fermi II acceleration, δ = the doppler factor.

Radio Galaxy	Model	K [cm^{-3}]	Γ	B [G]	R_{rad} [cm]	R_{acc} [cm]	$\frac{t_{acc}}{t_{esc}}$	a	δ
NGC 1275	SSC	1.9×10^6	15	0.28	2.5×10^{15}	3.5×10^{14}	1.40	150	32.5
Pic A	SSC	2.5×10^5	65	0.47	2.95×10^{16}	1.77×10^{15}	1.11	100	21
M 87	SSC	1.9×10^6	10	0.24	6.0×10^{15}	1.0×10^{14}	1.43	20	14.5
Cen A	SSC	5.5×10^4	50	0.52	5.0×10^{15}	5.3×10^{14}	1.75	5×10^3	21
Pic A	Hyb	8.6×10^9	30	18	7.25×10^{16}	3.65×10^{13}	1.19	50	11

7.2.1 Other explanations for VHE γ -ray emission

If not an SSC scenario, there are other possible explanations for the very high energy emission of γ -rays from radio galaxies. The following theories attempt to account for this while excluding dark matter annihilation.

7.2.1.1 Multiple zone SSC

The use of multiple emission zones moving at different angles to the line-of-sight has been attempted by [101] for M 87 and Centaurus A. In the case of Centaurus A, a second zone works, and does not over-produce the data [96]. In the model used in this work, both zones move at the same angle.

7.2.1.2 Isotropic halo of electrons in the Interstellar Medium

Electron-positron pairs can be created by absorbed γ -rays which in turn create an isotropic halo of electrons in the Interstellar Medium (ISM). These electrons Compton scatter starlight from the host galaxy, resulting in isotropic γ -rays [102].

7.2.1.3 PeV neutrinos and UHECRs

The IceCube Neutrino Observatory (IceCube) on the South Pole, detects neutrinos by observing Cherenkov emission produced in ice when incident neutrinos interact with charged particles. Astrophysical objects including AGN are thought to produce high energy neutrinos when charged pions, produced through the interactions between gas, radiation, and cosmic rays, decay. The resulting neutrinos can reach energies of up to 5% that of the original cosmic ray nucleons. For more information, see the 'Big Bird' results from IceCube in [103]. Ultra high energy cosmic rays have been detected at energies as high as 10^{18} eV to 10^{20} eV, i.e. on the scale of EeV energies, and it is considered likely that these UHECRs are produced in conjunction with ultra high energy neutrinos (UHE ν s) [104]. Evidence for deposited neutrino energies between 30 TeV and 2 PeV has been confirmed by 3 years of data collected

between 2010 and 2013, with so far the 2 PeV event being the highest energy neutrino detected in history [103]. Since neutrinos point directly to their sources, traveling large distances without being affected by magnetic deflection or absorption [103], [104], detection of UHE ν s lends insight into the origin of cosmic rays [103].

7.3 Dark matter annihilation in radio galaxies

M 87 and NGC 1275 were analyzed for dark matter neutralino annihilation. In the case of M 87 the SED used for dark matter analysis was not simultaneous, but represented the low or steady-state spectrum. The NGC 1275 SED used for dark matter analysis was simultaneous. For M 87 the SSC fit alone could not account for the observations in the very high energy regime, which coincided with the currently accepted mass/energy range for self-annihilating neutralinos. The SSC and dark matter combined fit explained the data well. The dark matter model generated a neutral pion emission spectrum and an inverse-Compton emission spectrum, another double-hump signature, resulting from the decay of neutralinos. The neutralino mass m_χ was determined to be 4.747 TeV, and the boost factor which accounts for clumping within the dark matter halo, f , was determined to be 812 [70]. The combined model marginally improved the fit to the data set as compared to the SSC fit alone, and explained the excess in the very high energy regime as emission originating from dark matter annihilation. The same technique was applied to NGC 1275, which revealed a neutralino mass of $m_\chi = 4.793$ TeV and boost factor $f = 141$, coinciding with the predicted dark matter mass range of ~ 1 GeV to ~ 10 TeV [6].

This result is quite promising and seems to confirm the approximate value of the neutralino mass in both AGN. Reasons for caution would include the following. There could be multiple radiation mechanisms at play such as secondary inverse-Compton radiation which could produce a third peak in Figure 4.10, or contributions from other emission channels. Emission due to any mechanism that is captured in the observational data and SSC fit of NGC 1275 could potentially contaminate the dark matter calculations, and every new feature appearing on the plot should not immediately be taken as dark matter.

In both studies, the improvement was too small to claim an exact discovery, though it suggests that dark matter characteristics may be revealed through multiwavelength methods, and future low emission states can increase the likelihood of detection when using a combined model, since the SSC component is vulnerable to variability while the dark matter component should remain steady with respect to time. Quantities such as the neutralino mass, boost factor, and annihilation cross-section could be extracted by measuring the double-hump structure of the dark matter model. Nevertheless, the similarity in the results of M 87 and NGC 1275 is worth noting.

7.3.1 Future dark matter work

The above dark matter analyses were conducted numerically and successfully converged for M 87 and NGC 1275. However results of the same modeling technique for Centaurus A and Pictor A were inconclusive because the numerical program could not converge on values for m_χ and f . There are no obvious reasons for the malfunction, and it is thought to be due to limited computing power. It is recommended for future dark matter studies that the SSC SEDs of Centaurus A and Pictor A be used as a starting point for extracting quantitative dark matter parameters. These plots hold the twofold advantage of being constructed from simultaneous data, and following consistent SSC fitting methods.

It is considered that there exists no numerous population of γ -ray emitting sources within dwarf spheroidal galaxies, though they are heavily dominated by dark matter [105]. Therefore multiwavelength observation, SSC analysis, and dark matter analysis are recommended for AGN existing in dwarf spheroidal galaxies, and lower error margins expected due to the lack of contamination.

7.4 Calculation of γ -ray luminosities

The Fermi-LAT has detected 21 classes of objects emitting in γ -rays over four years of total data collection [52], which include starburst galaxies, binaries, normal galaxies, novae, and supernova remnants. The first 24 months of data has been opened for access as the 2FGL Catalog [50], from which raw data has been selected for analysis in this work. This has recently been

extended to 48 months in the 3FGL Catalog [52]. In this section, the γ -ray luminosities of the radio galaxies detected in the 48 month data release will be calculated, and used later for a correlation study. See Table 7.2.

Table 7.2: γ -ray emitting radio galaxies detected by the Fermi Large Area Telescope after 48 months of operation. $S_\gamma(\epsilon_1, \epsilon_2)$ is the energy flux between 100 MeV and 100 GeV, and Γ is the photon number power law index between 100 MeV and 100 GeV [50], [106]. $\Gamma_{avg} \approx 2.18$. Right ascension and declination are given in degrees in Equatorial J2000.0 coordinates [52].

Common Name	Fermi Name	z	FRI/II	R.A.	Dec	$S_\gamma(\epsilon_1, \epsilon_2)$ [10^{-12} erg/cm ² /s]	Γ
NGC 1275	J0319.8 +4130	0.018	I	49.959	41.514	199.1 ± 3.9	2.08
Pictor A	J0519.2 -4542	0.035	II	80.17	-45.61	4.68 ± 1.2	2.49 ± 0.18
M 87	J1230.8 +1224	0.004	I	187.701	12.406	14.52 ± 1.3	2.04 ± 0.07
Cen A Core	J1325.6 -4300	0.001	I	201.367	-43.030	66.5 ± 2.1	2.70 ± 0.03
IC 310	J0316.6 +4119	0.019	I	49.169	41.322	7.58 ± 1.5	1.90 ± 0.14
OH -342	J0627.1 -3528	0.055	I	96.777	-35.479	16.87 ± 1.6	1.87 ± 0.06
NGC 1218	J0308.6 +0408	0.029	I	47.109	4.111	6.59 ± 1.1	2.07 ± 0.11
NGC 2484	J0758.7 +3747	0.043	I	119.617	37.787	2.82 \pm 0.7	2.16 ± 0.16
NGC 6251	J1629.4 +8236	0.025	I	247.355	82.614	10.95 ± 0.9	2.04 ± 0.08
3C 111	J0418.5 +3813c	0.049	II	64.589	38.027	16.26 ± 1.5	2.79 ± 0.08
3C 264	J1145.1 +1935	0.022	I	176.271	19.606	2.97 ± 0.7	1.98 ± 0.20
3C 303	J1442.6 +5156	0.141	II	220.762	52.027	2.19 ± 0.6	1.91 ± 0.18
4C +39.12	J0334.2 +3915	0.021	LPC	53.577	39.357	4.18 ± 1.0	2.11 ± 0.17
Fornax A	J0322.5 -3721	0.006	I	50.643	-37.358	5.30 ± 0.8	2.20 ± 0.11
Centaurus B	J1346.6 -6027	0.013	I	206.663	-60.466	24.92 ± 3.0	2.32 ± 0.09

In Table 7.2 11 objects are FRI, 3 are FRII and one is a low power compact source. The average photon number power law index is found to be $\Gamma_{avg} \approx 2.18$.

The energy fluxes $S_\gamma(\epsilon_1, \epsilon_2)$ between ϵ_1 and ϵ_2 can be determined from the photon fluxes [10]:

$$S_\gamma(\epsilon_1, \epsilon_2) = \int_{\epsilon_1}^{\epsilon_2} \epsilon \frac{dN}{d\epsilon} d\epsilon \quad (7.1)$$

where the γ -ray spectrum $\frac{dN}{d\epsilon}$ is most often a power law distribution [10].

The γ -ray luminosity is dependent on the luminosity distance at the redshift z , the energy flux $S_\gamma(\epsilon_1, \epsilon_2)$, and the photon number power law index Γ [10],

$$L_\gamma(\epsilon_1, \epsilon_2) = 4\pi d_L^2(z) \frac{S_\gamma(\epsilon_1, \epsilon_2)}{(1+z)^{2-\Gamma}} \quad (7.2)$$

The luminosity distance is calculated using the cosmological parameters and redshift as derived in §B.1, resulting in the γ -ray luminosity estimates listed in Table 7.3. The calculation table can be found in §B.4.

$$d_L = \frac{300000}{70} \frac{2}{0.0729} \left(1.73 + (0.27)z - (1.73)\sqrt{1 + (0.27)z} \right) \quad (7.3)$$

Table 7.3: γ -ray luminosity and luminosity distance estimates for the population of γ -ray emitting radio galaxies detected by Fermi using Table 7.2, equation 7.2 and equation 7.3, after 48 months of operation. For details, refer to §B.4.

Radio Galaxy	d_L [cm]	L_γ [erg/s]
NGC 1275	2.399×10^{26}	1.442×10^{44}
Pictor A	4.698×10^{26}	1.320×10^{43}
M 87	5.299×10^{25}	5.124×10^{41}
Cen A Core	1.323×10^{25}	1.464×10^{41}
IC 310	2.533×10^{26}	6.101×10^{42}
OH -342	7.445×10^{26}	1.167×10^{44}
NGC 1218	3.883×10^{26}	1.251×10^{43}
NGC 2484	5.792×10^{26}	1.197×10^{43}
NGC 6251	3.342×10^{26}	1.538×10^{43}
3C 111	6.616×10^{26}	9.289×10^{43}
3C 264	2.937×10^{26}	3.218×10^{42}
3C 303	1.976×10^{27}	1.062×10^{44}
4C +39.12	2.802×10^{26}	4.134×10^{42}
Fornax A	7.955×10^{25}	4.220×10^{41}
Cen B	1.729×10^{26}	9.398×10^{42}

7.5 Collection of core radio data

In parallel to the assembling of simultaneous multiwavelength data of radio galaxies in §3 through to §6, radio measurements of signals emanating specifically from the core regions of γ -ray emitting radio galaxies were also collected. This section will describe this type of data.

As the jets, lobes, and core regions of radio galaxies are distinct, two new spectral indices are defined; $\alpha_{R,core}$, the core radio spectral index, and $\alpha_{R,total}$,

the total radio spectral index. Given a frequency ν in GHz, the radio fluxes are defined as $S_{R,core}(\nu)$, the core radio flux, and $S_{R,total}(\nu)$, the total radio flux.

Table 7.4 lists radio emission data from the TANAMI program [107], introduced in §2.2.2. For the analysis, circular and/or elliptical Gaussian components were used to fit the data using the software DIFMAP [108]. The fit parameters were the flux density, the size of the component (minor and major axes), and the position, resulting in a model for the spatial flux density distribution of the radio galaxy [109].

Pictor A, also known as Source 0518-458, was imaged by [110] and model fit by [109]. The derived model for Centaurus A was further constrained by other observations, and imaged and model fit by [111]. OH -342, also known as Source 0625-354, was also further constrained by other observations and imaged and model fit by [112] in four different epochs; in each case, the most recent epochs will be used in further sections.

Table 7.4: Radio core emission from TANAMI.

Source	Epoch	ν [GHz]	$S_{R,core}(\nu)$ [mJy]
Pictor A	Nov 27 2008	8.441	571.8 ± 57.18
	Nov 29 2008	22.316	541.0 ± 54.1
Centaurus A	Nov 27 2008	8.441	493.0 ± 49.3
	Nov 29 2008	22.316	1620.0 ± 162.0
OH -342 (Trial 1)	Feb 07 2008	8.441	368.0 ± 36.8
	Feb 6 2008	22.316	235.0 ± 23.5
OH -342 (Trial 2)	Nov 27 2008	8.441	342.0 ± 34.2
	Nov 29 2008	22.316	209.0 ± 20.9

The core radio spectral index can be calculated using $S_{R,core}(\nu)$ and ν for the two measurements of each source. Given a power law spectral energy distribution,

$$S(\nu) = \nu^\alpha \quad (7.4)$$

$$\alpha = \frac{\log \frac{S(\nu_1)}{S(\nu_2)}}{\log \frac{\nu_1}{\nu_2}}. \quad (7.5)$$

The calculation of each $\alpha_{R,core}$ value as well as its error is shown in §B.2. These results are listed in Table 7.5.

Table 7.5: Derived core radio spectral indices for TANAMI sources.

Source	$\alpha_{R,core}$
	(8.441 GHz - 22.316 GHz)
Pictor A	-0.06 ± 0.15
Centaurus A	1.22 ± 0.15
OH -342 (Trial 2)	-0.51 ± 0.15

The MOJAVE program introduced in §2.2.1 has published milliarcsecond-scale spectral index distributions for 190 extragalactic radio jets [113], ranging from quasars to BL Lac objects and active galaxies. The sources were observed at frequencies of 8.1 GHz, 8.4 GHz, 12.1 GHz, and 15.4 GHz in 2006, with spectral index maps determined between 8.1 GHz and 15.4 GHz. Preliminary spectral index estimates before the publication of [113] were available for the core and increasingly farther components away from the core. Fluxes are found in [114]. Note that 3C 380 is currently classified as a steep-spectrum radio quasar (SSRQ) rather than a radio galaxy, and will be excluded from further analysis. See Table 7.6.

Table 7.6: Core radio emission from MOJAVE from [113] (preliminary) and [114].

Source	Epoch	$S_{R,core}$ [Jy] (15.4 GHz)	$\alpha_{R,core}$ (8.1 GHz - 15.4 GHz)
NGC 1275	Sept 06 2006	1.380	0.48 ± 0.10
M 87	June 15 2006	1.408	0.24 ± 0.10
NGC 6251	March 09 2006	0.664	0.65 ± 0.10
3C 380	Aug 09 2006	1.358	0.61 ± 0.10

Table 7.7 combines this TANAMI and MOJAVE core information with total radio data from a large range of literature, as collected in [10] and listed in 7.8. Radio measurements must be compared at the same frequency; hence TANAMI fluxes are translated from 8.441 GHz and 22.316 GHz to 5 GHz as shown in §B.3. Similarly MOJAVE core fluxes and spectral indices are translated from 15.4 GHz to 5 GHz using equation 7.4.

Table 7.7: Collection of core and total radio data for radio galaxies detected in γ -ray and radio regimes. Sources of data are listed in Table 7.8. The total radio energy flux for Fornax A is not known to a higher degree of precision than shown.

Radio Galaxy	$\alpha_{R,core}$	$\alpha_{R,tot}$	$S_{R,core}$ (5GHz) [Jy]	$S_{R,tot}$ (5GHz) [Jy]
NGC 1275	0.48 ± 0.10	0.78	0.804	high variability
Pictor A	-0.06 ± 0.15	1.07	0.592	15.45 ± 0.47
M 87	0.24 ± 0.10	0.79	1.075	71.566 ± 0.993
Cen A Core	1.22 ± 0.15	0.70	0.261	62.837 ± 0.099
IC 310	-	0.75	-	0.258 ± 0.031
OH -342	-0.51 ± 0.15	0.65	0.448	2.25 ± 0.09
NGC 1218	0	0.64	0.964 ± 0.164	3.40 ± 0.11
NGC 6251	0.65 ± 0.10	0.72	0.320	0.510 ± 0.050
3C 111	-0.20	0.73	1.14	6.637 ± 0.996
Fornax A	0.50	0.52	0.051	72
Cen B	0	0.13	2.730	6.58 ± 1.04

Table 7.8: Sources of data corresponding to Table 7.7.

Column	Data
$\alpha_{R,core}$	Core radio spectral index. Pictor A, Centaurus A, and OH -342 from TANAMI observations (Table 7.4, 7.5 and §B.2). NGC 1275, M87, and NGC 6251 from MOJAVE observations in Table 7.6. Fornax A from [115]. 3C 111 and Centaurus B from [10].
$\alpha_{R,tot}$	Total radio spectral index. Pictor A, NGC 1218, and Fornax A from reference [116]. Centaurus A from [117], OH -342 from [118]. NGC 1275, 3C 111, and 3C 207 from [119]. M87, NGC 6251, and Centaurus B from [10]. IC 310 from [120].
$S_{R,core}$	Core radio energy flux at 5 GHz in Jy. Pictor A, Centaurus A, and OH -342 core fluxes observed by TANAMI at 8.441 GHz and 22.316 GHz as listed in Table 7.4, and extrapolated to 5 GHz as shown in §B.3. NGC 1275, M87, and NGC 6251 fluxes observed by MOJAVE at 15.4 GHz as listed in Table 7.6, and extrapolated to 5 GHz as shown in §B.3. Fornax A from [115], NGC 1218, 3C 111, and Centaurus B from [10].
$S_{R,tot}$	Total radio energy flux at 5 GHz in Jy. Pictor A and OH -342 are from [121], remainder of sources from [10].

7.6 Calculation of core and total radio luminosities

Here the radio luminosities of the aforementioned core and total data will be calculated, and used for a correlation study in §7.7.

The radio luminosity is dependent on the luminosity distance $d_L(z)$, radio spectral index α_R , and radio energy flux $S_R(\nu)$ of a source [10]:

$$L_R(\nu) = 4\pi d_L^2(z) \frac{S_R(\nu)}{(1+z)^{1-\alpha_R}} \quad (7.6)$$

α_R may be the radio core spectral index $\alpha_{R,core}$, or the radio total spectral index $\alpha_{R,tot}$. Analogously, the radio energy flux $S_R(\nu)$ may be $S_{R,core}(\nu)$ or $S_{R,tot}(\nu)$, yielding either $L_{R,core}(\nu)$ or $L_{R,tot}(\nu)$.

In Table 7.9, estimates of the luminosities are calculated, using the data found in Table 7.7. L_γ values are repeated for comparison. The calculation tables can be found in §B.4.

Table 7.9: Calculated estimates of the core radio, total radio, and γ -ray luminosities for the population of radio galaxies detected by the 48 month Fermi-LAT all-sky survey. There are 9 radio galaxies for which all values have been determined. For details, refer to §B.

Radio Galaxy	d_L [cm]	$L_{R,core}$ [erg/s]	$L_{R,tot}$ (5GHz) [erg/s]	L_γ [erg/s]
NGC 1275	2.399×10^{26}	2.880×10^{40}		1.442×10^{44}
Pictor A	4.698×10^{26}	7.917×10^{40}	2.145×10^{42}	1.320×10^{43}
M 87	5.299×10^{25}	1.891×10^{39}	1.262×10^{41}	5.124×10^{41}
Cen A Core	1.323×10^{25}	2.871×10^{37}	6.909×10^{39}	1.464×10^{41}
IC 310	2.533×10^{26}		1.035×10^{40}	6.101×10^{42}
OH -342	7.445×10^{26}	1.439×10^{41}	7.691×10^{41}	1.167×10^{44}
NGC 1218	3.883×10^{26}	8.875×10^{40}	3.188×10^{41}	1.251×10^{43}
NGC 2484	5.792×10^{26}			1.197×10^{43}
NGC 6251	3.342×10^{26}	2.226×10^{40}	3.554×10^{40}	1.538×10^{43}
3C 111	6.616×10^{26}	2.961×10^{41}	1.802×10^{42}	9.289×10^{43}
3C 264	2.937×10^{26}			3.218×10^{42}
3C 303	1.976×10^{27}			1.062×10^{44}
4C +39.12	2.802×10^{26}			4.134×10^{42}
Fornax A	7.955×10^{25}	2.022×10^{38}	2.855×10^{41}	4.220×10^{41}
Cen B	1.729×10^{26}	5.061×10^{40}	1.222×10^{41}	9.398×10^{42}

7.7 Luminosity function and the isotropic γ -ray background

The existence of an isotropic γ -ray background everywhere in the universe has been established. The luminosity function (LF) is a metric for different populations of sources, and the first step in determining a percent contribution to the IGRB. In this section, correlation coefficients between radio and γ -ray luminosities of Fermi-detected sources will be determined, and some of the steps toward the γ -ray luminosity function explored. The exact γ -ray

luminosity function and percent contribution of γ -ray emitting radio galaxies to the IGRB will not be calculated as they are outside the scope of this work.

The luminosity function of a population of sources is the number of sources per unit luminosity bin, per unit comoving volume:

$$\Phi(L, z) = \frac{dN(L, z)}{dVdL} \quad (7.7)$$

Where $\Phi(L, z)$ is equal to the number of sources that have luminosity between L and $L + dL$, inside the comoving volume dV . The LF can be computed following two methods. The first is from first principles, as a counting exercise, where the source luminosities are sorted into bins and summed to produce each Φ value, and fit to a power law distribution. Since radio catalogs are generally accurate and vast in their collection of source information, such derivations of the LF from radio data are widely accepted. However in higher energy regimes such as in X-rays or γ -rays, the statistics of available data is much lower and a reliable estimate of the LF cannot be procured through counting.

If it can be determined that the luminosity of a source in one waveband is linearly related to the luminosity of the source in another waveband, then it may be assumed that the LF in one waveband also correlates to the LF in the other waveband [10]. This brings us to the second method for calculating the LF, in this case the γ -ray luminosity function (GLF). Given the increased statistics of core and total radio data (§7.5), the radio luminosity function (RLF) can be determined and then appropriately scaled to provide a reasonable estimation of the γ -ray luminosity function. Given the radio and γ -ray luminosities, L_R and L_γ , respectively:

$$\frac{dN}{dVdL_R} \Rightarrow \frac{dN}{dVdL_\gamma} \quad (7.8)$$

Having access to core radio, total radio, and γ -ray luminosity data for a population of sources, as in Table 7.9 for radio galaxies, provides the foundation for computing L_γ . As the transformation is not straightforward, an efficient approach is suggested in the following table.

Table 7.10: Steps in calculating the γ -ray luminosity function of the population and its diffuse emission. Adapted from [10].

Step	Description
1	Correlation between core radio luminosity $L_{R,core}$ and γ -ray luminosity L_γ
2	Selection of a reliable total radio luminosity function $\Phi_{R,tot}(L, z)$
3	Transformation of radio luminosity function frequency
4	Transformation of radio luminosity function cosmology
5	Selection of a reliable core radio luminosity function $\Phi_{R,core}(L, z)$
6	Correlation between core radio luminosity $L_{R,core}$ and total radio luminosity $L_{R,tot}$
7	Calculation of γ -ray luminosity function $\Phi_\gamma(L_\gamma, z)$ of the population
8	Calculation of diffuse γ -ray emission $S_\gamma(> 100\text{MeV})$ of the extended population

7.7.1 Correlation between core radio luminosity and γ -ray luminosity

A linear relation can be determined by plotting the observed core radio luminosities $L_{R,core}$ against the γ -ray luminosities L_γ from Table 7.9 as in Figure 7.1:

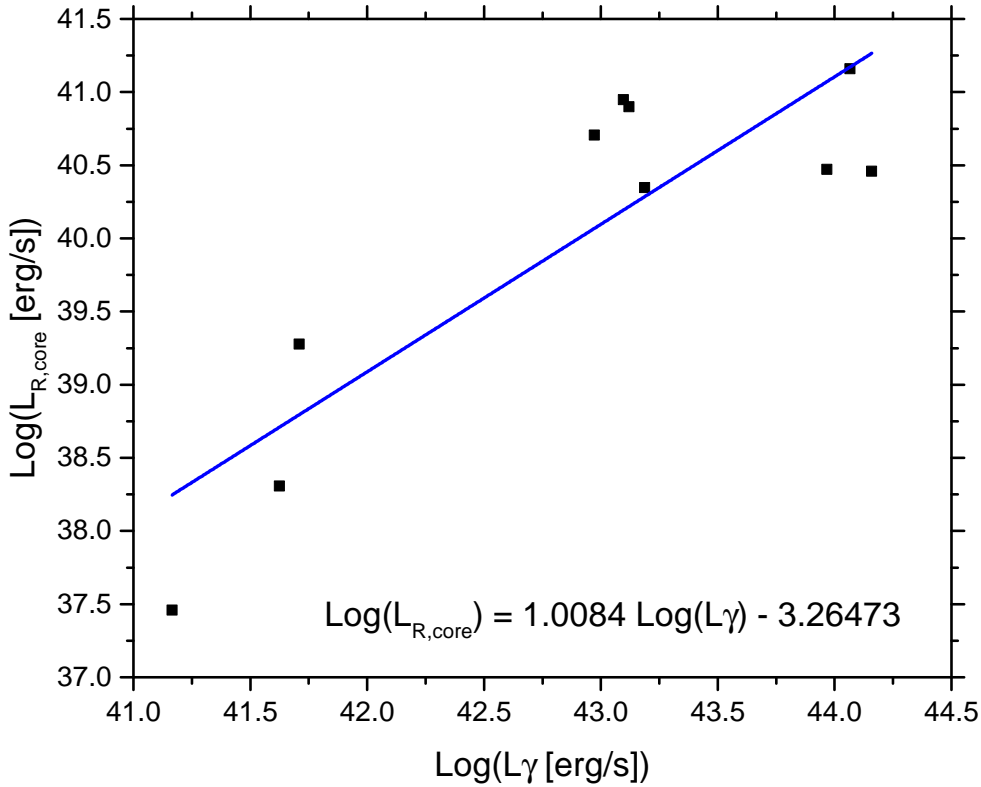


Figure 7.1: Plot of the core radio luminosity $\log L_{R,core}$ versus the γ -ray luminosity $\log L_{\gamma}$ for the population of radio galaxies detected by the 48 month Fermi-LAT all-sky survey. Data is from Tables 7.9, B.1, and B.2.

The slope is found to be $\frac{d\log L_{R,core}}{d\log L_{\gamma}} \cong 1.008$. Calculation details can be found in §B.4.

7.7.2 Selection of a reliable total radio luminosity function

The total radio luminosity function is designated as $\Phi_{R,tot}(L, z)$. The 2001 study by Chris J. Willott et al. [122] provides excellent coverage of 356 sources by combining the low frequency 3CRR, 6CE and 7CRS surveys. The luminosity-redshift plane is shown in Figure 7.2:

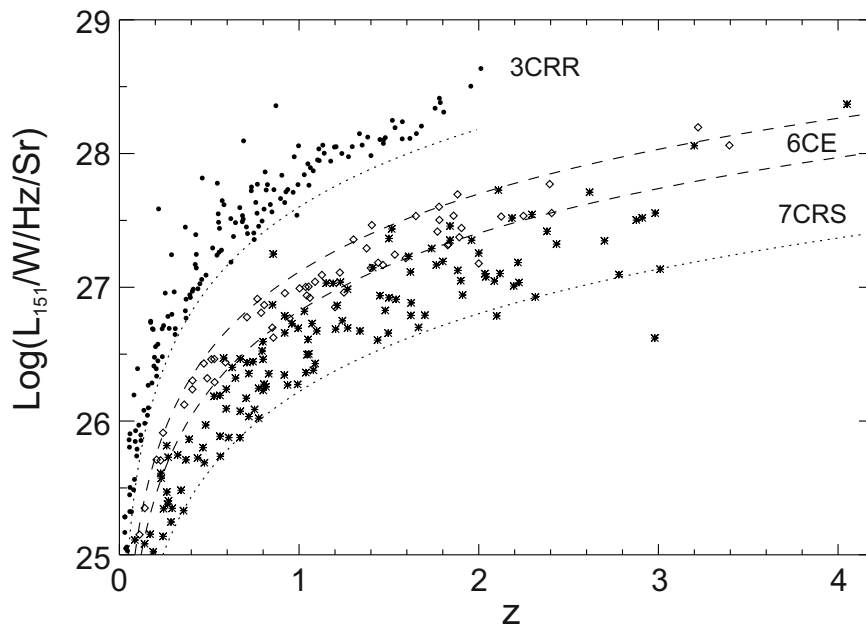


Figure 7.2: Redshift space for 356 low frequency sources listed in the 3CRR, 6CE and 7CRS samples. Image modified from [122].

The radio fluxes and luminosities are detected at 151 MHz and 178 MHz, and a radio luminosity function calculated at 151 MHz. Although mentions are made of core radio fluxes, the LF is in this case the total RLF.

The radio data in Table 7.7 are stated at 5 GHz. Therefore if a correlation will be made between the Willott 151 MHz RLF and a 5 GHz RLF, the 151 MHz RLF must be shifted to 5 GHz, as will be detailed in §7.7.3.

The Willott total RLF also assumes an older cosmology than is standard today. The comoving volume element used in [122] is:

$$\frac{d^2V}{dzd\Omega} = \frac{c^3 z^2 (2+z)^2}{4H_{0,W}^3 (1+z)^3} \quad (7.9)$$

[10] where z is the redshift, $H_{0,W}$ is equal to 50 km/s/Mpc, and c is the speed of light. This will also be detailed further in §7.7.4. Figure 7.3 displays the total radio luminosity function.

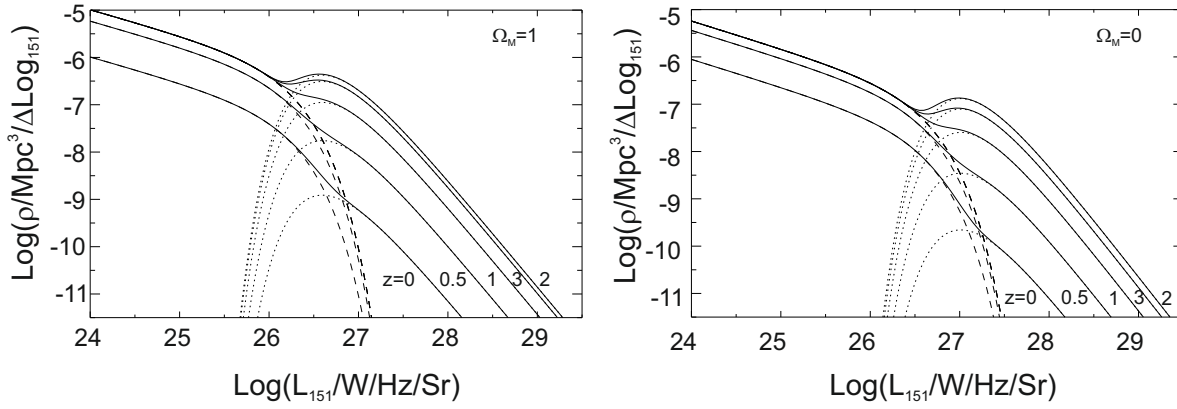


Figure 7.3: The radio LF from [122] at varying redshifts, for $\Omega_M = 1$ and $\Omega_M = 0$.

7.7.3 Transformation of radio luminosity function frequency

The RLF should be scaled from 151 MHz to 5 GHz using the power law proportionality

$$\frac{L(\nu)}{\nu} \propto \nu^{-\alpha_{R,tot}} \quad (7.10)$$

$$\frac{L(\nu_2) - L(\nu_1)}{\nu_2 - \nu_1} \propto (\nu_2 - \nu_1)^{-\alpha_{R,tot}} \quad (7.11)$$

where $\nu_1 = 5$ GHz and $\alpha_{R,tot}$ is an average spectral index selected for the $\nu_2 = 151$ MHz luminosity sampling.

7.7.4 Transformation of radio luminosity function cosmology

Returning to the older cosmology used by [122], and the comoving volume element shown in equation 7.9, a transformation must be made to a current cosmology. The standard Lambda CDM cosmology has $H_0 = 70$ km/s/Mpc, $\Omega_M = 0.27$, and $\Omega_\Lambda = 0.73$. The comoving volume element is:

$$\frac{d^2V}{dzd\Omega} = \frac{cd_L^2(z)}{H_0(1+z)^2 \sqrt{(1-\Omega_\Lambda - \Omega_M)(1+z)^2 + \Omega_M(1+z)^3 + \Omega_\Lambda}} \quad (7.12)$$

Taking the quotient of equations 7.9 and 7.12 and replacing all variables with their given numerical values, will produce a redshift-dependent conversion factor. The relationship between z and d_L in the Λ CDM cosmology is derived in §B.1. Thus the quotient, i.e. conversion factor, can be calculated based entirely on the redshift bin.

7.7.5 Selection of a reliable core radio luminosity function

The core radio luminosity function is designated as $\Phi_{R,core}(L, z)$. Yuan et al. 2012 [123] use a sample of 1063 radio loud AGN to investigate the core RLF at 5 GHz. Figure 7.4 displays the core luminosities versus total luminosities for radio galaxies and quasi-stellar objects:

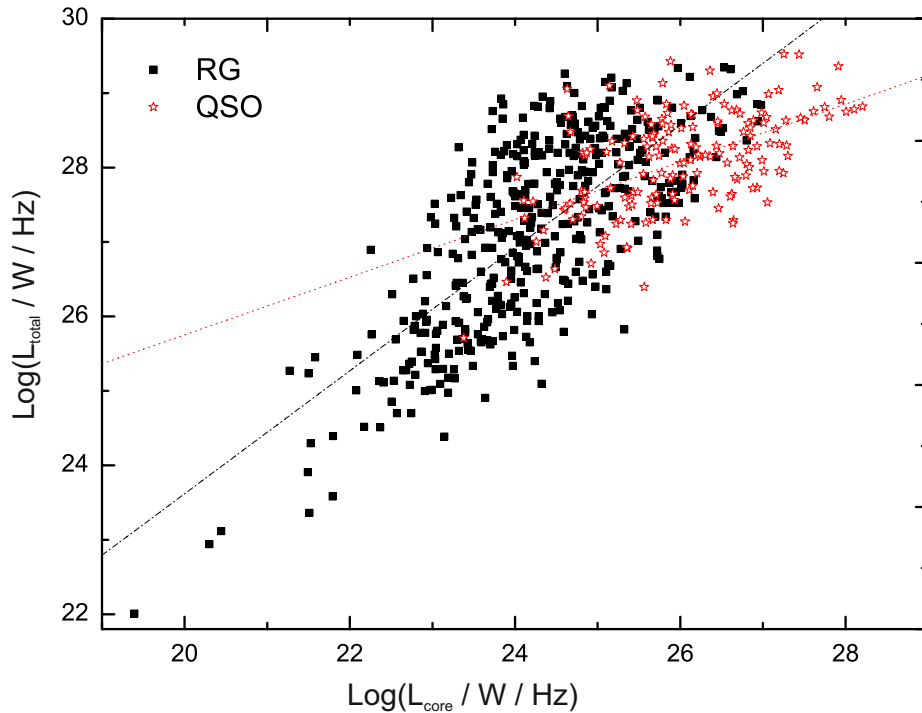


Figure 7.4: Total and core luminosities of radio galaxies and quasi-stellar objects modified from [123], with linear fitting.

7.7.6 Correlation between core radio luminosity and total radio luminosity

A linear relation between $L_{R,core}$ and $L_{R,tot}$ can be determined by plotting the observed total radio luminosities against the core radio luminosities from Table 7.9 as in Figure 7.5:

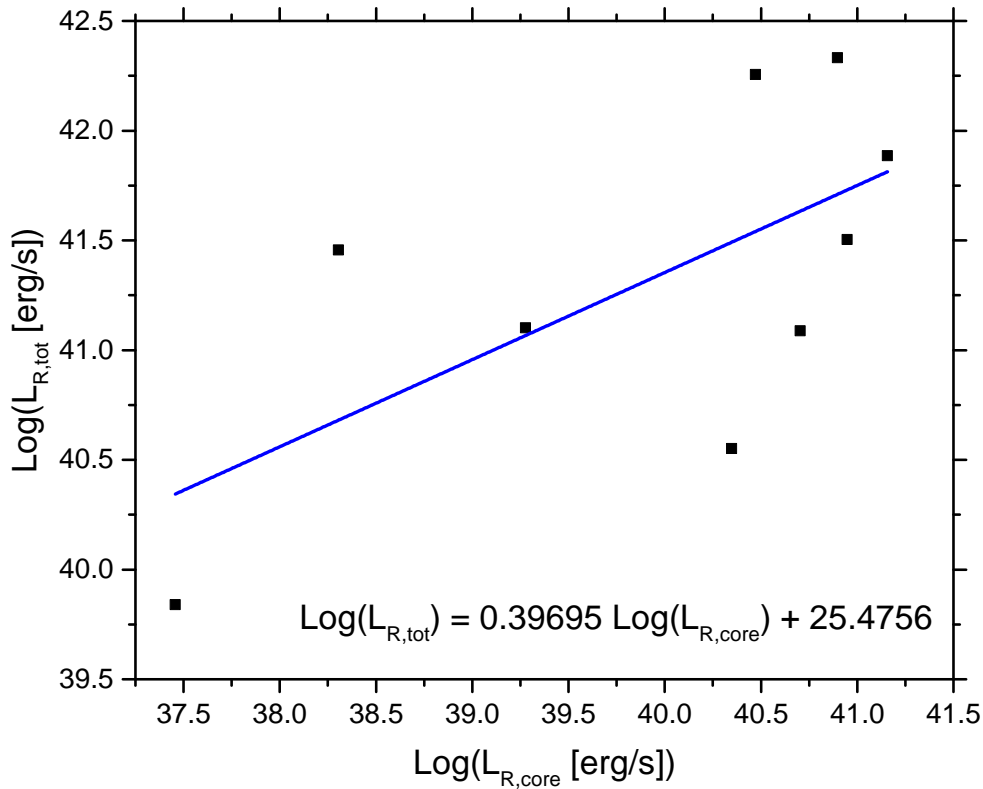


Figure 7.5: Plot of the total radio luminosity $\log L_{R,tot}$ versus the core radio luminosity $\log L_{R,core}$ for the population of radio galaxies detected by the 48 month Fermi-LAT survey. Data is from Tables 7.9, B.2, and B.3.

The slope is found to be $\frac{d\log L_{R,tot}}{d\log L_{R,core}} \cong 0.397$. Calculation details can be found in §B.4.

7.7.7 Calculation of the γ -ray luminosity function of the population

The γ -ray luminosity function may now be found, in relation to the total radio luminosity function:

$$\Phi_{\gamma}(L_{\gamma}, Z) = k\Phi_{R,tot}(L_{R,tot}, Z) \quad (7.13)$$

where k is an appropriate scaling factor. The correlation coefficient from Figure 7.1 which describes the relationship between the core radio luminosity

and the γ -ray luminosity may be inserted, as well as the coefficient from Figure 7.5 which describes the relationship between the total radio luminosity and the core radio luminosity:

$$\Phi_{\gamma}(L_{\gamma}, z) = k \frac{d \log L_{R,core}}{d \log L_{\gamma}} \frac{d \log L_{R,tot}}{d \log L_{R,core}} \Phi_{R,tot}(L_{R,tot}, z) \quad (7.14)$$

7.7.8 Calculation of diffuse γ -ray emission of the extended population

Finally the above results may be extended to the entire population of γ -ray emitting radio galaxies in the universe, to estimate the diffuse γ -ray energy flux above 100 MeV in erg/cm²/s by integrating over all possible redshifts and luminosities:

$$S_{\gamma}(> 100 \text{ MeV}) = k \frac{d \log L_{R,core}}{d \log L_{\gamma}} \frac{d \log L_{R,tot}}{d \log L_{R,core}} \int_{z=0}^{z=11.1} \int_{L_{\gamma}=10^{41}}^{L_{\gamma}=10^{50}} \frac{d^2 V}{dz d\Omega} \frac{L_{\gamma} (1+z)^{2-\Gamma_{avg}}}{4\pi d_L^2(z)} \Phi_{R,tot}(L_{R,tot}, z) \quad (7.15)$$

where the comoving volume element is integrated from a distance of zero redshift to the highest measured redshift thus far [124]. The γ -ray energy flux from equation 7.2 is integrated between the lowest luminosity in the radio galaxy population detected by Fermi in Table 7.9 and 10⁵⁰ erg/s [10], using the average spectral index from §7.4 of $\Gamma_{avg} \cong 2.18$. From this, the contribution to the total IGRB can be calculated.

7.8 Alternate theories for the origin of the IGRB

The IGRB is theorized to be the superposition of far-off unresolved γ -ray emitting sources, diffuse star formation, UHECRs interacting with the EBL, and annihilating dark matter particles. It has been proposed that alternatively, gravitational shock waves originating through large-scale structure formation such as the merging of separate clusters, produce relativistic leptons which inverse-Compton scatter CMB photons to γ -ray energies [125]. In

the case that the IGRB is a byproduct of structure formation in the universe, it can be expected that there are correlations between known clusters of galaxies and a mapping of the total IGRB [125].

7.9 Summary

The SSC and dark matter results for M 87, NGC 1275, Pictor A, and Centaurus A are summarized and discussed here, with the finding that the two-zone SSC model is able to well explain all the radio galaxies in the sample. The combined SSC and dark matter model is successful in extracting the neutralino mass and boost factor, with $m_\chi \approx 4.7$ TeV. Beyond SSC, other γ -ray emission mechanisms are discussed, including PeV neutrinos and UHE-CRs. The sample is then extended to all of the γ -ray emitting radio galaxies detected by the Fermi-LAT in a four year period, and their γ -ray luminosities and luminosity distances are calculated. Returning then to the data collection stage of this work, core and total radio data for γ -ray emitting radio galaxies are described, before calculating the core radio luminosities and total radio luminosities. All three types of luminosities for γ -ray emitting radio galaxies are brought together in Table 7.9, which is a valuable foundation from which the γ -ray luminosity function and diffuse γ -ray emission can be calculated.

Chapter 8

Summary

The incomplete understanding of the Isotropic Gamma-Ray Background has served as the initial motivation for this work. In order to attain a deeper understanding of the diffuse processes that can contribute to the IGRB, it is necessary to construct multiwavelength SEDs of γ -ray emitting AGN. SEDs constructed from simultaneous data provide a more accurate picture of the object than do those constructed from non-simultaneous data. Within AGN, radio galaxies are selected for investigation, as due to doppler beaming effects, they are detected in fewer numbers than blazars. Dark matter is investigated, as its annihilation is also thought to produce γ -rays, and the high density regions near the black holes of AGN provide optimal conditions for detection of a dark matter annihilation signature. Observations across all wavelength bands are collected for M 87, NGC 1275, Pictor A, and Centaurus A, including VHE γ -ray observations from Cherenkov telescopes. Core and total radio data is also collected and saved for a later stage. Fermi-LAT γ -ray raw data is analyzed in time ranges simultaneous to the Cherenkov observations, resulting in thorough SEDs for each galaxy. A self-consistent and time-dependent two-zone SSC model, which is able to explain the SED across 20 orders of magnitude including VHE γ -rays, is applied in fitting each SED. In some cases there is an excess between the fit and the observed data in the VHE γ -ray regime, which is well explained by the dark matter model introduced and applied here, from which a dark matter particle mass of $m_\chi \approx 4.7$ TeV is extracted. Returning to the collected core radio data and total radio data, the sample is extended to Fermi-LAT detected γ -ray emitting radio galaxies. Calculation of the core radio luminosities, total radio luminosities, and γ -ray luminosities produces a set of 9 γ -ray emitting radio galaxies from which a γ -ray luminosity function may be determined with

the aid of correlation coefficients and a reliable radio luminosity function. A foundation for the luminosity function, diffuse γ -ray emission, and IGRB contribution calculations, is hereby laid out.

Appendix A

Fermi Large Area Telescope analysis

A.1 Raw results for each object in the region of interest

A.1.1 M 87

2FGLJ1158.8+0939: GB6 J1158+0937

Prefactor: 6.72205 +/- 1.60159

Index: 2.38219 +/- 0.233324

Scale: 1408.79

TS value: 35.6322

Flux: 5.82231e-09 +/- 1.54029e-09 photons/cm²/s

2FGLJ1204.2+1144: 1RXS J120413.0+114549

Prefactor: 5.80286 +/- 1.30616

Index: 2.31483 +/- 0.20001

Scale: 1587.48

TS value: 42.1551

Flux: 6.27506e-09 +/- 1.50017e-09 photons/cm²/s

2FGLJ1209.7+1807: MG1 J120953+1809

Prefactor: 3.82383 +/- 1.47877

Index: 5 +/- 0.00616456

Scale: 831.124
TS value: 8.81619
Flux: $4.72067e-09 \pm 1.81368e-09$ photons/cm²/s

2FGLJ1214.6+1309: 4C +13.46
Prefactor: 4.99789 ± 1.81235
Index: 2.53942 ± 0.312829
Scale: 523.522
TS value: 15.6966
Flux: $4.01494e-09 \pm 1.39881e-09$ photons/cm²/s

2FGLJ1214.8+1653: TXS 1212+171
Prefactor: 1.72607 ± 1.6923
Index: 1.77041 ± 0.596984
Scale: 1432.48
TS value: 8.85523
Flux: $1.05961e-09 \pm 1.21139e-09$ photons/cm²/s

2FGLJ1224.9+2122: 4C +21.35
norm: 16.5155 ± 0.238889
alpha: 2.12155
beta: 0.0658717
Eb: 317.119
TS value: 23347.7
Flux: $4.59434e-07 \pm 6.63231e-09$ photons/cm²/s

2FGLJ1230.8+1224: M 87
Prefactor: 2.05289 ± 0.378289
Index: 2.28251 ± 0.17147
Scale: 1025.3
TS value: 57.3501
Flux: $7.94961e-09 \pm 1.63594e-09$ photons/cm²/s

2FGLJ1231.6+1417: GB6 J1231+1421
Prefactor: 2.74323 ± 1.00361
Index: 2.39887 ± 0.35173

Scale: 1635.47
TS value: 14.6523
Flux: $3.44598e-09 \pm 1.51773e-09$ photons/cm²/s

2FGLJ1251.2+1045: 1RXS J125117.4+103914
Prefactor: 9.79218 ± 3.58508
Index: 2.07489 ± 0.349756
Scale: 2793.13
TS value: 18.418
Flux: $2.79957e-09 \pm 1.4462e-09$ photons/cm²/s

2FGLJ1254.4+2209: TXS 1252+224
Prefactor: 1.58934 ± 0.669772
Index: 1.65314 ± 0.259543
Scale: 1925.12
TS value: 19.6648
Flux: $1.54395e-09 \pm 7.4817e-10$ photons/cm²/s

gal_2yearp7v6_0:
Prefactor: 0.907791 ± 0.0891743
Index: 0
Scale: 100
Flux: $0.000178171 \pm 1.75044e-05$ photons/cm²/s

iso_p7v6source:
Normalization: 1.1579 ± 0.0777449
Flux: $5.33005e-05 \pm 3.5789e-06$ photons/cm²/s

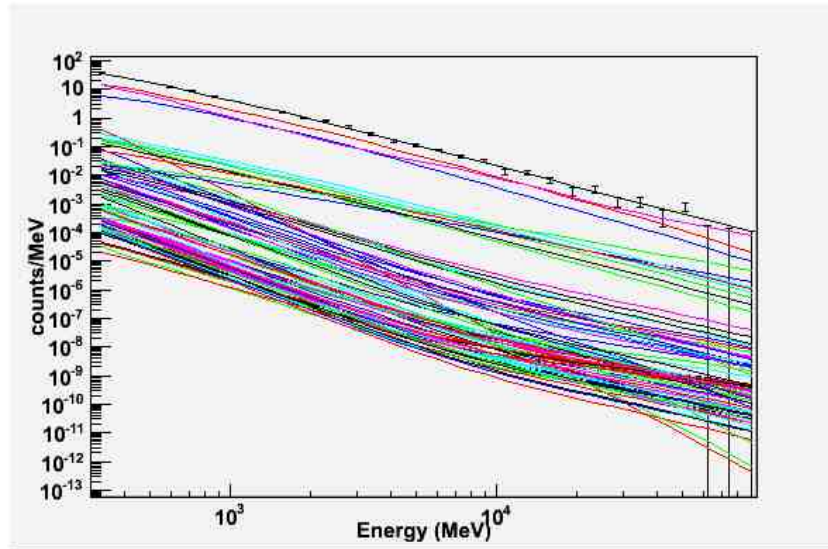


Figure A.1: Counts distribution over energy for M 87. Coloured lines indicate individual sources, and black line indicates their sum.

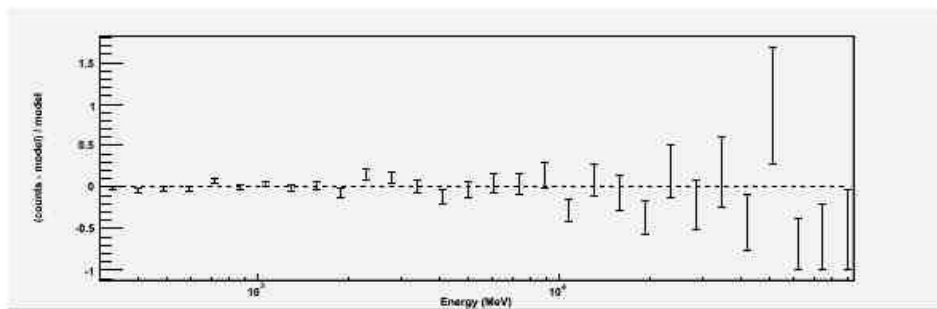


Figure A.2: Residuals plot of detected counts versus model expectations for M 87. This allowed a quick check for correctness during early steps in the analysis chain.

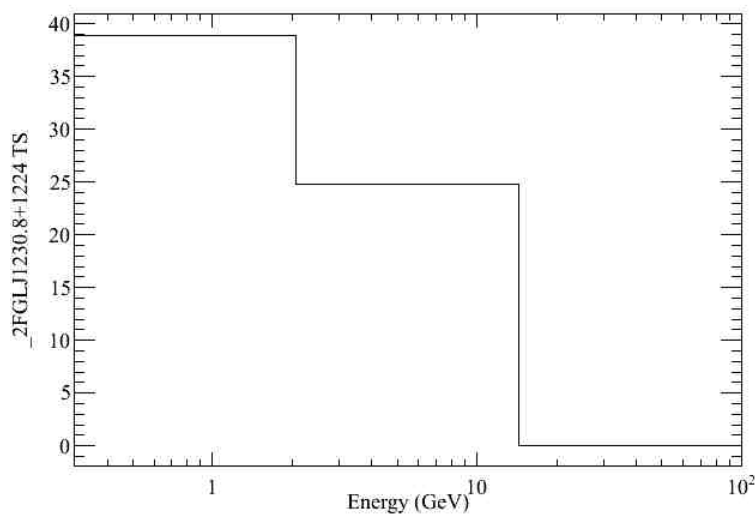


Figure A.3: Test statistic histogram for M 87.

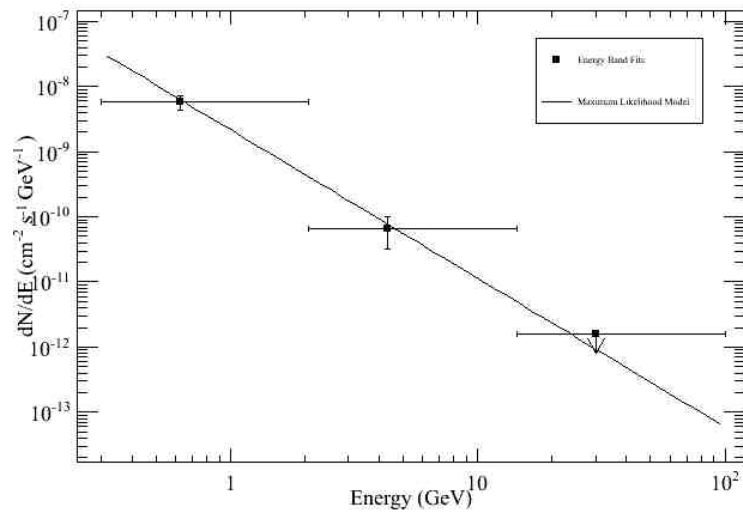


Figure A.4: Count spectrum for M 87.

A.1.2 NGC 1275

2FGLJ0303.5+4713: 4C +47.08

Prefactor: 5.99367 +/- 0.619917

Index: 2.20421 +/- 0.095887

Scale: 996.412

TS value: 212.893

Flux: $2.10711\text{e-}08$ +/- $2.44081\text{e-}09$ photons/cm²/s

2FGLJ0307.4+4915: No Assoc

Prefactor: 1.20053 +/- 0.838498

Index: 1.73742 +/- 0.40162

Scale: 2275.87

TS value: 10.767

Flux: $1.63049\text{e-}09$ +/- $1.52063\text{e-}09$ photons/cm²/s

2FGLJ0310.7+3813: B3 0307+38

Prefactor: 2.01897 +/- 2.54455

Index: 3.99982 +/- 1.14404

Scale: 1193.95

TS value: 7.3369

Flux: $5.09326e-09 \pm 2.05105e-09$ photons/cm²/s

2FGLJ0316.6+4119: IC 310

Prefactor: 0.505559 ± 3.60656

Index: 1.98161 ± 1.43465

Scale: 3186.29

TS value: 0.0176221

2FGLJ0319.8+4130: NGC 1275

norm: 3.35527 ± 0.115916

alpha: 1.99622

beta: 0.0659159

E_b: 1000.92

TS value: 3291.29

Flux: $1.05582e-07 \pm 3.6417e-09$ photons/cm²/s

2FGLJ0324.8+3408: 1H 0323+342

norm: 3.8163 ± 0.898765

alpha: 2.68524

beta: 0.869111

E_b: 372.764

TS value: 22.8726

Flux: $9.86332e-09 \pm 2.31589e-09$ photons/cm²/s

2FGLJ0340.4+4131: PSR J0340+4130

Prefactor: 4.23175 ± 0.670961

Index1: 0.958373

Scale: 1316.28

Cutoff: 2336.36

Index2: 1

TS value: 88.192

Flux: $8.79086e-09 \pm 1.39239e-09$ photons/cm²/s

2FGLJ0342.4+3859: GB6 J0342+3858

Prefactor: 0.175944 ± 0.341723

Index: 3.50583 ± 1.91381

Scale: 1074.15

TS value: 0.764694

Flux: $1.85157\text{e-}09 \pm 2.17458\text{e-}09$ photons/cm²/s

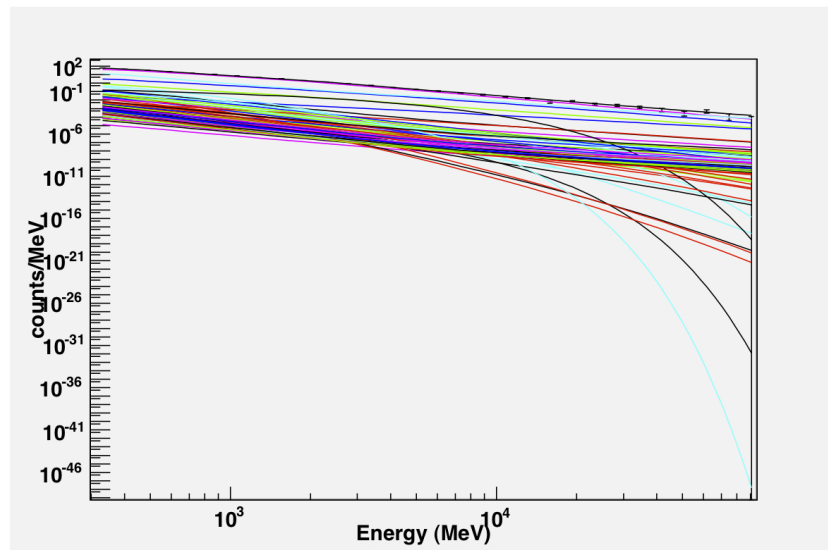


Figure A.5: Counts distribution over energy for NGC 1275. Coloured lines indicate individual sources, and black line indicates their sum.

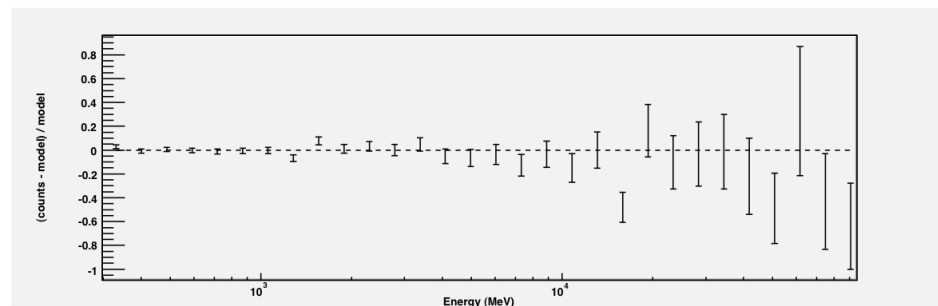


Figure A.6: Residuals plot of detected counts versus model expectations for NGC 1275. This allowed a quick check for correctness during early steps in the analysis chain.

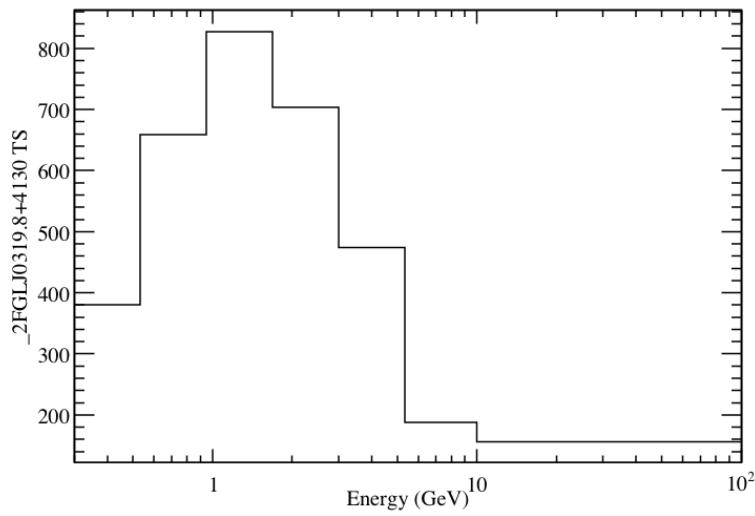


Figure A.7: Test statistic histogram for NGC 1275.

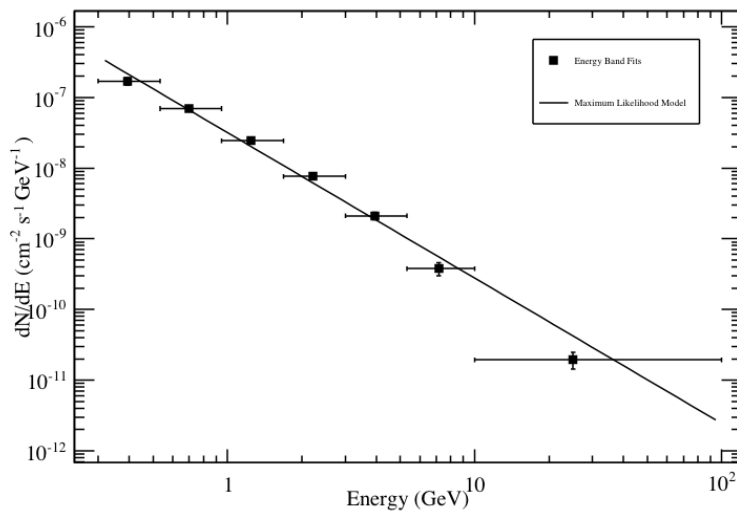


Figure A.8: Count spectrum for NGC 1275.

A.1.3 Pictor A

2FGLJ0437.3-4712:

Prefactor: 1.88383 +/- 0.112885

Index1: 1.35809

Scale: 582.751

Cutoff: 1152.79

Index2: 1

TS value: 660.056

Flux: $1.06489\text{e-}08 \pm 6.37095\text{e-}10$ photons/cm²/s

2FGLJ0438.8-4521:

Prefactor: 1.829 ± 0.202754

Index: 2.38926 ± 0.105747

Scale: 837.269

TS value: 162.482

Flux: $4.59643\text{e-}09 \pm 5.65766\text{e-}10$ photons/cm²/s

2FGLJ0449.4-4350:

Prefactor: 6.04822 ± 0.159136

Index: 1.8352 ± 0.0212109

Scale: 1255.36

TS value: 6210.79

Flux: $2.98571\text{e-}08 \pm 8.37758\text{e-}10$ photons/cm²/s

2FGLJ0456.1-4613:

Prefactor: 2.36565 ± 0.18747

Index: 2.66669 ± 0.0819001

Scale: 414.323

TS value: 437.496

Flux: $1.01001\text{e-}08 \pm 6.89591\text{e-}10$ photons/cm²/s

2FGLJ0515.0-4411:

Prefactor: 3.72332 ± 0.665672

Index: 2.94758 ± 0.211409

Scale: 534.396

TS value: 44.2691

Flux: $3.15559\text{e-}09 \pm 5.74318\text{e-}10$ photons/cm²/s

2FGLJ0516.5-4601:

Prefactor: 1.18897 ± 0.251486

Index: 2.57702 ± 0.217038

Scale: 782.032

TS value: 41.856

Flux: $2.67832e-09 \pm 6.49795e-10$ photons/cm²/s

2FGLJ0523.0-3628:

Prefactor: 5.14753 ± 0.180122

Index: 2.5385 ± 0.0380745

Scale: 457.708

TS value: 2626.2

Flux: $2.94046e-08 \pm 9.23737e-10$ photons/cm²/s

2FGLJ0526.1-4829:

Prefactor: 1.04463 ± 0.111308

Index: 2.28038 ± 0.103491

Scale: 1230.38

TS value: 181.368

Flux: $6.12496e-09 \pm 8.2104e-10$ photons/cm²/s

2FGLJ0531.8-3831:

Prefactor: 2.87821 ± 0.551259

Index: 2.71965 ± 0.195588

Scale: 596.777

TS value: 48.3572

Flux: $3.26871e-09 \pm 6.54611e-10$ photons/cm²/s

2FGLJ0532.0-4826:

Prefactor: 6.26067 ± 0.182976

Index: 2.13294 ± 0.027758

Scale: 1208.47

TS value: 4163.05

Flux: $3.23918e-08 \pm 1.06176e-09$ photons/cm²/s

2FGLJ0538.5-3909:

Prefactor: 2.1155 ± 0.421106

Index: 2.32035 ± 0.200197

Scale: 1569

TS value: 43.4521

Flux: $2.23757e-09 \pm 6.15264e-10$ photons/cm²/s

2FGLJ0538.8-4405:

norm: 3.05283 ± 0.0352285

alpha: 2.01159

beta: 0.0440284

E_b: 371.966

TS value: 31376.7

Flux: $1.31823e-07 \pm 1.51848e-09$ photons/cm²/s

2FGLJ0555.9-4348:

Prefactor: 1.72315 ± 0.396783

Index: 2.19925 ± 0.201744

Scale: 1641.24

TS value: 30.7519

Flux: $1.812e-09 \pm 5.48138e-10$ photons/cm²/s

2FGLJ0558.2-3837:

Prefactor: 3.40298 ± 0.782178

Index: 1.92667 ± 0.162598

Scale: 1282.75

TS value: 70.5206

Flux: $1.80521e-09 \pm 4.96796e-10$ photons/cm²/s

2FGLJ0602.7-4011:

Prefactor: 5.26645 ± 0.608013

Index: 2.08867 ± 0.10262

Scale: 1508.3

TS value: 175.508

Flux: $4.23345e-09 \pm 6.32725e-10$ photons/cm²/s

2FGLJ0604.2-4817:

Prefactor: 5.2213 ± 0.988089

Index: 1.88306 ± 0.164903

Scale: 3368.77

TS value: 68.4341

Flux: $1.67834\text{e-}09 \pm 4.96761\text{e-}10$ photons/cm²/s

Pictor A:

Prefactor: 1.37905 ± 5.47429

Index: 2.30427 ± 0.299137

Scale: 534.355 ± 921.011

TS value: 13.9568

Flux: $1.2016\text{e-}09 \pm 5.84223\text{e-}10$ photons/cm²/s

And the two diffuse background fits:

gal_2yearp7v6_0:

Prefactor: 1.14633 ± 0.0542212

Index: $-0.000873794 \pm 0.013968$

Scale: 100

Flux: $0.000224612 \pm 6.28243\text{e-}06$ photons/cm²/s

iso_p7v6source:

Normalization: 0.866348 ± 0.0282664

Flux: $3.98797\text{e-}05 \pm 1.30121\text{e-}06$ photons/cm²/s

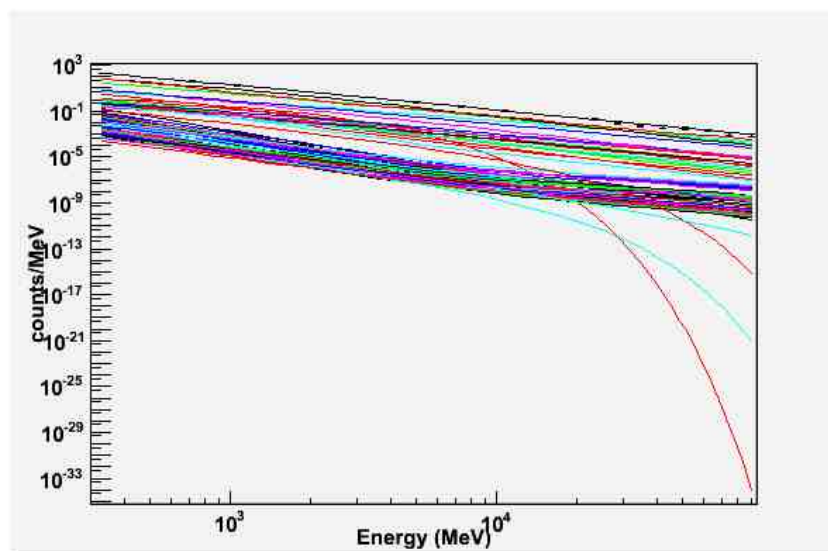


Figure A.9: Counts distribution over energy for Pictor A. Coloured lines indicate individual sources, and black line indicates their sum.

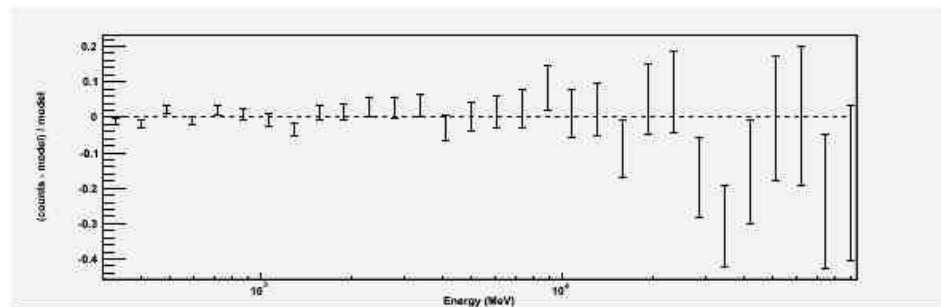


Figure A.10: Residuals plot of detected counts versus model expectations for Pictor A. This allowed a quick check for correctness during early steps in the analysis chain.

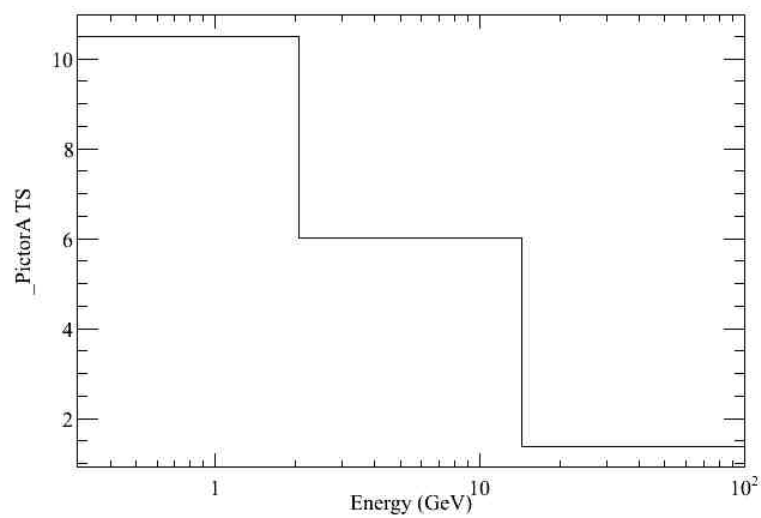


Figure A.11: Test statistic histogram for Pictor A.

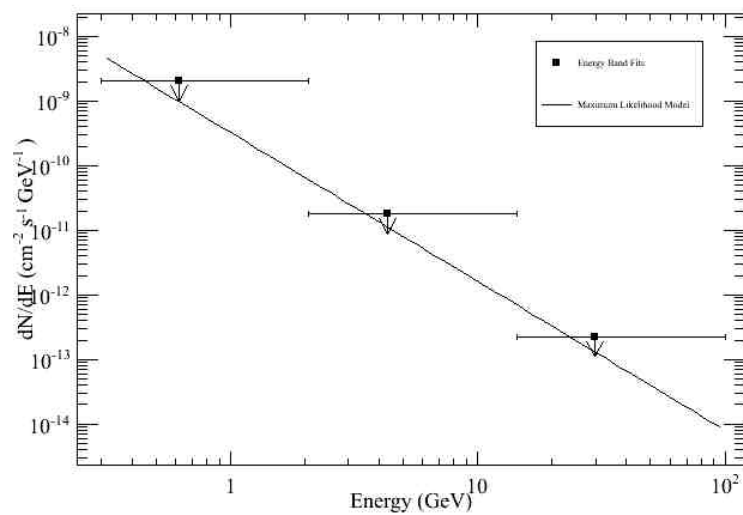


Figure A.12: Count spectrum for Pictor A.

A.2 Spectral fit results

A.2.1 M 87 - power law

$$\frac{dN}{dE} = (2.05 \pm 0.38) \left(\frac{E}{1025.3 \text{ MeV}} \right)^{-2.28 \pm 0.17} \text{ ph/cm}^2/\text{s/MeV} \quad (\text{A.1})$$

A.2.2 NGC 1275 - log parabola

$$\frac{dN}{dE} = (3.36 \pm 0.12) \frac{E}{1000.92} \left(2.00 + 0.07 \ln \frac{E}{1000.92} \right) \text{ ph/cm}^2/\text{s/MeV} \quad (\text{A.2})$$

A.2.3 Pictor A - power law

$$\frac{dN}{dE} = (1.38 \pm 5.47) \left(\frac{E}{534.36 \text{ MeV}} \right)^{-2.30 \pm 0.30} \text{ ph/cm}^2/\text{s/MeV} \quad (\text{A.3})$$

A.2.4 Centaurus A - power law

As calculated by [96],

$$\frac{dN}{dE} \approx \left(\frac{E}{100 \text{ MeV}} \right)^{-2.76 \pm 0.07} \text{ ph/cm}^2/\text{s/MeV} \quad (\text{A.4})$$

Appendix B

Calculations

B.1 Derivation of the luminosity distance d_L

The luminosity distance d_L is derived for each source using the redshift and cosmological parameters.

From Hogg 1999 [126], $\Omega_M + \Omega_L + \Omega_k = 1$ where Ω_k is the curvature of space parameter. For our choice of cosmology ($\Omega_M = 0.27$, $H_0 = 70$ km/s/Mpc), $\Omega_k = 0$ implying there is an analytic solution for d_M , and

$$d_L = (1 + z)d_M$$

$$d_L = (1 + z)d_H \frac{2[2 - \Omega_M(1-z) - (2 - \Omega_M)\sqrt{1 + \Omega_M z}]}{(1+z)\Omega_M^2}$$

where $c_0 = 300\,000$ km/s, and the Hubble Distance $d_H = c_0/H_0$

$$d_L = \frac{300000 \text{ km/s}}{70 \text{ km/s/Mpc}} \frac{2(2 - (0.27)(1-z) - (1.73)\sqrt{1 + (0.27)z})}{(0.27)^2}$$

$$d_L = \frac{300000}{70} \frac{2}{0.0729} (1.73 + (0.27)z - (1.73)\sqrt{1 + (0.27)z}) \text{ Mpc for every } z.$$

Note that $1 \text{ Mpc} = 3.08568 \times 10^{24} \text{ cm}$.

B.2 Calculation of $\alpha_{R,core}$ from TANAMI measurements

$$\alpha_{R,core} = \frac{\log \frac{S(v_1)}{S(v_2)}}{\log \frac{v_1}{v_2}} \quad (\text{B.1})$$

In every case, $\nu_1 = 8.441$ and $\nu_2 = 22.316$

$$\alpha_{R,core} = \frac{\log \frac{S(\nu_1)}{S(\nu_2)}}{\log \frac{8.441}{22.316}}$$

$$\alpha_{R,core} = -2.3684 \log \frac{S(\nu_1)}{S(\nu_2)}$$

By the log identity

$$\alpha_{R,core} = -2.3684(\log S(\nu_1) - \log S(\nu_2)) \quad (\text{B.2})$$

The exact formula for error propagation is

$$\sigma_x^2 = \left(\frac{\delta x}{\delta a}\right)^2 \sigma_a^2 + \left(\frac{\delta x}{\delta b}\right)^2 \sigma_b^2 \quad (\text{B.3})$$

in this case

$$\sigma_{\alpha_{R,core}}^2 = \left(\frac{\delta \alpha_{R,core}}{\delta S(\nu_1)}\right)^2 \sigma_{S(\nu_1)}^2 + \left(\frac{\delta \alpha_{R,core}}{\delta S(\nu_2)}\right)^2 \sigma_{S(\nu_2)}^2 \quad (\text{B.4})$$

where

$\alpha_{R,core}$ is the radio core spectral index

$\sigma_{\alpha_{R,core}}$ is the uncertainty on $\alpha_{R,core}$

$S(\nu_1)$ is the energy flux of the source at frequency ν_1

$\sigma_{S(\nu_1)}$ is the uncertainty on $S(\nu_1)$

$S(\nu_2)$ is the energy flux of the source at frequency ν_2

$\sigma_{S(\nu_2)}$ is the uncertainty on $S(\nu_2)$

With reference to Table 7.4 in §7.5, every $\sigma_{S(\nu_1)} = \frac{S(\nu_1)}{10}$ and $\sigma_{S(\nu_2)} = \frac{S(\nu_2)}{10}$.

Therefore

$$\sigma_{\alpha_{R,core}}^2 = \left(\frac{\delta \alpha_{R,core}}{\delta S(\nu_1)}\right)^2 \frac{S^2(\nu_1)}{10^2} + \left(\frac{\delta \alpha_{R,core}}{\delta S(\nu_2)}\right)^2 \frac{S^2(\nu_2)}{10^2} \quad (\text{B.5})$$

calculating the partial derivatives,

$$\frac{\delta \alpha_{R,core}}{\delta S(\nu_1)} = -2.3684 \frac{\delta}{\delta S(\nu_1)} \log S(\nu_1)$$

$$\frac{\delta \alpha_{R,core}}{\delta S(\nu_1)} = -2.3684 \frac{1}{S(\nu_1) \ln 10}$$

$$\frac{\delta\alpha_{R,core}}{\delta S(\nu_2)} = +2.3684 \frac{\delta}{\delta S(\nu_2)} \log S(\nu_2)$$

$$\frac{\delta\alpha_{R,core}}{\delta S(\nu_2)} = +2.3684 \frac{1}{S(\nu_2) \ln 10}$$

and,

$$\sigma_{\alpha_{R,core}}^2 = \left(\frac{2.3684}{\ln 10}\right)^2 \left(\frac{1}{S^2(\nu_1)} \frac{S^2(\nu_1)}{10^2} + \frac{1}{S^2(\nu_2)} \frac{S^2(\nu_2)}{10^2}\right)$$

$$\sigma_{\alpha_{R,core}}^2 = \left(\frac{2.3684}{\ln 10}\right)^2 \left(\frac{2}{100}\right)$$

$$\sigma_{\alpha_{R,core}} = \frac{2.3684}{\ln 10} \sqrt{\frac{2}{100}}$$

$$\sigma_{\alpha_{R,core}} = 0.1455$$

$$\sigma_{\alpha_{R,core}} \approx \pm 0.15 \quad (\text{B.6})$$

B.2.1 Pictor A

With reference to Table 7.4,

$$\alpha_{R,core} = -2.3684 (\log S(\nu_1) - \log S(\nu_2))$$

$$\alpha_{R,core} = -2.3684 (\log(571.8) - \log(541.0))$$

$$\alpha_{R,core} = -0.0570$$

$$\alpha_{R,core} \approx -0.06 \pm 0.15$$

B.2.2 Centaurus A

With reference to Table 7.4,

$$\alpha_{R,core} = -2.3684 (\log S(\nu_1) - \log S(\nu_2))$$

$$\alpha_{R,core} = -2.3684 (\log(493.0) - \log(1620.0))$$

$$\alpha_{R,core} = 1.2237$$

$$\alpha_{R,core} \approx 1.22 \pm 0.15$$

B.2.3 OH -342 (Trial 1)

With reference to Table 7.4,

$$\alpha_{R,core} = -2.3684 (\log S(\nu_1) - \log S(\nu_2))$$

$$\alpha_{R,core} = -2.3684 (\log(368.0) - \log(235.0))$$

$$\alpha_{R,core} = -0.4613$$

$$\alpha_{R,core} \approx -0.46 \pm 0.15$$

B.2.4 OH -342 (Trial 2)

With reference to Table 7.4,

$$\alpha_{R,core} = -2.3684 (\log S(\nu_1) - \log S(\nu_2))$$

$$\alpha_{R,core} = -2.3684 (\log(342.0) - \log(209.0))$$

$$\alpha_{R,core} = -0.5066$$

$$\alpha_{R,core} \approx -0.51 \pm 0.15$$

B.3 Extrapolation of TANAMI and MOJAVE $S_{R,core}$ from various frequencies to 5 GHz

$$S(\nu) = \nu^\alpha \quad (\text{B.7})$$

$$\Delta S(\nu) = (\Delta \nu)^\alpha \quad (\text{B.8})$$

$$\log(\Delta S(\nu)) = \log((\Delta \nu)^\alpha) = \alpha \log(\Delta \nu) \quad (\text{B.9})$$

$$\alpha = \frac{\log(S_2(\nu_2) - S_1(\nu_1))}{\log(\nu_2 - \nu_1)} = \frac{\log(S_2(\nu_2)/S_1(\nu_1))}{\log(\nu_2/\nu_1)} \quad (\text{B.10})$$

$$\alpha \log(\nu_2/\nu_1) = \log(S_2(\nu_2)/S_1(\nu_1)) = \log S_2(\nu_2) - \log S_1(\nu_1) \quad (\text{B.11})$$

$$\log S_1(\nu_1) = \log S_2(\nu_2) - \alpha \log(\nu_2/\nu_1) \quad (\text{B.12})$$

$$10^{\log S_1(\nu_1)} = 10^{\log S_2(\nu_2) - \alpha \log(\nu_2/\nu_1)} \quad (\text{B.13})$$

$$S_1(\nu_1) = 10^{\log S_2(\nu_2) - \alpha \log(\nu_2/\nu_1)} \quad (\text{B.14})$$

B.3.1 Pictor A

$$S_1(\nu_1) = 10^{\log S_2(\nu_2) - \alpha \log(\nu_2/\nu_1)} \quad (\text{B.15})$$

$$S(5\text{GHz}) = 10^{\log 541.0 - (-0.06) \log(22.316/5)} \quad (\text{B.16})$$

$$S(5\text{GHz}) = 591.8\text{mJy} = 0.592\text{Jy} \quad (\text{B.17})$$

B.3.2 Centaurus A

$$S(5\text{GHz}) = 10^{\log 1620.0 - (1.22) \log(22.316/5)} \quad (\text{B.18})$$

$$S(5\text{GHz}) = 261.2\text{mJy} = 0.261\text{Jy} \quad (\text{B.19})$$

B.3.3 OH -342 (Trial 2)

$$S(5\text{GHz}) = 10^{\log 209.0 - (-0.51) \log(22.316/5)} \quad (\text{B.20})$$

$$S(5\text{GHz}) = 448.2\text{mJy} = 0.448\text{Jy} \quad (\text{B.21})$$

B.3.4 NGC 1275

$$S(5\text{GHz}) = 10^{\log 1.380 - (0.48) \log(15.4/5)} \quad (\text{B.22})$$

$$S(5\text{GHz}) = 0.804\text{Jy} \quad (\text{B.23})$$

B.3.5 M 87

$$S(5\text{GHz}) = 10^{\log 1.408 - (0.24) \log(15.4/5)} \quad (\text{B.24})$$

$$S(5\text{GHz}) = 1.075\text{Jy} \quad (\text{B.25})$$

B.3.6 NGC 6251

$$S(5\text{GHz}) = 10^{\log 0.664 - (0.65) \log(15.4/5)} \quad (\text{B.26})$$

$$S(5\text{GHz}) = 0.320\text{Jy} \quad (\text{B.27})$$

B.4 Calculation tables for d_L , L_γ , $L_{R,\text{core}}$ and $L_{R,\text{tot}}$

Name	z	dL [Mpc]	dL [cm]	S [erg/cm ² /s]	ΔS [erg/cm ² /s]	Γ	$\Delta\Gamma$	L_γ (100MeV - 100GeV) [erg/s]	Log L_γ
NGC 1275	0.018	77.74195935	2.39887E+26	1.99E-10	3.90E-12	2.08		1.44183E+44	44.159
Pictor A	0.035	152.2599592	4.69826E+26	4.68E-12	1.20E-12	2.49	0.18	1.32023E+43	43.121
M87	0.004	17.17249828	5.29888E+25	1.45E-11	1.30E-12	2.04	0.07	5.12406E+41	41.710
Cen A									
Core	0.001	4.287567607	1.32301E+25	6.65E-11	2.10E-12	2.70	0.03	1.46372E+41	41.165
IC 310	0.019	82.09599986	2.53322E+26	7.58E-12	1.50E-12	1.90	0.14	6.10109E+42	42.785
OH -342	0.055	241.2800893	7.44513E+26	1.69E-11	1.60E-12	1.87	0.06	1.16694E+44	44.067
NGC 1218	0.029	125.8384946	3.88297E+26	6.59E-12	1.10E-12	2.07	0.11	1.2511E+43	43.097
NGC 2484	0.043	187.6932159	5.79161E+26	2.82E-12	7.00E-13	2.16	0.16	1.19669E+43	43.078
NGC 6251	0.025	108.2974458	3.34171E+26	1.10E-11	9.00E-13	2.04	0.08	1.53812E+43	43.187
3C 111	0.049	214.4212266	6.61635E+26	1.63E-11	1.50E-12	2.79	0.08	9.28924E+43	43.968
3C 264	0.022	95.18018824	2.93696E+26	2.97E-12	7.00E-13	1.98	0.20	3.2179E+42	42.508
3C 303	0.141	640.4513697	1.97623E+27	2.19E-12	6.00E-13	1.91	0.18	1.06212E+44	44.026
4C+39.12	0.021	90.81511578	2.80226E+26	4.18E-12	1.00E-12	2.11	0.17	4.13425E+42	42.616
Fornax A	0.006	25.78096029	7.95518E+25	5.30E-12	8.00E-13	2.20	0.11	4.21993E+41	41.625
Cen B	0.013	56.02699073	1.72881E+26	2.49E-11	3.00E-12	2.32	0.09	9.3983E+42	42.973

Figure B.1: Calculation of luminosity distance using equation 7.3 derived in Appendix B.1 and γ -ray luminosity using equation 7.2. Log values are plotted in Figure 7.1 to estimate the core- γ luminosity correlation.

Name	z	dL [Mpc]	dL [cm]	S core (5 GHz) [Jy]	ΔS core (5 GHz) [Jy]	α core	$\Delta\alpha$ core	$L_{R\text{ core}}$ (5 GHz) [erg/s]	Log $L_{R\text{ core}}$
NGC 1275	0.018	77.74195935	2.39887E+26	0.814		0.48	0.10	2.916E+40	40.465
Pictor A	0.035	152.2599592	4.69826E+26	0.591		-			
M87	0.004	17.17249828	5.29888E+25	1.082	0.013	0.06	0.15	7.90321E+40	40.898
Cen A						0.24	0.10	1.90309E+39	39.279
Core	0.001	4.287567607	1.32301E+25	0.261	0.005	1.22	0.15	2.87104E+37	37.458
IC 310	0.019	82.09599986	2.53322E+26					0	0.000
OH -342	0.055	241.2800893	7.44513E+26	0.447	0.010	0.51	0.15	1.43589E+41	41.157
NGC 1218	0.029	125.8384946	3.88297E+26	0.964	0.164			8.87504E+40	40.948
NGC 2484	0.043	187.6932159	5.79161E+26					0	0.000
NGC 6251	0.025	108.2974458	3.34171E+26	0.325	0.001	0.65	0.10	2.26073E+40	40.354
3C 111	0.049	214.4212266	6.61635E+26	1.14		-0.2		2.96068E+41	41.471
3C 264	0.022	95.18018824	2.93696E+26					0	0.000
3C 303	0.141	640.4513697	1.97623E+27					0	0.000
4C+39.12	0.021	90.81511578	2.80226E+26					0	0.000
Fornax A	0.006	25.78096029	7.95518E+25	0.051		0.5		2.02186E+38	38.306
Cen B	0.013	56.02699073	1.72881E+26	2.73				5.06092E+40	40.704

Figure B.2: Calculation of luminosity distance using equation 7.3 and core radio luminosity at 5 GHz in erg/s using equation 7.6. Log values are plotted in Figures 7.1 and 7.5 to estimate the core- γ luminosity and core-total luminosity correlations.

Name	z	dL [Mpc]	dL [cm]	S total (5 GHz) [Jy]	ΔS total (5 GHz) [Jy]	α total	$\Delta\alpha$ total	Lr total (5 GHz) [erg/s]	Log Lr total
NGC 1275	0.018	77.74195935	2.39887E+26			0.78		0	0.000
Pictor A	0.035	152.2599592	4.69826E+26	15.45		0.47	1.07	2.14797E+42	42.332
M87	0.004	17.17249828	5.29888E+25	71.566		0.993	0.79	1.26151E+41	41.101
Cen A									
Core	0.001	4.287567607	1.32301E+25	62.837		0.099	0.70	6.90858E+39	39.839
IC 310	0.019	82.09599986	2.53322E+26	0.258		0.031	0.75	1.03538E+40	40.015
OH -342	0.055	241.2800893	7.44513E+26	2.25		0.09	0.65	7.69075E+41	41.886
NGC 1218	0.029	125.8384946	3.88297E+26	3.40		0.11	0.64	3.188E+41	41.504
NGC 2484	0.043	187.6932159	5.79161E+26					0	0.000
NGC 6251	0.025	108.2974458	3.34171E+26	0.510		0.050	0.72	3.55374E+40	40.551
3C 111	0.049	214.4212266	6.61635E+26	6.637		0.996	0.73	1.8021E+42	42.256
3C 264	0.022	95.18018824	2.93696E+26					0	0.000
3C 303	0.141	640.4513697	1.97623E+27					0	0.000
4C+39.12	0.021	90.81511578	2.80226E+26					0	0.000
Fornax A	0.006	25.78096029	7.95518E+25	72		0.52		2.85473E+41	41.456
Cen B	0.013	56.02699073	1.72881E+26	6.58		1.04	0.13	1.22186E+41	41.087

Figure B.3: Calculation of luminosity distance using equation 7.3 and total radio luminosity at 5 GHz in erg/s using equation 7.6. Log values are plotted in Figure 7.5 to estimate the core-total luminosity correlation.

Bibliography

- [1] WL Kraushaar, GW Clark, GP Garmire, R Borke, P Higbie, V Leong, and T Thorsos. High-energy cosmic gamma-ray observations from the oso-3 satellite. *The Astrophysical Journal*, 177:341, 1972.
- [2] Reshmi Mukherjee and Jules Halpern. Multifrequency strategies for the identification of gamma-ray sources. In *Cosmic Gamma-Ray Sources*, pages 311–344. Springer, 2004.
- [3] M Ajello, D Gasparrini, Miguel Sánchez-Conde, G Zaharijas, M Gustafsson, J Cohen-Tanugi, CD Dermer, Y Inoue, D Hartmann, M Ackermann, et al. The origin of the extragalactic gamma-ray background and implications for dark matter annihilation. *The Astrophysical Journal Letters*, 800(2):L27, 2015.
- [4] Stanley D Hunter, DL Bertsch, JR Catelli, TM Dame, SW Digel, BL Dingus, JA Esposito, CE Fichtel, RC Hartman, G Kanbach, et al. Egret observations of the diffuse gamma-ray emission from the galactic plane. *The Astrophysical Journal*, 481(1):205, 1997.
- [5] Mattia Di Mauro, Fermi-LAT Collaboration, et al. Isotropic diffuse and extragalactic γ -ray background: emission from extragalactic sources vs dark matter annihilating particles. In *Journal of Physics: Conference Series*, volume 718, page 042019. IOP Publishing, 2016.
- [6] Fermi LAT Collaboration et al. Limits on dark matter annihilation signals from the fermi lat 4-year measurement of the isotropic gamma-ray background. *Journal of Cosmology and Astroparticle Physics*, 2015 (09):008, 2015.
- [7] CGRO Science Support Center. Egret technical information, 2005. URL https://heasarc.gsfc.nasa.gov/docs/cgro/egret/egret_tech.html#B.

- [8] AA Abdo, Markus Ackermann, Marco Ajello, A Allafort, Luca Baldini, J Ballet, Guido Barbiellini, MG Baring, D Bastieri, K Bechtol, et al. Insights into the high-energy γ -ray emission of markarian 501 from extensive multifrequency observations in the fermi era. *The Astrophysical Journal*, 727(2):129, 2011.
- [9] Yoshiyuki Inoue. Contribution of gamma-ray-loud radio galaxies'core emissions to the cosmic mev and gev gamma-ray background radiation. *The Astrophysical Journal*, 733(1):66, 2011.
- [10] MATTIA Di Mauro, F Calore, F Donato, M Ajello, and L Latronico. Diffuse γ -ray emission from misaligned active galactic nuclei. *The Astrophysical Journal*, 780(2):161, 2014.
- [11] Fabrizio Tavecchio, Laura Maraschi, and Gabriele Ghisellini. Constraints on the physical parameters of tev blazars. *The Astrophysical Journal*, 509(2):608, 1998.
- [12] C Megan Urry and Paolo Padovani. Unified schemes for radio-loud active galactic nuclei. *Publications of the Astronomical Society of the Pacific*, 107(715):803–890, 1995.
- [13] C Megan Urry. Agn unification: An update. *arXiv preprint astro-ph/0312545*, 2003.
- [14] Goddard Space Flight Center. Exploring active galactic nuclei, 2016. URL <https://fermi.gsfc.nasa.gov/science/eteu/agn/>.
- [15] VA Acciari, E Aliu, T Arlen, T Aune, M Beilicke, W Benbow, D Boltuch, V Bugaev, A Cannon, L Ciupik, et al. Multiwavelength observations of the very high energy blazar 1es 2344+ 514. *The Astrophysical Journal*, 738(2):169, 2011.
- [16] RD Blandford and A Königl. Relativistic jets as compact radio sources. *The Astrophysical Journal*, 232:34–48, 1979.
- [17] KI Kellermann, YY Kovalev, ML Lister, DC Homan, M Kadler, MH Cohen, E Ros, JA Zensus, RC Vermeulen, MF Aller, et al. Doppler boosting, superluminal motion, and the kinematics of agn jets. *Astrophysics and Space Science*, 311(1-3):231–239, 2007.
- [18] Volker Beckmann and Chris Shrader. *Active galactic nuclei*. John Wiley & Sons, 2013.

- [19] George B Rybicki and Alan P Lightman. *Radiative processes in astrophysics*. John Wiley & Sons, 1979.
- [20] J Chiang and R Mukherjee. The luminosity function of the egret gamma-ray blazars. *The Astrophysical Journal*, 496(2):752, 1998.
- [21] Lars Bergström, Joakim Edsjö, and Piero Ullio. Spectral gamma-ray signatures of cosmological dark matter annihilations. *Physical Review Letters*, 87(25):251301, 2001.
- [22] PAR Ade, N Aghanim, C Armitage-Caplan, M Arnaud, M Ashdown, F Atrio-Barandela, J Aumont, C Baccigalupi, AJ Banday, RB Barreiro, et al. Planck 2013 results. xvi. cosmological parameters. *arXiv preprint arXiv:1303.5076*, 2013.
- [23] Benjamin W Lee and Steven Weinberg. Cosmological lower bound on heavy-neutrino masses. *Physical Review Letters*, 39(4):165, 1977.
- [24] Kim Griest and Marc Kamionkowski. Unitarity limits on the mass and radius of dark-matter particles. *Physical Review Letters*, 64(6):615, 1990.
- [25] N Jarosik, CL Bennett, J Dunkley, B Gold, MR Greason, M Halpern, RS Hill, G Hinshaw, A Kogut, E Komatsu, et al. Seven-year wilkinson microwave anisotropy probe (wmap) observations: sky maps, systematic errors, and basic results. *The Astrophysical Journal Supplement Series*, 192(2):14, 2011.
- [26] CERN. The standard model, 2017. URL <https://home.cern/about/physics/standard-model>.
- [27] Mark Srednicki. Supersymmetric grand unified theories and the early universe. *Nuclear Physics B*, 202(2):327–335, 1982.
- [28] S Saxena. Completing the spectral energy distribution of messier 87 with magic data and predicting dark matter annihilation. wissenschaftliche arbeit zur promotionspruefung am lehrstuhl fuer astronomie. *Universitaet Wuerzburg*, 2010.
- [29] Claire Chandler National Radio Astronomy Observatory, Amy Mioduszewski. Very long baseline array, 2014. URL <https://science.nrao.edu/facilities/vlba>.

- [30] National Aeronautics and Space Administration. The very long baseline array. URL <http://www.nasa.gov/topics/universe/features/rxte-bullets.html>.
- [31] ML Lister and DC Homan. Mojave: monitoring of jets in active galactic nuclei with vlba experiments. i. first-epoch 15 ghz linear polarization images. *The Astronomical Journal*, 130(4):1389, 2005.
- [32] MOJAVE program. The mojave program homepage. URL <http://www.physics.purdue.edu/MOJAVE/>.
- [33] TANAMI program. Tanami - project description, 2010. URL <http://pulsar.sternwarte.uni-erlangen.de/tanami/about/>.
- [34] Robin Wark Nuria McKay. Australia telescope national facility, 2013. URL <http://www.narrabri.atnf.csiro.au/>.
- [35] National Aeronautics and Space Administration. Chandra x-ray observatory, 2016. URL <http://nssdc.gsfc.nasa.gov/nmc/spacecraftDisplay.do?id=1999-040B>.
- [36] NGST. Chandra technical specifications, 2008. URL <http://chandra.harvard.edu/press/fact1.html>.
- [37] National Aeronautics and Space Administration. Chandra x-ray observatory, 2015. URL http://www.nasa-usa.de/mission_pages/chandra/main/chandra_fact_sheets.html.
- [38] Smithsonian Astrophysical Observatory. Chandra specifications, 2015. URL http://chandra.harvard.edu/resources/handouts/lithos/chandra_specs_litho.pdf.
- [39] Scott D Barthelmy, Louis M Barbier, Jay R Cummings, Ed E Fenimore, Neil Gehrels, Derek Hullinger, Hans A Krimm, Craig B Markwardt, David M Palmer, Ann Parsons, et al. The burst alert telescope (bat) on the swift midex mission. *Space Science Reviews*, 120(3-4):143–164, 2005.
- [40] Peter WA Roming, Thomas E Kennedy, Keith O Mason, John A Nousek, Lindy Ahr, Richard E Bingham, Patrick S Broos, Mary J Carter, Barry K Hancock, Howard E Huckle, et al. The swift ultra-violet/optical telescope. *Space Science Reviews*, 120(3-4):95–142, 2005.

- [41] Sergio Prostač. Swift spacecraft detected unique gamma-ray burst, 2012. URL <http://www.sci-news.com/astronomy/article00145.html>.
- [42] David N Burrows, JE Hill, JA Nousek, JA Kennea, A Wells, JP Osborne, AF Abbey, A Beardmore, K Mukerjee, ADT Short, et al. The swift x-ray telescope. *Space Science Reviews*, 120(3-4):165–195, 2005.
- [43] Browse Software Development Team. Swiftmastr - swift master catalog, 2014. URL <http://heasarc.gsfc.nasa.gov/W3Browse/swift/swiftmastr.html>.
- [44] F Krauss. Swift data analysis. 2012 - 2013.
- [45] National Aeronautics and Space Administration. Suzaku, 2016. URL <http://nssdc.gsfc.nasa.gov/nmc/spacecraftDisplay.do?id=2005-025A>.
- [46] NASA Goddard Space Flight Center. Suzaku mission overview, 2006. URL <http://heasarc.gsfc.nasa.gov/docs/suzaku/about/overview.html>.
- [47] Japan Aerospace Exploration Agency. Suzaku, 2008. URL <http://www.isas.jaxa.jp/e/enterp/missions/suzaku/>.
- [48] WB Atwood, Aous A Abdo, M Ackermann, W Althouse, B Anderson, M Axelsson, L Baldini, J Ballet, DL Band, Guido Barbiellini, et al. The large area telescope on the fermi gamma-ray space telescope mission. *The Astrophysical Journal*, 697(2):1071, 2009.
- [49] University of Nova Gorica Laboratory for Astroparticle Physics. Fermi large area telescope. URL <http://www.ung.si/en/research/laboratory-for-astroparticle-physics/projects/fermi-lat/>.
- [50] PL Nolan, AA Abdo, Markus Ackermann, Marco Ajello, A Allafort, E Antolini, WB Atwood, Magnus Axelsson, Luca Baldini, J Ballet, et al. Fermi large area telescope second source catalog. *The Astrophysical Journal Supplement Series*, 199(2):31, 2012.
- [51] Anthony M Brown and Jenni Adams. Discovery of γ -ray emission from the broad-line radio galaxy pictor a. *Monthly Notices of the Royal Astronomical Society*, 421(3):2303–2309, 2012.
- [52] The Fermi-LAT Collaboration. Fermi large area telescope third source catalog. *arXiv preprint arXiv:1501.02003*, 2015.

- [53] Luca Baldini. The fermi large area telescope an overview. *Fermi Summer School 2012, Lewes Delaware*.
- [54] Attila Abramowski, F Acero, F Aharonian, AG Akhperjanian, G Anton, A Balzer, A Barnacka, U Barres De Almeida, Y Becherini, J Becker, et al. The 2010 very high energy γ -ray flare and 10 years of multi-wavelength observations of m 87. *The Astrophysical Journal*, 746(2): 151, 2012.
- [55] Jelena Aleksić, S Ansoldi, LA Antonelli, P Antoranz, A Babic, P Bangale, M Barcelo, JA Barrio, J Becerra González, W Bednarek, et al. The major upgrade of the magic telescopes, part i: The hardware improvements and the commissioning of the system. *Astroparticle Physics*, 72:61–75, 2016.
- [56] Canadian Nuclear Association. Research reactors, 2015. URL <https://cna.ca/technology/research-development/research-reactors/>.
- [57] VA Acciari, M Beilicke, G Blaylock, SM Bradbury, JH Buckley, V Bugaev, Y Butt, O Celik, A Cesarini, L Ciupik, et al. Observation of gamma-ray emission from the galaxy m87 above 250 gev with veritascorresponding author:. *The Astrophysical Journal*, 679(1):397, 2008.
- [58] The VERITAS Collaboration. About veritas, 2015. URL <http://veritas.sao.arizona.edu/about-veritas-mainmenu-81>.
- [59] The VERITAS Collaboration. Welcome to veritas, 2016. URL <http://veritas.sao.arizona.edu/index.php>.
- [60] RD Parsons, A Balzer, M Füssling, C Hoischen, M Holler, AMW Mitchell, G Pühlhofer, G Rowell, S Wagner, E Bissaldi, et al. The hess ii grb program. *arXiv preprint arXiv:1509.05191*, 2015.
- [61] James Anthony Hinton, HESS collaboration, et al. The status of the hess project. *New Astronomy Reviews*, 48(5):331–337, 2004.
- [62] W. Hofmann. The h.e.s.s. telescopes, 2012. URL <https://www.mpi-hd.mpg.de/hfm/HESS/pages/about/telescopes/#mirror>.
- [63] The H.E.S.S. Collaboration. Largest ever cherenkov telescope sees first light. URL https://www.mpi-hd.mpg.de/hfm/HESS/pages/press/2012/HESS_II_first_light/.

- [64] California Institute of Technology Jet Propulsion Laboratory. Nasa/ipac extragalactic database (ned), 2012. URL <https://ned.ipac.caltech.edu/>.
- [65] Fermi Science Support Center. Lat 2-year point source catalog, 2012. URL https://fermi.gsfc.nasa.gov/ssc/data/access/lat/2yr_catalog/.
- [66] Fermi Science Support Center. Overview: Lat data analysis tools, 2012. URL <https://fermi.gsfc.nasa.gov/ssc/data/analysis/scitools/overview.html>.
- [67] Fermi Science Support Center. Lat background models, 2012. URL <https://fermi.gsfc.nasa.gov/ssc/data/access/lat/BackgroundModels.html>.
- [68] E Massaro, Matteo Perri, P Giommi, and R Nesci. Log-parabolic spectra and particle acceleration in the bl lac object mkn 421: Spectral analysis of the complete beposax wide band x-ray data set. *Astronomy & Astrophysics*, 413(2):489–503, 2004.
- [69] Trevor C Weekes. *Very high energy gamma-ray astronomy*. CRC Press, 2003.
- [70] Sheetal Saxena, Alexander Summa, Dominik Elsässer, Michael Rürger, and Karl Mannheim. Constraints on dark matter annihilation from m87. *The European Physical Journal C-Particles and Fields*, 71(11): 1–5, 2011.
- [71] Aous A Abdo, M Ackermann, M Ajello, WB Atwood, L Baldini, J Ballet, G Barbiellini, D Bastieri, BM Baughman, K Bechtol, et al. Fermi large area telescope view of the core of the radio galaxy centaurus a. *The Astrophysical Journal*, 719(2):1433, 2010.
- [72] Steven D Bloom and Alan P Marscher. An analysis of the synchrotron self-compton model for the multi-wave band spectra of blazars. *The Astrophysical Journal*, 461:657, 1996.
- [73] Aous A Abdo, M Ackermann, M Ajello, WB Atwood, M Axelsson, L Baldini, J Ballet, DL Band, G Barbiellini, D Bastieri, et al. Fermi/large area telescope bright gamma-ray source list. *The Astrophysical Journal Supplement Series*, 183(1):46, 2009.

- [74] Aous A Abdo, M Ackermann, M Ajello, et al. Fermi large area telescope gamma-ray detection of the radio galaxy m87. *The Astrophysical Journal*, 707(1):55, 2009.
- [75] Matthias Weidinger, Michael R uger, and Felix Spanier. Modelling the steady state spectral energy distribution of the bl-lac object pks 2155-304 using a selfconsistent ssc model. *arXiv preprint arXiv:1001.2145*, 2010.
- [76] Matthias Weidinger and Felix Spanier. Modelling the variability of 1es1218+ 30.4. *arXiv preprint arXiv:1005.3747*, 2010.
- [77] Matthias Weidinger and Felix Spanier. Variability along the blazar-sequence-hints for extragalactic cosmic rays? *arXiv preprint arXiv:1109.1975*, 2011.
- [78] M. Weidinger and F. Spanier. A self-consistent and time-dependent hybrid blazar emission model. properties and application. *arXiv preprint arXiv:1410.5380*, 2015.
- [79] Marco Chiaberge, Annalisa Celotti, Alessandro Capetti, and Gabriele Ghisellini. Does the unification of bl lac and fr i radio galaxies require jet velocity structures? *Astronomy and Astrophysics*, 358:104, 2000.
- [80] Markos Georganopoulos and Demosthenes Kazanas. Decelerating flows in tev blazars: a resolution to the bl lacertae-fr i unification problem. *The Astrophysical Journal Letters*, 594(1):L27, 2003.
- [81] JF Navarro, CS Frenk, and SDM White. Apj, 462, 563 crossref. *Web of Science*, 1996.
- [82] S. Saxena, D. Els asser, M. R uger, A. Summa, and K. Mannheim. Searching for Dark Matter Annihilation in M87. *Proceedings of the 32nd International Cosmic Ray Conference*, September 2011.
- [83] Paolo Gondolo, Joakim Edsj o, Piero Ullio, Lars Bergstr om, Mia Schelke, and Edward A Baltz. Darksusy: Computing supersymmetric dark matter properties numerically. *Journal of Cosmology and Astroparticle Physics*, 2004(07):008, 2004.
- [84] Hubblesite Newscenter. Hubble acs image of elliptical galaxy m87, 2008. URL <http://hubblesite.org/newscenter/archive/releases/2008/30/image/f/>.

- [85] M Ruger, F Spanier, and K Mannheim. Spectral modelling of 1 es 1218+ 30.4. *Monthly Notices of the Royal Astronomical Society*, 401 (2):973–976, 2010.
- [86] Fermi LAT Collaboration et al. Limits on dark matter annihilation signals from the fermi lat 4-year measurement of the isotropic gamma-ray background. *Journal of Cosmology and Astroparticle Physics*, 2015 (09):008, 2015.
- [87] Aous A Abdo, M Ackermann, M Ajello, K Asano, L Baldini, J Ballet, Guido Barbiellini, Denis Bastieri, BM Baughman, K Bechtol, et al. Fermi discovery of gamma-ray emission from ngc 1275. *The Astrophysical Journal*, 699(1):31, 2009.
- [88] HIDETOSHI Kubo, T Takahashi, G Madejski, M Tashiro, F Makino, S Inoue, and F Takahara. Asca observations of blazars and multiband analysis. *The Astrophysical Journal*, 504(2):693, 1998.
- [89] Scott Wakely and Deirdre Horan. Tevcat - tev catalog, 2017. URL <http://tevcats.uchicago.edu/>.
- [90] Justin D Finke, Charles D Dermer, and Markus Bottcher. Synchrotron self-compton analysis of tev x-ray-selected bl lacertae objects. *The Astrophysical Journal*, 686(1):181, 2008.
- [91] National Aeronautics and Space Administration. Fermi’s lat extended view, 2012. URL https://www.nasa.gov/mission_pages/GLAST/news/NGC1275-IC310.html.
- [92] Jelena Aleksić, LA Antonelli, P Antoranz, M Backes, JA Barrio, D Bastieri, J Becerra Gonzalez, W Bednarek, A Berdyugin, K Berger, et al. Detection of very high energy gamma-ray emission from the perseus cluster head-tail galaxy ic 310 by the magic telescopes. *The Astrophysical Journal Letters*, 723(2):L207, 2010.
- [93] A Neronov, D Semikoz, and Ie Vovk. Very high-energy γ -ray emission from ic 310. *Astronomy & Astrophysics*, 519:L6, 2010.
- [94] IJ Danziger, RAE Fosbury, and MV Penston. Optical observations of pictor a. *Monthly Notices of the Royal Astronomical Society*, 179(1):41P–45P, 1977.
- [95] SJ Tingay, DL Jauncey, JE Reynolds, AK Tzioumis, PM McCulloch, SP Ellingsen, ME Costa, JEJ Lovell, RA Preston, and SM Simkin. The

- parsec-scale structure and evolution of the nearby fanaroff-riley type ii radio galaxy pictor a. *The Astronomical Journal*, 119(4):1695, 2000.
- [96] Aous A Abdo, M Ackermann, M Ajello, WB Atwood, L Baldini, J Ballet, G Barbiellini, D Bastieri, BM Baughman, K Bechtol, et al. Fermi large area telescope view of the core of the radio galaxy centaurus a. *The Astrophysical Journal*, 719(2):1433, 2010.
- [97] Jin Zhang, J-M Bai, Liang Chen, and Xian Yang. Origin of the x-rays and possible gev-tev emission from the western hot spot of pictor a. *The Astrophysical Journal*, 701(1):423, 2009.
- [98] Alessandro Marconi, Ethan J Schreier, Anton Koekemoer, Alessandro Capetti, David Axon, Duccio Macchetto, and Nicola Caon. Unveiling the active nucleus of centaurus a. *The Astrophysical Journal*, 528(1):276, 2000.
- [99] F Aharonian, AG Akhperjanian, G Anton, U Barres De Almeida, AR Bazer-Bachi, Y Becherini, B Behera, W Benbow, K Bernlöhr, C Boisson, et al. Discovery of very high energy γ -ray emission from centaurus a with hess. *The Astrophysical Journal Letters*, 695(1):L40, 2009.
- [100] Markos Georganopoulos and Demosthenes Kazanas. Decelerating flows in tev blazars: a resolution to the bl lacertae-fr i unification problem. *The Astrophysical Journal Letters*, 594(1):L27, 2003.
- [101] J-P Lenain, Catherine Boisson, H el ene Sol, and K Katarzy nski. A synchrotron self-compton scenario for the very high energy gamma-ray emission of the radiogalaxy m 87-unifying the tev emission of blazars and other agns? *Astronomy & Astrophysics*, 478(1):111–120, 2008.
- [102] F Aharonian, S Wagner, M Ostrowski, et al. Absorption of nuclear γ -rays on the starlight radiation in fr i sources: the case of centaurus a. *Monthly Notices of the Royal Astronomical Society*, 371(4):1705–1716, 2006.
- [103] MG Aartsen, M Ackermann, J Adams, JA Aguilar, M Ahlers, M Ahrens, D Altmann, T Anderson, C Argu elles, TC Arlen, et al. Observation of high-energy astrophysical neutrinos in three years of icecube data. *Physical review letters*, 113(10):101101, 2014.
- [104] Pedro Abreu, M Aglietta, M Ahlers, EJ Ahn, IFM Albuquerque, D Allard, I Allekotte, J Allen, P Allison, A Almela, et al. Ultrahigh energy neutrinos

- at the pierre auger observatory. *Advances in High Energy Physics*, 2013, 2013.
- [105] Goddard Space Flight Center. Fermi searches for dark matter, 2016. URL <https://fermi.gsfc.nasa.gov/science/eteu/dm/>.
- [106] F Acero, M Ackermann, M Ajello, A Albert, WB Atwood, Magnus Axelson, L Baldini, J Ballet, G Barbiellini, D Bastieri, et al. Fermi large area telescope third source catalog. *The Astrophysical Journal Supplement Series*, 218(2):23, 2015.
- [107] Roopesh Ojha, Matthias Kadler, Moritz Böck, Roy Booth, Michael S Dutka, Philip G Edwards, Alan L Fey, Lars Fuhrmann, Ralph A Gaume, Hayo Hase, et al. Tanami: tracking active galactic nuclei with austral milliarcsecond interferometry-i. first-epoch 8.4 ghz images. *Astronomy & Astrophysics*, 519:A45, 2010.
- [108] MC Shepherd, TJ Pearson, and GB Taylor. Difmap: an interactive program for synthesis imaging. *Bulletin of the American Astronomical Society*, 26:987–989, 1994.
- [109] Robert Schulz. Scientific discussion. *Lehrstuhl für Astronomie, Universität Würzburg*, 2013 - 2015.
- [110] Matthias Kadler. Data analysis. *Lehrstuhl für Astronomie, Universität Würzburg*, 2013 - 2014.
- [111] Cornelia Müller. Data analysis. *Lehrstuhl für Astronomie, Universität Würzburg*, 2011.
- [112] Jonas Trüstedt. Data analysis. *Lehrstuhl für Astronomie, Universität Würzburg*, 2013.
- [113] Talvikki Hovatta, Margo F Aller, Hugh D Aller, Eric Clausen-Brown, Daniel C Homan, Yuri Y Kovalev, Matthew L Lister, Alexander B Pushkarev, and Tuomas Savolainen. Mojave: Monitoring of jets in active galactic nuclei with vlba experiments. xi. spectral distributions. *The Astronomical Journal*, 147(6):143, 2014.
- [114] ML Lister, MF Aller, HD Aller, DC Homan, KI Kellermann, YY Kovalev, AB Pushkarev, JL Richards, E Ros, and T Savolainen. Mojave. x. parsec-scale jet orientation variations and superluminal motion in active galactic nuclei. *The Astronomical Journal*, 146(5):120, 2013.

- [115] BJ Geldzahler and EB Fomalont. Radio observations of the jet in Fornax A. *The Astronomical Journal*, 89:1650–1657, 1984.
- [116] CN Tadhunter, R Morganti, S di Serego Alighieri, RAE Fosbury, and IJ Danziger. Optical spectroscopy of a complete sample of southern 2-Jy radio sources. *Monthly Notices of the Royal Astronomical Society*, 263(4):999–1022, 1993.
- [117] FP Israel, D Raban, RS Booth, and FT Rantakyrö. The millimeter-wave continuum spectrum of Centaurus A and its nucleus. *Astronomy & Astrophysics*, 483(3):741–748, 2008.
- [118] RD Ekers, JV Wall, PA Shaver, WM Goss, RAE Fosbury, IJ Danziger, AFM Moorwood, DF Malin, AS Monk, and JA Ekers. A complete sample of radio galaxies—i. the radio data. *Monthly Notices of the Royal Astronomical Society*, 236(4):737–777, 1989.
- [119] HYRON Spinrad, J Marr, L Aguilar, and S Djorgovski. A third update of the status of the 3CR sources: Further new redshifts and new identifications of distant galaxies. *Publications of the Astronomical Society of the Pacific*, 97(596):932, 1985.
- [120] Matthias Kadler, Dorit Eisenacher, Eduardo Ros, Karl Mannheim, Dominik Elsässer, and Uwe Bach. The blazar-like radio structure of the TeV source IC 310. *Astronomy & Astrophysics*, 538:L1, 2012.
- [121] H Kühr, A Witzel, IIK Pauliny-Toth, and U Nauber. A catalogue of extragalactic radio sources having flux densities greater than 1 Jy at 5 GHz. *Astronomy and Astrophysics Supplement Series*, 45:367–430, 1981.
- [122] Chris J Willott, Steve Rawlings, Katherine M Blundell, Mark Lacy, and Stephen A Eales. The radio luminosity function from the low-frequency 3CR, 6CE and 7CRS complete samples. *Monthly Notices of the Royal Astronomical Society*, 322(3):536–552, 2001.
- [123] Zunli Yuan and Jiancheng Wang. On the evolution of the cores of radio sources and their extended radio emission. *The Astrophysical Journal*, 744(2):84, 2011.
- [124] PA Oesch, G Brammer, PG van Dokkum, GD Illingworth, RJ Bouwens, I Labbé, M Franx, I Momcheva, MLN Ashby, GG Fazio, et al. A remarkably luminous galaxy at $z = 11.1$ measured with Hubble Space Telescope grism spectroscopy. *The Astrophysical Journal*, 819(2):129, 2016.

-
- [125] Caleb A Scharf and Reshmi Mukherjee. A statistical detection of gamma-ray emission from galaxy clusters: implications for the gamma-ray background and structure formation. *The Astrophysical Journal*, 580(1):154, 2002.
- [126] David W Hogg. Distance measures in cosmology. *arXiv preprint astro-ph/9905116*, 1999.

Acknowledgements

Scholarly appreciation is extended to the following individuals. K. Mannheim, P. Jakob, R. Ströhmer, R. Mukherjee, W. Prod, M. Errando, D. Elsässer, M. Weidinger, A. Bolaños, A. Shukla, R. Schulz, N. Paschenda, and M. Richard.

This research has made use of the NASA/IPAC Extragalactic Database (NED) which is operated by the Jet Propulsion Laboratory, California Institute of Technology, under contract with the National Aeronautics and Space Administration.